박 사 학 위 논 문
Ph.D. Dissertation

다중 보 유한요소를 이용한 케이블의 모델링 방법 및 이를 이용한 케이블 설계

Modeling of helically stranded cables using multiple beam finite elements and its application to cable design

2017

김 성 윤 (金 成 閏 Kim, Sung-Yun)

한 국 과 학 기 술 원

Korea Advanced Institute of Science and Technology

박 사 학 위 논 문

다중 보 유한요소를 이용한 케이블의 모델링 방법 및 이를 이용한 케이블 설계

2017

김 성 윤

한 국 과 학 기 술 원

기계항공공학부/기계공학과

다중 보 유한요소를 이용한 케이블의 모델링 방법 및 이를 이용한 케이블 설계

김 성 윤

위 논문은 한국과학기술원 박사학위논문으로
학위논문 심사위원회의 심사를 통과하였음

2017 년 5 월 10 일

심사위원장 이 필 승 (인)

심 사 위 원 김 병 완 (인)

심 사 위 원 김 진 환 (인)

심 사 위 원 이 준 근 (인)

심 사 위 원 정 현 (인)

Modeling of helically stranded cables using multiple beam finite elements and its application to cable design

Sung-Yun Kim

Advisor: Phill-Seung Lee

A dissertation/thesis submitted to the faculty of
Korea Advanced Institute of Science and Technology in
partial fulfillment of the requirements for the degree of
Doctor of Philosophy in Mechanical Engineering

Daejeon, Korea
May 10, 2017

Approved by

Phill-Seung Lee,
Professor of Mechanical Engineering

The study was conducted in accordance with Code of Research Ethics[1].

1) Declaration of Ethical Conduct in Research: I, as a graduate student of Korea Advanced Institute of Science and Technology, hereby declare that I have not committed any act that may damage the credibility of my research. This includes, but is not limited to, falsification, thesis written by someone else, distortion of research findings, and plagiarism. I confirm that my dissertation contains honest conclusions based on my own careful research under the guidance of my advisor.

DME 20115044

김성윤. 다중 보 유한요소를 이용한 케이블의 모델링 방법 및 이를 이용한 케이블 설계. 기계항공공학부/기계공학. 2017 년. 106+vi 쪽. 지도교수: 이필승. (영문 논문)

Sung-Yun Kim. Modeling of helically stranded cables using multiple beam finite elements and its application to cable design. Department of Mechanical Engineering. 2017. 106+vi pages. Advisor: Phill-Seung Lee. (Text in English)

초 록

스트랜드 케이블(Helically stranded cable)의 기계적 거동을 정확히 해석하기 위한 다중 보 유한요소 모델을 제안하고, 이를 이용한 케이블의 최적 회전 균형 설계 방법(procedure of torque balance design)을 제시하였다. 보 유한요소해석 모델은 각 와이어간의 접촉 거동 및 탄소성 재료 거동을 잘 구현할 수 있도록 구성하였으며, 본 논문에서 제안한 보 유한요소 모델에 대해 케이블의 축 하중 및 굽힘 하중시의 기계적 거동을 해석하고 이론 및 실험, 타 유한요소 모델들과 그 정확성과 효율성을 비교하였다. 보 유한요소 모델은 케이블 전체 거동을 정확히 해석하면서도 효율성이 뛰어났다. 보 유한요소 모델을 이용하여 케이블 해석을 위한 이론 모델에 대한 강성 계수의 분석 및 적용성을 평가하였으며, 서브루틴(Subroutine) 프로그램을 이용하여 유한요소해석 모델의 마찰 거동을 구현한 후 이에 대해 평가하고 가장 효율적 모델을 제안하였다. 다중 보 요소를 이용한 스트랜드 케이블의 회전 균형 설계 방법을 제안하고, 실험을 통해 제안된 설계 방법을 검증하였으며, 무차원 계수의 도입을 통해 초기 케이블 설계 단계에서 쉽게 적용 가능한 회전 균형 곡선을 제시하였다.

핵 심 낱 말 : 스트랜드 케이블, 유한요소해석, 보요소, 보모델링, 쿨롱 마찰, 회전균형

Abstract

In this paper, a method for the effective modeling of helically stranded cables for which multiple beam finite elements (FE) are used is presented, and a design procedure for the torque balance of the cables using the beam FE model is proposed. Regarding the beam modeling, the wire-to-wire contacts and the elastoplastic material behavior are considered. The proposed beam model is advantageous because the accuracy of the corresponding numerical results is as good as that of the full solid model, while the computational cost is significantly reduced. Using the beam FE model, the mechanical behavior of helically stranded cables is analyzed under axial and transverse loadings. The numerical results are compared with those of full solid FE models and available experimental results, where accuracy and computational cost are investigated. This paper also proposes a practical procedure for torque balance design of helically stranded cables using the proposed beam FE model. Furthermore, the proposed design procedure is verified by experimental tests and the generalized torque balance curves are proposed using dimensionless parameter.

Keywords helically stranded cable, finite element analysis, beam finite elements, beam modeling, Coulomb friction, friction coefficient, torque balance

Contents

List of Tables

List of Figures

Chapter 1. Introduction

Cables and ropes that consist of helically stranded wires have been used in a wide range of engineering applications, and the understanding of their mechanical behavior is a very important issue for cable designers and manufacturers; however, it is not easy to formulate accurate predictions regarding the behavior of these wires because of the corresponding complex geometry and the internal contacts that exist between the individual wires. While experimental tests are necessary for the attainment of accurate predictions (see the previous works by Utting and Jones [1–3]), laboratory experiments are typically very expensive and difficult to conduct. The analytical or numerical modeling of cables, if sufficiently accurate, can replace such costly tests, which are carried out routinely by cable manufactures, and can lead to a considerable cost reduction.

Several analytical models [4–10] that enable the prediction of the mechanical behavior of cables and ropes under various loading conditions are available. Although these analytical models are simple and easy to use, the validity of these models is limited for simple stranded cables under axial loading because of the difficulty regarding the consideration of the complicated geometry, the material, and the complex contact behavior among the individual wires; in particular, wire-to-wire contact behavior is very complicated.

The finite element analysis has been successfully used to predict the behavior of cables; in particular, full solid finite element (FE) models have been developed for which the wire-to-wire contact, the wire yielding, and various loading conditions are considered (see references [11–17]). The predictive ability of the full solid FE models regarding the complicated behavior of wires are far more accurate than those of the analytical models; however, in terms of helically stranded cables, this kind of modeling is not trivial. All of the individual wires must be precisely placed in the FE model and must be in contact with each other without penetration to avoid the emergence of numerical instabilities during a nonlinear solution procedure; furthermore, to accurately capture the geometry of the wires and to model the complicated wire-to-wire contact conditions, very fine meshes that can incur a considerable computational cost are required.

In the cable design phase, full solid FE models are quite often the cause of a time delay that may result in losses of opportunity and profit for a new cable product. To overcome this problem, analysts have come up with strategies such as the use of coarse mesh, or even an adjustment of the element size; however, these strategies can be very labor intensive and do not always work, and this could be why the full solid FE model for analysis of helically stranded cables is a very good solution but has a limitation in applying it to cable design. Overcoming this limitation is a major interest of cable designers and manufacturers. The cable designers require a tool that is reasonably accurate and simple to use; this is especially important during the preliminary design stage of a new cable system. This outstanding need is the motivation of this work.

In this study, we propose a beam FE model for a computationally efficient prediction of the mechanical behavior of helically stranded cables whereby complicated contacts and the elastoplastic behavior of wires are included; here, the wires are modeled using beam finite elements, and the wire-to-wire contacts are modeled using beam-to-beam contacts. Compared to the solid FE models, the degrees of freedom (DOFs) are significantly reduced, but the resulting predictive capability is as good as those of the solid FE models; furthermore, a large modeling effort is saved because the beam FE model is very effective in terms of both accuracy and computational cost.

The torque balance design of cables is very important for the prevention or minimization of an undesirable twist, which is due to the coupling between the stretching and the twisting when cables are axially loaded with tension. The torque balance design generally requires a large number of torque analyses, and these must be performed accurately during the preliminary design stage. The solid FE models are proper in terms of accuracy, but the computational costs are too high; indeed, the solid models have not been used for the torque balance design of cables in engineering practice, where the use of the beam FE models can be a practical solution. In this paper, a design procedure for the achievement of the torque balance of helically stranded cables is suggested, whereby the proposed beam FE model is used. Furthermore, the proposed design procedure is verified by experimental tests and the generalized torque balance curves are proposed using dimensionless parameter.

This paper is organized as follows: The mathematical relations of a helically stranded cable is introduced and the stiffness coefficients for the various analytical models are evaluated in Section 2; the FE models for the prediction of the mechanical behavior of the cables are presented in Section 3; in Section 4, the influence of friction is analyzed and the computational cost are investigated. And, the accuracies of the FE models are verified through a comparison of the numerical results to the analytical and experimental results; a procedure for the torque balance design of the cables is proposed in Section 5; the proposed design procedure is verified by experimental tests and the generalized torque balance curves are proposed using dimensionless parameter in Section 6; and the conclusions are given in Section 7.

Chapter 2. Mathematical relations of a helically stranded cable

The mathematical model of the helically stranded cable depends on the assembly of the wires configuring it and the nature of their contact conditions. The curved rod models fairly represent the bent and curved nature of the wires and allow the representation of the individual behavior of each wire in the same layer and adjoining layers.

In this section, the equations for curved rod models regarding an understanding of basic cable mechanics under axial loading and bending are provided. And, these are also used for the comparison with numerical results.

2. 1 Kinematic relations

In helically stranded cables, the kinematics of axial stretching and twisting are coupled together, and twisting can therefore occur under a pure axial loading; in such a case, it can be assumed that all of the wires in a given layer carry exactly the same loads. Global cable kinematics are designated by the cable axial strain ε and the cable twist rate $\delta\theta / h$ (twist per unit length). The linear elastic response is governed by the following equation:

$$\begin{bmatrix} F_T \\ M_T \end{bmatrix} = \begin{bmatrix} K_{\varepsilon\varepsilon} \, K_{\varepsilon\theta} \\ K_{\theta\varepsilon} \, K_{\theta\theta} \end{bmatrix} \begin{bmatrix} \varepsilon \\ \delta\theta / h \end{bmatrix}, \tag{1}$$

where F_T and M_T are cable axial force and cable torsion, respectively, and in the stiffness matrix components, the subscripts ε and θ denote axial stretch and twisting, respectively.

Figs. 2.1 (a), (b) and (c) show the geometry of a single-layer helically-stranded cable and the developed geometry of a helical wire.

The axial strain and shear strain of the cable are given by the following equation:

$$\varepsilon = \frac{\delta h}{h}, \quad \gamma = r(\frac{\delta\theta}{h})\tan\alpha, \tag{2}$$

where h is cable length, r_c is core radius, r_w is wire radius, r is wire centerline radius $(r_c + r_w)$, γ is shear strain, θ is twist angle (rad), and α is helix angle. It is assumed that the axial strain is constant in both the core and the wires, and that the shear strain is constant in the wires. The shear strain is not induced in the core due to the axial loading.

In Fig. 2.1 (c), the following relations can be established:

$$h = l \sin \alpha \, , \quad r\theta = l \cos \alpha \, , \tag{3}$$

where l is the length of the helical wire in the developed geometry.

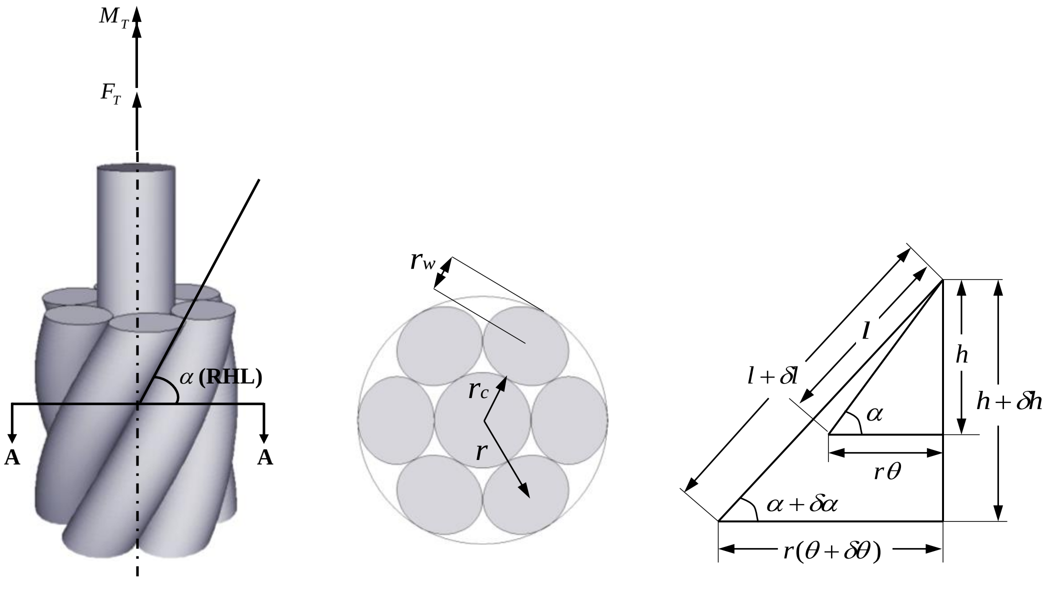

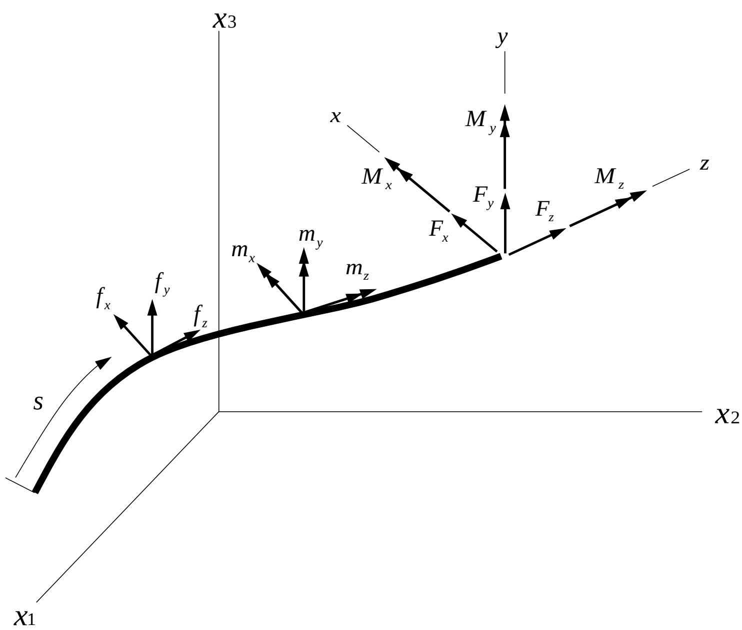

Fig. 2.1. Geometry of a helically-stranded cable (1 layer, 1 + 6 structure). (a) Cable geometry, (b) Cross section A-A, (c) Developed geometry of the helical wire, (d) Forces and moments on a helical wire

It is assumed that the core is rigid radially, the material is linear elastic and isotropic, and the slips between the wires are ignored.

$$\delta r = 0,\ \ \delta l \neq 0,\ \ \delta\alpha \neq 0,\ \ \delta\theta \neq 0. \tag{4}$$

When the deformation is small,

$$\delta h = l\cos\alpha\delta\alpha + \sin\alpha\delta l, \tag{5}$$

$$r\delta\theta = -l\sin\alpha\delta\alpha + \cos\alpha\delta l. \tag{6}$$

Solving equations (5) and (6) for $\delta\alpha$ and using Eqs. (2) and (3)

$$\delta\alpha = (\varepsilon - \gamma)\sin\alpha\cos\alpha, \tag{7}$$

eliminating $\delta\alpha$ in Eqs. (4) and (5), the axial strain of the helical wire ε_w is then obtained by the following equation:

$$\varepsilon_w = \frac{\delta l}{l} = \varepsilon\sin^2\alpha + \gamma\cos^2\alpha \cdot \tag{8}$$

The initial curvatures are known for a helix as

$$\kappa_{x0} = 0,\ \ \kappa_{y0} = \frac{\cos^2\alpha}{r}, \tag{9}$$

where κ_x and κ_y are the curvatures in the x and y directions, respectively.

The initial twist for a helix is known as

$$\tau_0 = \frac{(\sin\alpha\cos\alpha)}{r}, \tag{10}$$

where τ is the twist per unit length.

The change in κ_x is zero, since the deformed helical wires again remain helical on the cylindrical core. The changes in κ_y and τ are found by variation in Eqs. (9) and (10) , respectively as,

$$\Delta\kappa_y = \delta\left(\frac{\cos^2\alpha}{r}\right), \quad \Delta\tau = \delta\left(\frac{\sin\alpha\cos\alpha}{r}\right), \tag{11}$$

using Eq. (11) with the kinematic conditions, Eq. (3)

$$\Delta\kappa_y = -\sin 2\alpha\left(\frac{\delta\alpha}{r}\right), \quad \Delta\tau = \cos 2\alpha\left(\frac{\delta\alpha}{r}\right). \tag{12}$$

Using $\delta\alpha$ from Eq. (7) and noting that $\kappa_{x0} = 0$, the changes of the curvature $\Delta\kappa_y$ and the twist $\Delta\tau$ can be calculated by the following equations, respectively:

$$\Delta\kappa_y = -\sin 2\alpha \sin\alpha\cos\alpha(\varepsilon-\gamma), \quad \Delta\tau = \cos 2\alpha \sin\alpha\cos\alpha(\varepsilon-\gamma), \tag{13}$$

the final curvature κ_y and twist τ are given by

$$\kappa_y = \kappa_{y0} + \Delta\kappa = \frac{\cos^2\alpha}{r} - \sin 2\alpha \sin\alpha\cos\alpha(\varepsilon-\gamma), \tag{14}$$

$$\tau = \tau_0 + \Delta\tau = \frac{(\sin\alpha\cos\alpha)}{r} + \cos 2\alpha \sin\alpha\cos\alpha(\varepsilon-\gamma). \tag{15}$$

2. 2 Equilibrium equations of wire

The equilibrium equations for the resultant forces and moments can be derived for a general twisted and bent rod under the action of distributed external loads and moments as shown in Fig. 2.1 (d).

$$\frac{dF_x}{ds} - F_y\tau + F_z\kappa_y + f_x = 0, \tag{16}$$

$$\frac{dF_y}{ds} - F_z\kappa_x + F_x\tau + f_y = 0, \tag{17}$$

$$\frac{dF_z}{ds} - F_x\kappa_y + F_y\kappa_x + f_z = 0, \tag{18}$$

$$\frac{dM_x}{ds} - M_y\tau + M_z\kappa_y + m_x = 0, \tag{19}$$

$$\frac{dM_y}{ds} - M_z\kappa_x + M_x\tau + m_y = 0,\tag{20}$$

$$\frac{dM_z}{ds} - M_x\kappa_y + M_y\kappa_x + m_z = 0,\tag{21}$$

where s is the arc length along the wire, and F_x, F_y, and F_z are the resultant forces on a wire cross section in the x, y, and z directions, respectively. M_x and M_y are the bending moments about the x axis and y axis, respectively, and M_z is the twisting moment in the wire. f_x, f_y and f_z are the components of the external line load per unit length of the centerline of the wire in the x, y, and z directions, respectively. m_x, m_y and m_z are the components of the external moment per unit length of the centerline in the x, y, and z directions, respectively.

The bending and twisting couples M_y and M_z and the wire tension F_z can be simply expressed as the following formulas:

$$M_y = EI\Delta\kappa_y, M_z = GJ\Delta\tau, \quad F_z = EA\varepsilon_w, \quad F_y = M_z\kappa_y - M_y\tau,\tag{22}$$

where E is the Young's modulus of the wire, I is the moment of inertia of the helical wire cross section, J is the polar moment of inertia of the helical wire cross section, and A is the cross sectional area of the helical wire. The stresses caused by axial loads are presented in Appendix A.

2. 3 Equilibrium equations of stranded cable

The resultant external force of the cable F_T and the moment M_T can be obtained from the following equations, where the core deformation is additionally considered:

$$F_T = n(F_z \sin\alpha + F_y \cos\alpha) + E_c A_c,\tag{23}$$

$$M_T = n(M_z \sin\alpha + M_y \cos\alpha + F_z r\cos\alpha - F_y r\sin\alpha) + G_c J_c,\tag{24}$$

where n is the total number of wires, and E_c, A_c, G_c, and J_c are the Young's modulus, area, shear modulus, and polar moment of inertia of the core cross section, respectively.

2. 4 Stiffness matrix components of various analytical models

The equations for each analytical model are then briefly presented in a standardized form

2.4.1 Hruska's model

The model of Hruska is based on simple hypothesis that wires are subjected to pure tensile force only (no moments) during any axial loading. Since the curved nature of the helical wire is neglected, the flexural and twisting moments terms EI , GJ are omitted in the equations of stiffness constants and only the axial stretch terms (EA) are present. The stiffness coefficients are presented as:

$$K_{\varepsilon\varepsilon} = n(EA\sin^3\alpha) + E_c A_c \tag{25a}$$

$$K_{\varepsilon\theta} = K_{\theta\varepsilon} = n(EAr\sin^2\alpha\cos\alpha) , \tag{25b}$$

$$K_{\theta\theta} = n(EAr^2\sin\alpha\cos^2\alpha) + G_c J_c . \tag{25c}$$

2.4.2 Machida and Durelli model

The model, through considered the effects of tension, bending and twist in the wires, neglected the term F_y in the equilibrium equations. Accordingly the equations for $K_{\varepsilon\varepsilon}$, $K_{\varepsilon\theta}$ remained unaltered and the equations are derived as:

$$K_{\varepsilon\varepsilon} = n(EA\sin^3\alpha) + E_c A_c \tag{26a}$$

$$K_{\varepsilon\theta} = n(EAr\sin^2\alpha\cos\alpha) , \tag{26b}$$

$$K_{\theta\varepsilon} = n\left[EAr\sin^2\alpha\cos\alpha + \frac{GJ\cos 2\alpha\sin^2\alpha\cos\alpha}{r} - \frac{EI\sin 2\alpha\sin\alpha\cos^2\alpha}{r}\right], \tag{26c}$$

$$K_{\theta\theta} = n\left[EAr^2\sin\alpha\cos^2\alpha - GJ\cos 2\alpha\sin^3\alpha + EI\sin 2\alpha\sin^2\alpha\cos\alpha\right] + G_c J_c . \tag{26d}$$

2.4.3 Costello's model

Considering the effects of tension, bending, and twist, Costello model can be derived the following stiffness components:

$$K_{\varepsilon\varepsilon} = n\left[EA\sin^3\alpha + \frac{GJ\cos 2\alpha\cos^4\alpha\sin\alpha}{r^2} + \frac{EI\sin 2\alpha\cos^3\alpha\sin^2\alpha}{r^2}\right] + E_c A_c \tag{27a}$$

$$K_{\varepsilon\theta} = n\left[EAr\sin^2\alpha\cos\alpha - \frac{GJ\cos 2\alpha\cos^3\alpha\sin^2\alpha}{r} - \frac{EI\sin 2\alpha\cos^2\alpha\sin^3\alpha}{r}\right] \tag{27b}$$

$$K_{\theta\varepsilon} = n\left[EAr\sin^2\alpha\cos\alpha + \frac{GJ\cos 2\alpha\sin^4\alpha\cos\alpha}{r} - \frac{EI\sin 2\alpha\cos^2\alpha\sin\alpha(1+\sin^2\alpha)}{r}\right] \tag{27c}$$

$$K_{\theta\theta} = n\left[EAr^2\sin\alpha\cos^2\alpha - GJ\cos 2\alpha\sin^5\alpha + EI\sin 2\alpha\cos\alpha\sin^2\alpha(1+\sin^2\alpha)\right] + G_c J_c \tag{27d}$$

It is important to note that the derived analytical equations in Eqs. (25), (26) and (27) can be used for only the linear elastic range.

The selected analytical models with their principal features, behaviors of wire and change in geometry due to Poisson's effect, are summarized in Table 2.1.

Table 2.1 The analytical models with their principal features

Model	Behavior of wires			Poisson's effect
	Tension	Torsion	Bending	
Hruska	O	X	X	X
Machida	O	O	O	X
Costello	O	O	O	O

2.4.4 Evaluation of the stiffness coefficients for the various analytical models

The model was considered as a 7- wire helically stranded cable with a core and helical wire diameters of 3.94mm and 3.72mm respectively. The geometric and material properties are given in Table 2.2. The stiffness coefficients of the various models have been evaluated and given in Table 2.3 for the range of helix angles, $45° < \alpha < 85°$.

Table 2.2. Geometric and material properties of the 7-wire helically-stranded cable where RHL denotes "right hand lay" (see Fig. 1.1 (a)).

Layer No.	No. of Wires	Helical direction & angle	Wire diameter [mm]	Pitch length [mm]	Young's Modulus [GPa]	Plastic Modulus [GPa]	Yield Strength [GPa]	Poisson's ratio
Core	1	-	3.94	-	188	24.60	1.54	0.3
1	6	RHL, 72.97°	3.72	78.67	188	24.60	1.54	0.3

The wire dimensions in Table 2.2 were chosen for this analysis for the subsequent study and investigations. The difference in $K_{\varepsilon\varepsilon}$, $K_{\varepsilon\theta}$, $K_{\theta\varepsilon}$ and $K_{\theta\theta}$ in the range of α is relatively so small that almost all models yields mutually agreeable results as given in Table 2.3. This is mainly because of the predominance of the effect of wire stretch compared to that of wire twist and bending as can be seen Table 2.4 and Fig. 2.2. Table 2.4 and Fig. 2.2 present the relative significance of the contributions among them when the wire axial force, wire twisting moment and wire bending moment are given.

Table 2.3. Stiffness coefficients as a function of helix angle for three models

Model	Helix angle [deg]	$K_{\varepsilon\varepsilon}$ [MN]	$K_{\varepsilon\theta}$ [MN-mm]	$K_{\theta\varepsilon}$ [MN-mm]	$K_{\theta\theta}$ [MN-mm^2]
Hruska	45	6.63	16.60	16.60	65.29
	50	7.80	17.71	17.71	58.63
	60	10.26	17.61	17.61	40.65
	70	12.46	14.18	14.18	21.48
	80	14.00	7.91	7.91	7.05
	85	14.41	4.06	4.06	3.07
Machida	45	6.63	16.60	15.62	67.40
	50	7.80	17.71	16.71	61.57
	60	10.26	17.61	16.69	45.10
	70	12.46	14.18	13.49	27.08
	80	14.00	7.91	7.54	13.34
	85	14.41	4.06	3.88	9.53
Costello	45	6.75	16.11	15.13	66.76
	50	7.90	17.28	16.26	60.36
	60	10.30	17.33	16.40	42.74
	70	12.48	14.07	13.38	23.69
	80	14.00	7.89	7.53	9.22
	85	14.41	4.06	3.87	5.21

Table 2.4. Relative significance of individual contributions by wire stretch, wire bending and wire twist of six wires to the cable stiffness for Costello's models.

Stiffness coefficient	Wire behavior	Helix angle [deg]					
		45	50	60	70	80	85
$K_{\varepsilon\varepsilon}$ [MN]	Stretch	4.3345	5.5112	7.9630	10.1728	11.7095	12.1204
	Twist	0.0000	-0.0126	-0.0105	-0.0055	-0.0005	0.0000
	Bending	0.1278	0.1109	0.0587	0.0164	0.0013	0.0001
$K_{\varepsilon\theta}$ [MN-mm]	Stretch	16.6012	17.7117	17.6082	14.1810	7.9078	4.0613
	Twist	0.0000	0.0752	0.1153	0.0613	0.0103	0.0014
	Bending	-0.4894	-0.5064	-0.3893	-0.1727	-0.0273	-0.0036
$K_{\theta\varepsilon}$ [MN-mm]	Stretch	16.6012	17.7117	17.6082	14.1810	7.9078	4.0613
	Twist	0.0000	-0.0819	-0.2995	-0.4351	-0.3269	-0.1800
	Bending	-1.4682	-1.3694	-0.9084	-0.3684	-0.0554	-0.0073
$K_{\theta\theta}$ [MN-mm^2]	Stretch	63.5824	56.9208	38.9362	19.7684	5.3404	1.3608
	Twist	0.0000	0.3736	1.9867	4.5781	7.0999	7.8810
	Bending	5.6234	6.2504	6.0262	3.8761	1.2031	0.3173

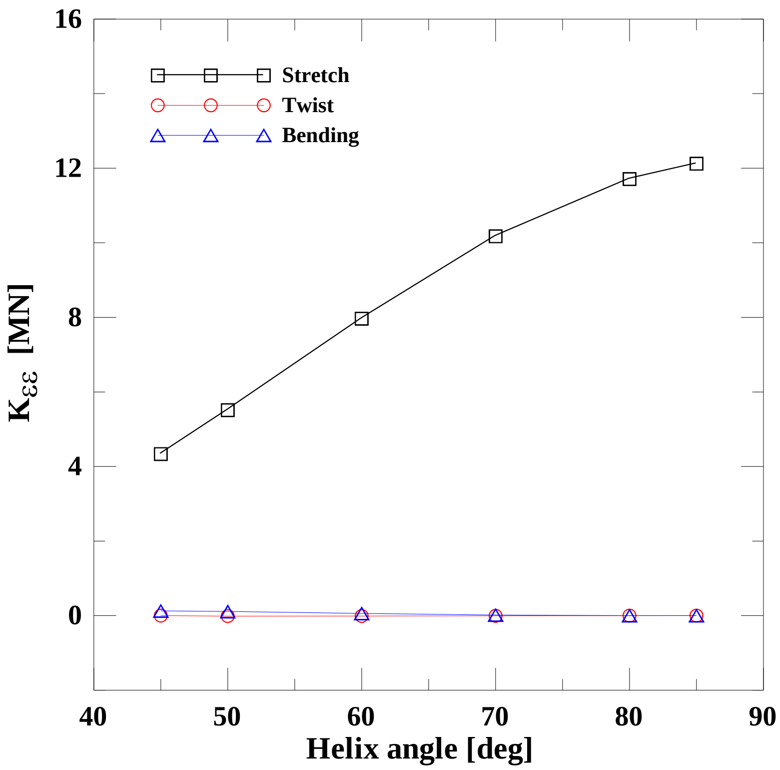
16
12
8
4
0
40
50
60
70
80
90
Stretch
Twist
Bending
K$_{\varepsilon\varepsilon}$ [MN]
Helix angle [deg]

(a)

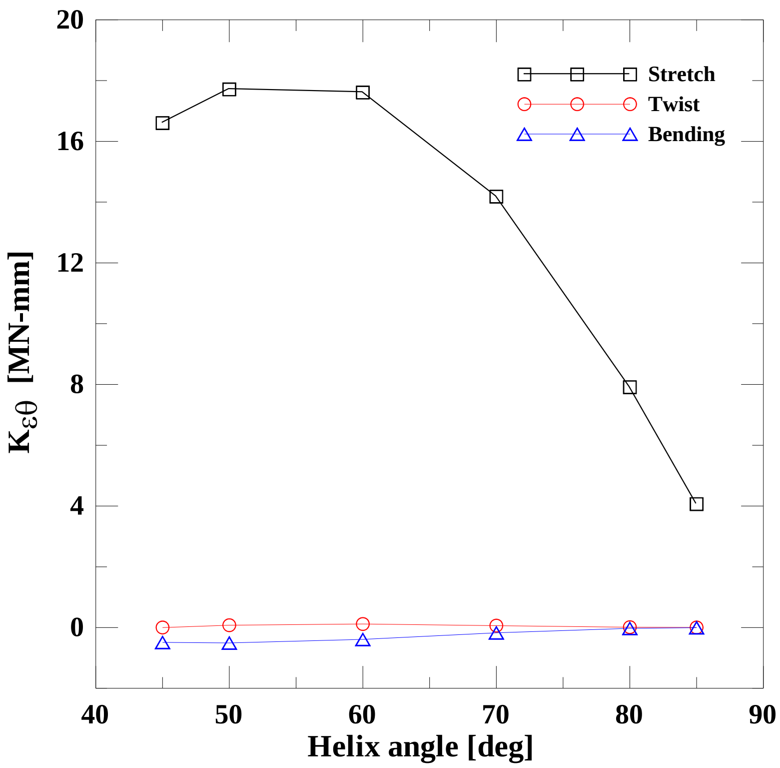
20
16
12
8
4
0
40
50
60
70
80
90
Stretch
Twist
Bending
K$_{\varepsilon\theta}$ [MN-mm]
Helix angle [deg]

(b)

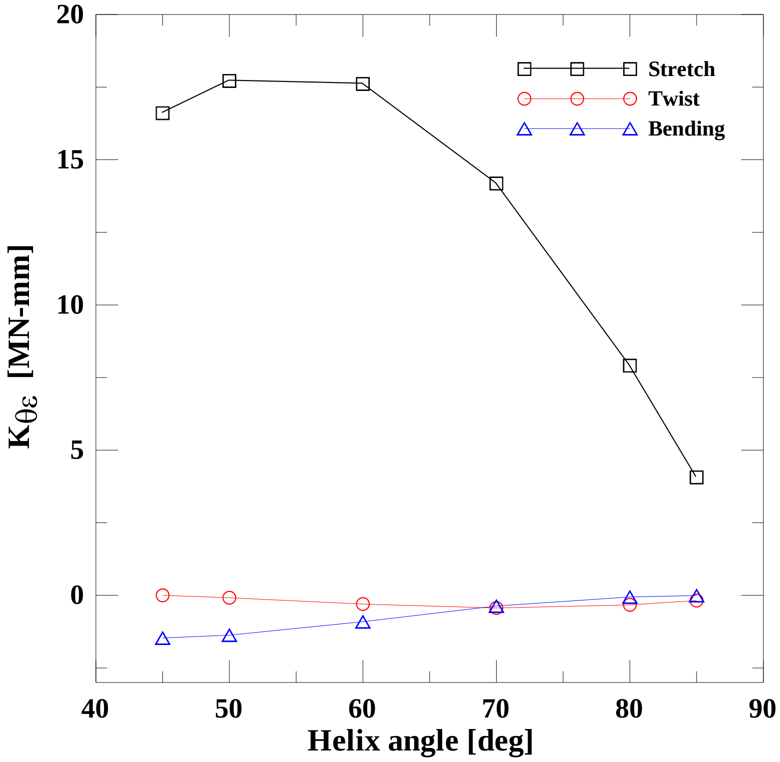

(c)

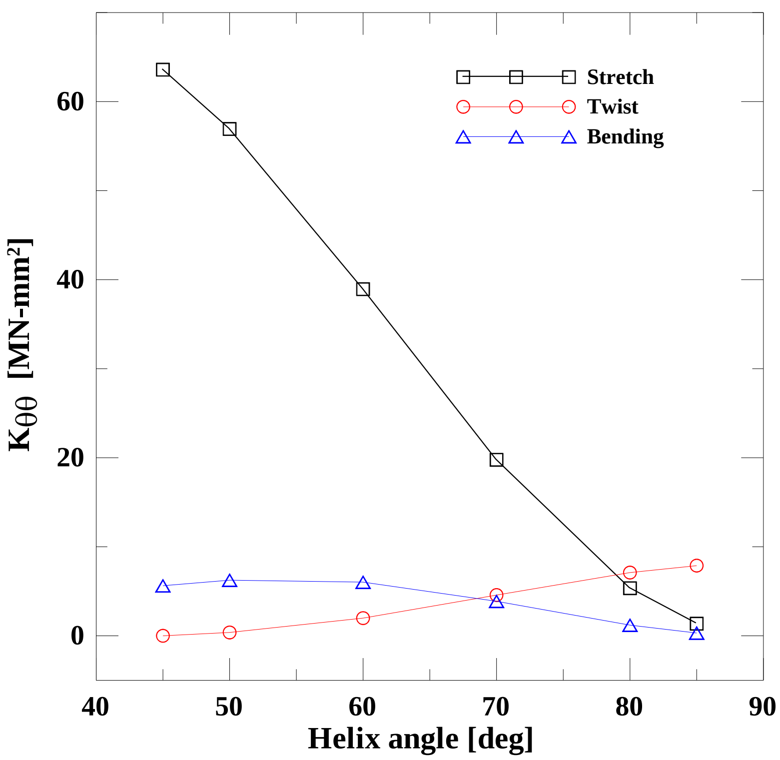

(d)

Fig. 2.2. Individual contribution by stretch, twist and bending to the cable stiffness. (a) Axial stiffness $K_{\varepsilon\varepsilon}$, (b) Coupling stiffness $K_{\varepsilon\theta}$, (c) Coupling stiffness $K_{\theta\varepsilon}$, (d) Twisting stiffness $K_{\theta\theta}$.

2. 5 Bending of a helically stranded cable

2.5.1 Costello's model

An initially straight helical wire with a helix angle, α, is subjected to a bending moment, M_s, which is applied about an axis perpendicular to the original axis of the wire. Fig. 2.3 shows such a wire.

Since the initial configuration of the wire is helical, and the initial curvatures and twist per unit length are

$$\kappa_{x0} = 0, \quad \kappa_{y0} = \frac{\cos^2\alpha}{r}, \quad \tau_0 = \frac{\sin\alpha\cos\alpha}{r}, \tag{28}$$

where r is the initial radius of the helix as shown in Fig. 2.1 (b) and, since the spring is subjected to a pure bending moment only, the following results from Fig. 2.1 (d):

$$f_x = f_y = f_z = m_x = m_y = m_z = F_x = F_y = F_z = 0. \tag{29}$$

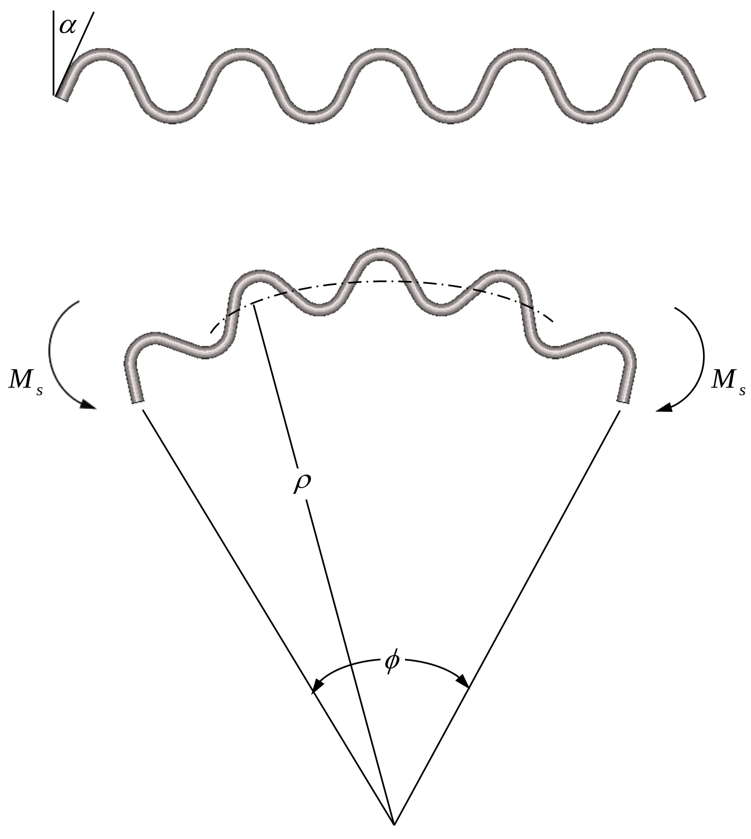

Fig. 2.3. Helical wire bent by bending moment

The equations of equilibrium Eqs. (16) through (21) from Fig. 1(d) yield

$$\frac{dM_x}{ds} - M_y\tau + M_z\kappa_y = 0, \tag{30}$$

$$\frac{dM_y}{ds} - M_z\kappa_x + M_x\tau = 0, \tag{31}$$

$$\frac{dM_z}{ds} - M_x\kappa_y + M_y\kappa_x = 0, \tag{32}$$

where κ_x, κ_y and τ are the final (deformed) curvatures and twist per unit length.

The bending and twisting moments M_x, M_y and M_z can be expressed as the following formulas:

$$M_x = \frac{\pi r_w^4}{4}E(\kappa_x - \kappa_{x0}), \quad M_y = \frac{\pi r_w^4}{4}E(\kappa_y - \kappa_{y0}), \quad M_z = \frac{\pi r_w^4}{4(1+\nu)}E(\tau - \tau_0), \tag{33}$$

By the Eqs. (28) and (33), the equilibrium equations [Eqs. (30) through (32)] can be written as

$$\frac{dM_x}{ds} - \frac{4}{\pi r_w^4 E}\nu M_y M_z - \frac{\sin\alpha\cos\alpha}{r}M_y + \frac{\cos^2\alpha}{r}M_z = 0, \tag{34}$$

$$\frac{dM_y}{ds} + \frac{4}{\pi r_w^4 E}\nu M_x M_z + \frac{\sin\alpha\cos\alpha}{r}M_x = 0, \tag{35}$$

$$\frac{dM_y}{ds} + \frac{4}{\pi r_w^4 E}\nu M_x M_z + \frac{\sin\alpha\cos\alpha}{r}M_x = 0. \tag{36}$$

Eqs. (34) through (36) constitute a nonlinear system of first-order ordinary differential equations that can be integrated numerically under suitable initial conditions. If these three equations are, respectively, multiplied by M_x, M_y and M_z and the resulting equations are added, the following results

$$\frac{1}{2}\frac{d}{ds}(M_x^2 + M_y^2 + M_z^2) = 0, \tag{37}$$

It is important to note that the magnitude of the resulting moment on any cross section is constant (independent of s).

Once Eqs. (34) through (36) are integrated numerically for M_x, M_y and M_z, Eq. (33) can be used to calculate the final curvature and twist.

Under the pure bending moment, M_s, applied perpendicular to the original axis of the helix, the wire behaves like a beam. The initially straight axis of the wire deforms into a circle of radius ρ with the angle ϕ as shown in Fig. 2.3.

For example, the case of ν =0. Eqs. (34) through (36) become linear and therefore have the solution

$$M_x = C_1 \cos ks + C_2 \sin ks, \tag{38}$$

$$M_y = -C_1 \sin\alpha \sin ks + C_2 \sin\alpha \cos ks + \frac{\cos\alpha}{\sin\alpha} C_3, \tag{39}$$

$$M_z = C_1 \cos\alpha \sin ks - C_2 \cos\alpha \cos ks + C_3, \tag{40}$$

where,

$$k = \frac{\cos\alpha}{r}\cdot \tag{41}$$

Let $M_x = M_s$, $M_y = 0$, $M_z = 0$ at $s = 0$. This yields

$$M_x = M_s \cos ks, \quad M_y = -M_s \sin\alpha \sin ks, \quad M_z = M_s \cos\alpha \sin ks. \tag{42}$$

The strain energy in the wire, U can be written as

$$\begin{aligned} U &= \int_0^l \left[\frac{\pi r_w^4 E}{4} (\kappa_x - \kappa_{x0})^2 + \frac{\pi r_w^4 E}{4} (\kappa_y - \kappa_{y0})^2 + \frac{\pi r_w^4 E}{4} (\tau - \tau_0)^2 \right] ds \\ &= \frac{1}{2} \int_0^l \frac{4}{\pi r_w^4 E} [M_x^2 + M_y^2 + M_z^2] ds = \frac{2}{\pi r_w^4 E} \int_0^l M_s^2 ds = \frac{2 M_s^2 l}{\pi r_w^4 E}, \end{aligned} \tag{43}$$

where l is the length of the wire.

When the work done by the bending moment M_s, is equated to the strain energy, the result is

$$\int_0^{\phi} M_s(\phi)d\phi = \frac{2M_s^2 l}{\pi r_w^4 E}\cdot \tag{44}$$

A differentiation of Eq. (44) yields

$$M_s = \frac{4M_s l}{\pi r_w^4 E}\frac{dM_s}{d\phi}, \tag{45}$$

an integration of Eq. (45) yields (since $M_s(0) = 0$)

$$M_s = \frac{\pi E r_w^4}{4l}\phi\cdot \tag{46}$$

$$h = l\sin\alpha, \tag{47}$$

where h is the length of the wire. Then Eq. (46) becomes

$$\frac{4M_s}{\pi E r_w^4 \sin\alpha} = \frac{\phi}{h} = \frac{1}{\rho}\cdot \tag{48}$$

The above equation is valid for $\nu = 0$.

When the exact solution for $\nu = 0$ is used in Picard's method to obtain a solution when $\nu \neq 0$, the following results

$$\frac{1}{\rho} = \frac{(2+\nu\cos^2\alpha)}{2\sin\alpha}\frac{4M_s}{\pi r_w^4 E}\cdot \tag{49}$$

Eq. (49) is valid for large changes in curvature. It should be noted that as α approaches 90°, the curvature $1/\rho$ approaches that of a straight beam.

When a straight stranded cable is bent into a circle of radius, ρ, and the cable is treated as an assemblages of helical wires, the following expression can be written

$$M_b = \frac{\pi E}{4}\left[\frac{2n\sin\alpha}{(2+\nu\cos^2\alpha)}r_w^4 + r_c^4\right]\frac{1}{\rho} = \frac{A^*}{\rho}, \tag{50}$$

where M_b is the total bending moment applied to the stranded cable, ρ is the radius of curvature of the stranded cable, n is number of wires, and r_c is the radius of the core. A^*, the bending stiffness of the stranded cable, is defined by the equation

$$A^* = \frac{\pi E}{4}\left[\frac{2n\sin\alpha}{(2+\nu\cos^2\alpha)} r_w^4 + r_c^4\right]. \tag{51}$$

It is important to note that the effect of ν is small on the value of the bending stiffness A^*. The stresses caused by bending are presented in Appendix B.

2.5.2 Semi-continuous model

A semi-continuous model is an approach in which each layer of a strand is mathematically represented by an orthotropic cylinder whose mechanical properties are selected to match the behavior of its corresponding layer of wires. A semi-continuous model is linearized to analyze the behavior of bending, stretching, twisting, and other complex loads. The stiffness matrix based on continuum mechanics and the elasticity model of the anisotropic material. The cylinder equivalent stiffness, contact force between the wires, inter-laminar shear, slippage, and other factors are considered. Using stress functions for cylindrically anisotropic elastic bodies, the analytic equations permit stiffness calculation of an assembly of coaxial cylinders.

The equivalent cable model stiffness matrix is as follows:

$$\mathbf{C} = \begin{bmatrix} \frac{1}{E_T} & -\frac{\nu_T}{E_T} & -\frac{\nu_L}{E_T} & 0 & 0 & 0 \\ -\frac{\nu_T}{E_T} & -\frac{1}{E_T} & -\frac{\nu_L}{E_T} & 0 & 0 & 0 \\ -\frac{\nu_L}{E_T} & -\frac{\nu_L}{E_T} & -\frac{1}{E_L} & 0 & 0 & 0 \\ 0 & 0 & 0 & \frac{1}{G_L} & 0 & 0 \\ 0 & 0 & 0 & 0 & \frac{1}{G_L} & 0 \\ 0 & 0 & 0 & 0 & 0 & \frac{1}{G_T} \end{bmatrix}, \tag{52}$$

where E_L is axial Young's modulus of the simplified model and E_T is tangential Young's modulus of the model. G_L and G_T are the shear modulus in the axial and tangential directions, respectively. ν_L and ν_T are the Poisson's ratios in the axial and tangential directions, respectively. The factor E_L is carried out by the ratio of the elliptical section areas of the n wires of the layer to the cylinder section area so that the axial stiffness that is considered an outer cylindrical structure will have the same axial stiffness as that of the cable structure.

$$\frac{E_L}{E_w} = \frac{nr_w}{4r_h \sin\alpha}, \tag{53}$$

where E_w is the Young's modulus of the outer layer of the model, r_w is the outer wire radius of the model, r_h is wire helix radius. When no gap exists outside in the direction of the tangential of the outer layers and when n is large enough, the ratio of Eq. (53) is $\pi / 4$.

Considering that the axial stiffness obtained by the ratio of cross-sectional areas is not sufficiently accurate especially when it used in bending calculation, E_L requires another approach when analyzing the bending behavior of cable structures. Assuming that the outer wires and the simplified cylindrical model have the same bending stiffness, the ratio of the inertia moment of layer wires to the inertia moment of the cylinder as follows:

$$\frac{E_L}{E_w} = \frac{nr_w}{8r(r_h^2 + r_w^2)\sin\alpha}\left(\frac{1+\sin^2\alpha}{2\sin^2\alpha} r_w^2 + 2r_c^2\right). \tag{54}$$

The deformation characteristics of the cable structure are considered during bending deformation in the model above. The maximum bending stiffness of the outer layer as

$$EI_{\max} = nE_w\left(I + \frac{1}{2}Ar_h^2\right)\sin^3\alpha, \tag{55}$$

As shown, the smaller α produces the less bending stiffness EI obtained Eq. (55).

2.5.3 Papiliou's model

This model considers the friction and slip between the wires. Bending stiffness changes with the curvature of the model in the axis direction when the cable model is bent. The value of bending stiffness is not constant but varies with the bending curvature and is applied to the cable model when tension varies. The bending stiffness of the model depends on the value of cable tension and curvature. In addition, the cable model having different bending stiffness values exhibits conventional nonlinear behavior.

In the process of bending wherein the friction effects for bending the cable model are considered, the deformation process generally involves three stages: stick, transition, and slip. As a common situation, the cable model of bending behavior is subjected to dynamic bending model calculations as well.

Assuming that no gap exists among wires in the tangential direction in the ideal cable structure, the outer layer and the core of the wire contact each other. Static friction is observed in the early stage. The slip force is insufficient to cause relative sliding between the wires. The bending stiffness of the cable structure is

$$EI_{stick}^{wire} = EA(r\sin\phi)^2 \sin^3\alpha \,. \tag{56}$$

When fully sliding without friction between wires, the bending stiffness of the cable is the minimum bending stiffness,

$$EI_{\min}^{wire} = E\frac{\pi r_w^4}{4}\sin\alpha \,. \tag{57}$$

Wire slip occurs between portions, i.e., portion slippage occurs, owing to the frictional force generated. Slip does not occur in the other part when the static friction is in the range,

$$EI_{slip}^{wire} = \sigma_T A(e^{\mu\cos\alpha\phi} - 1) r\sin\phi\sin\alpha / \kappa \,. \tag{58}$$

Therefore, the behavior of the cable model goes through different stages in the bending process, and bending stiffness has different expressions.

$$EI_{\max} = EI_{\min} + EI_{stick} = const \,, \tag{59}$$

$$EI = EI_{\min} + EI_{slip} = f(\kappa, F_T) \,. \tag{60}$$

3. Finite element models

Three different FE models were studied to simulate the mechanical behavior of helically stranded cable. We first considered a model for which 8-node, solid finite elements were used, and which has typically been used in most of the previous works. In this study, a beam model for which 2-node beam finite elements was used and a mixed FE model that consists of solid and beam finite elements were both developed.

In this section, the three FE models are explained in detail through the modeling of a straight 7-wire helically stranded cable comprising a central wire that is surrounded by six symmetrical helical wires, as shown in Fig. 2. 1 (a); the geometric and material properties (bilinear elastoplastic) are given in Table 2.2. The considered cable length for modeling is twice the pitch length.

The boundary and loading conditions are presented in Fig. 3.1 (a) and Fig. 3.2 (b). The left end is clamped and the right end is subjected to a force; like the experimental tests, both ends are then restrained against twist for the FE analyses [1–2]. The boundary conditions at the left end are given as

$$u_x = u_y = u_z = \theta_x = \theta_y = \theta_z = 0 . \tag{61}$$

Two cases of loading are considered at the right end: axial loading and transverse loading with pre-tension. As shown in Fig. 3.1 (a), the loading and boundary conditions at the right end for axial loading are

$$F_T = 120\text{kN},\quad u_x = u_y = 0,\quad u_z \neq 0,\quad \theta_x = \theta_y = \theta_z = 0 . \tag{62}$$

In the case of transverse loading(F_B) with pre-tension(F_T), as shown in Fig. 3.1 (b), the loading and boundary conditions at the right end are

$$F_B = 7\text{kN},\quad F_T = 10,\ 20,\ 30\text{kN},\quad u_x = u_y = 0,\quad u_z \neq 0,\quad \theta_x = \theta_y = \theta_z = 0 . \tag{63}$$

Notably, three different pre-tensions, 10kN, 20kN, and 30kN, are considered.

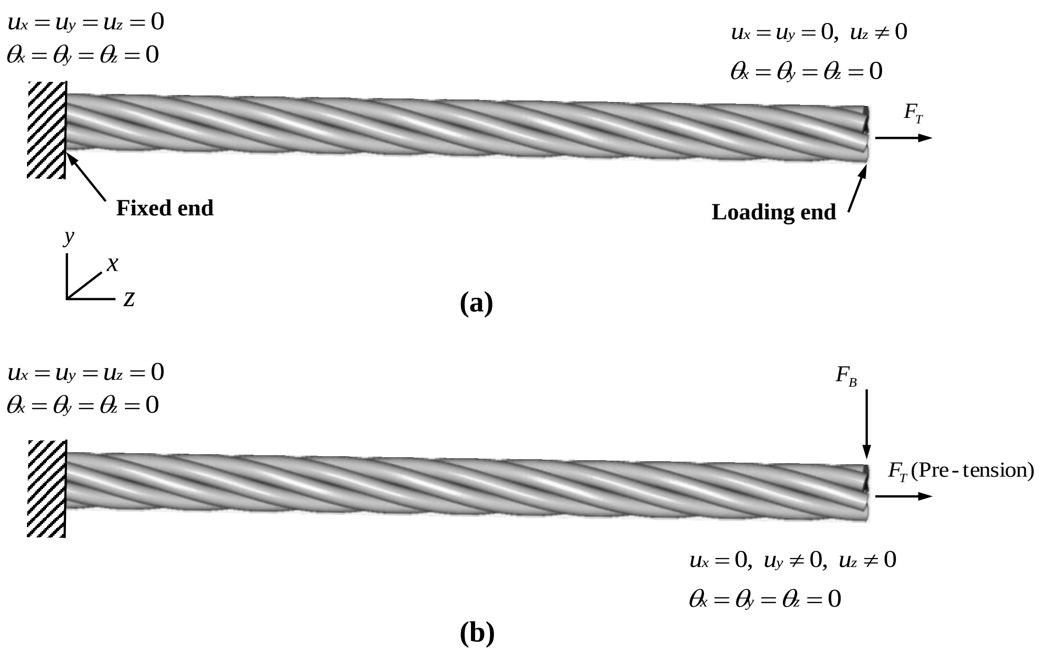

Fig. 3.1. Boundary and loading conditions for the 7-wire helically-stranded cable. (a) Axial load case(F_T :Axial load), (b) Transverse-load case(F_B : transverse load, F_T : pre-tension)

In the FE analysis model, one end-section of the cable is fully clamped. At the other end, the nodes corresponding to wires and core are rigidly linked using rigid link elements connected to a master node located at the cross-section center as shown in Fig. 3.2. Loads are applied at the master node and then conveyed to the whole section. Therefore, the end effects can be greatly reduced.

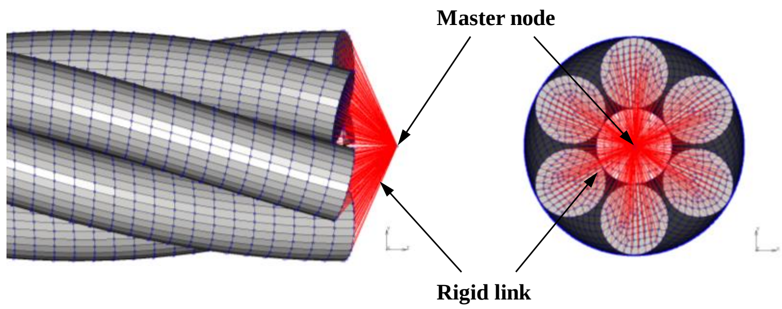

Fig. 3.2. Master node at the cross section center and rigid link.

At this point, it is important to understand the two types of physical contact that exist in helically stranded cables. First, line-to-line contacts that occur during deformation exist between the adjacent parallel wires within the same layer. The second type of contact occurs when the two wires of adjacent layers cross at an oblique angle, producing a point-to-point contact. Both types of contact should be properly modeled to perform the contact conditions accurately. ; furthermore, the elastoplastic material behavior needs to be considered for accurate modeling.

3.1 Full solid finite element model

For the full solid FE model, CATIA was used to obtain the core geometry through a linear z-axis extrusion, and the core was discretized by the 8-node solid elements. Each wire was generated through the extrusion of its cross-section along the helix that corresponds to the centroid line of the wire. Each wire (six in the outer layer) was then separately constructed in the same manner and positioned around the core, as shown in Fig. 3.3 (a). To accurately capture the radial contact between the individual wires, a relatively large number (28 elements in this study) of solid elements were used on the circumference direction to form a fine mesh in the wire cross-section, as shown in Fig. 3.3 (a).

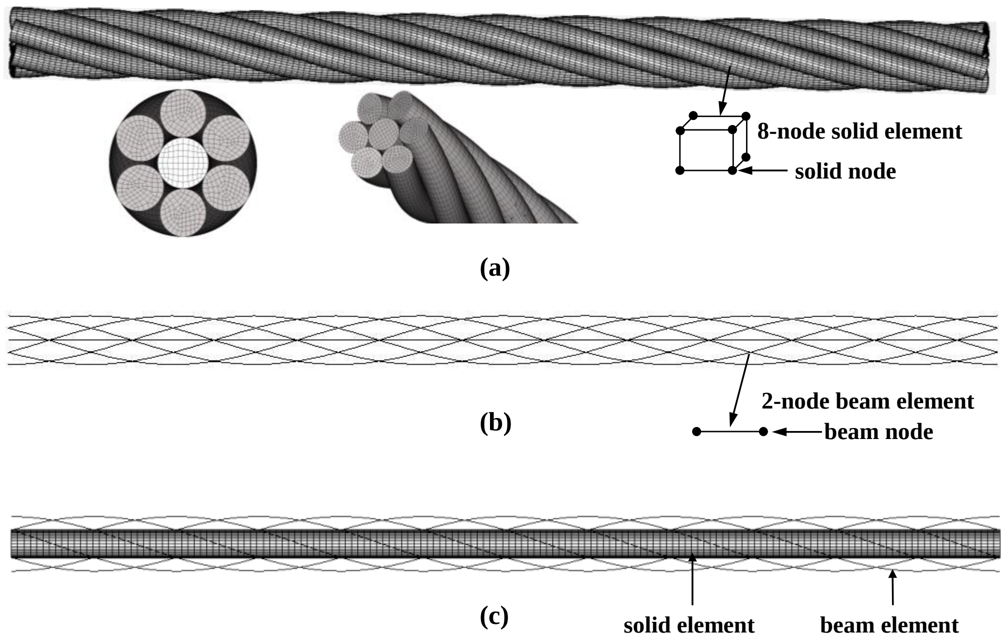

Fig. 3.3. Three FE models for the 7-wire helically-stranded cable. (a) Full solid FE model, (b) Beam FE model, (c) Mixed FE model (solid elements + beam elements)

To obtain a proper FE model with both desired accuracy and computational efficiency, we performed convergence studies to investigate the number of pitches to be modeled (model length) and mesh refinements required along the cable length considering the cable under axial loading. In this study, the equivalent stress (Von-Mises stress) at the core center and the maximum equivalent stress at core were investigated in the half length of the model. Note that the maximum stress occurs at contact points between the core and wires, due to both axial stress and transverse contact stress, as shown in Fig. 3.4 (a). The axial load applied was 100kN. In Figs. 3.4 (b) and (c), it is observed that the model length of at least two pitches is required and that the number of elements required per pitch length is more than 60.

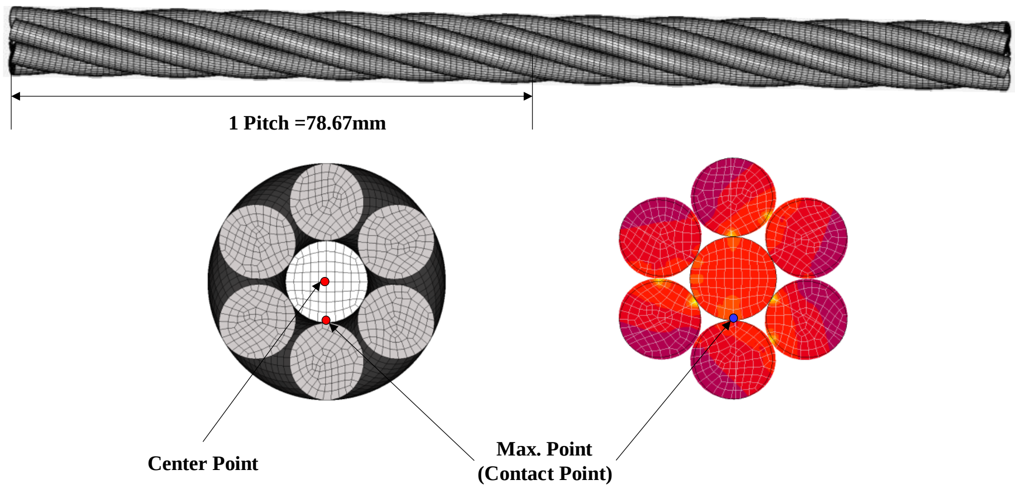
1 Pitch =78.67mm
Center Point
Max. Point
(Contact Point)

(a)

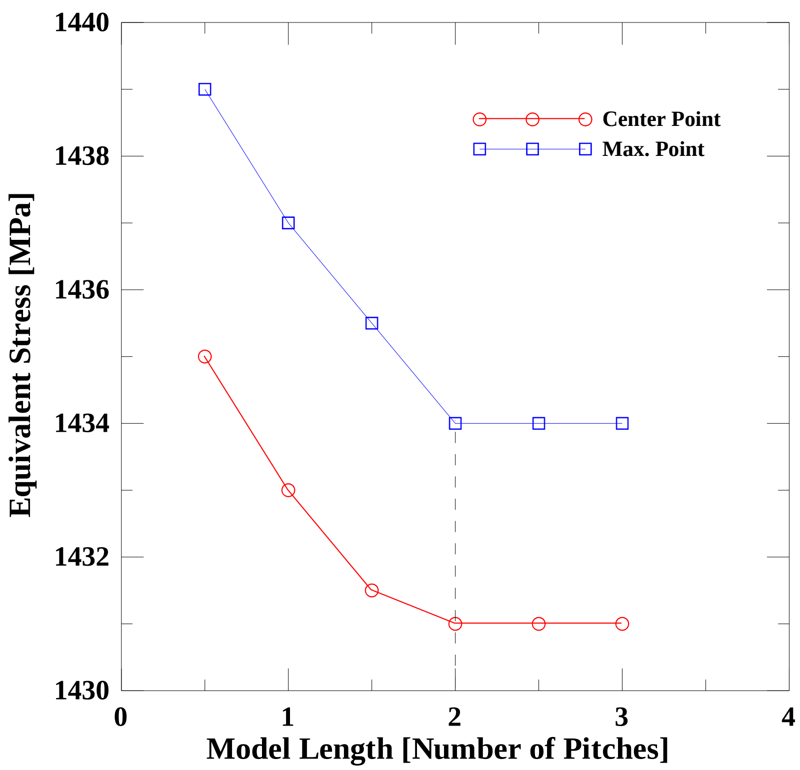
1440
1438
1436
1434
1432
1430
0
1
2
3
4
Equivalent Stress [MPa]
Model Length [Number of Pitches]
Center Point
Max. Point

(b)

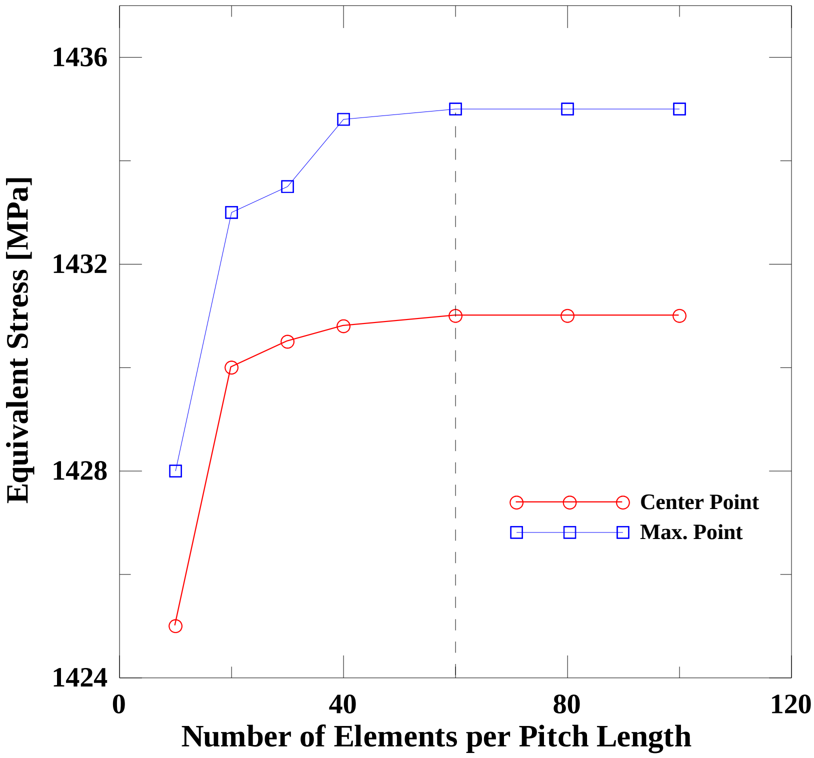

(c)

Fig. 3.4. Convergence of the equivalent stress calculated in the solid FE model. (a) Stress calculation points, (b) Model length, (c) The number of elements

Based on the convergence studies, we used 96,556 solid elements, 114,368 nodes, and 343,104 DOFs (Degree Of Freedoms). Extra care was taken to ensure that all six of the outer wires were just in contact with the core. By using the Coulomb friction model with a friction coefficient of 0.115, the friction-contact conditions were established between the wires and between the wires and the core.

3.2 Beam finite element model

The cable was modeled using multiple 2-node Timoshenko beam finite elements [20–24] that are positioned along the centerline of the core and each wire, as shown in Fig. 3.3 (b). The cross sectional area is πr_c^2 for the core and πr_w^2 for each wire. The moment of inertia is $\pi r_c^4/4$ for the core and $\pi r_w^4/4$ for each wire.

To construct a proper beam FE model, we also performed similar convergence studies to investigate the model length and the mesh refinement along the cable length. Equivalent stress at core center in the half length of the cable was considered, as shown in Fig. 3.5 (a). Figs. 3.5 (b) and (c) show that the minimum model length is two pitches and at least 40 elements per pitch length are required.

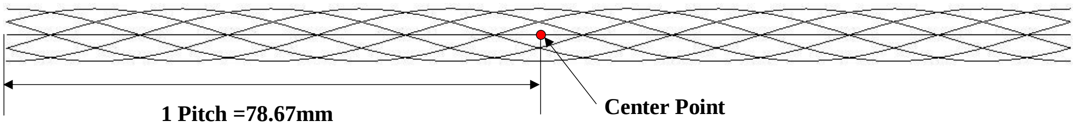

(a)

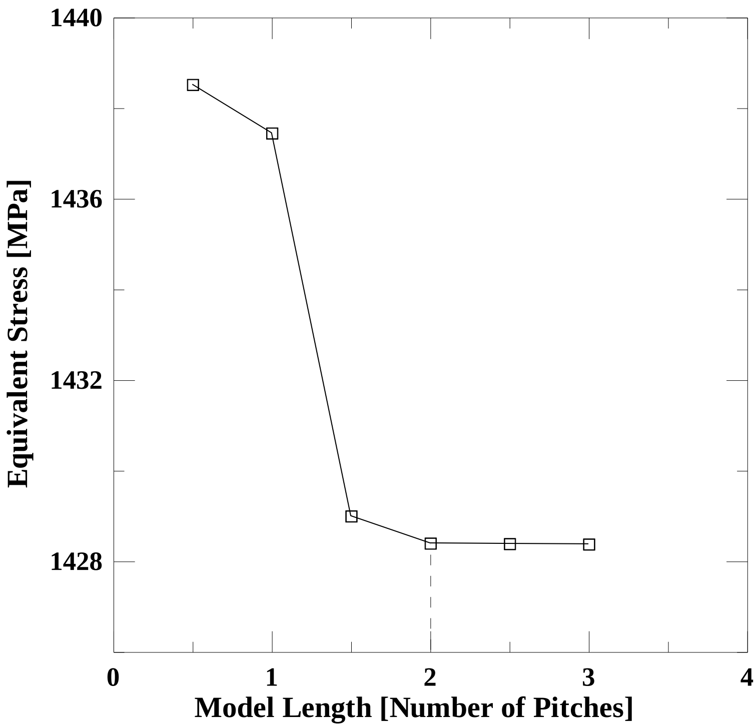

(b)

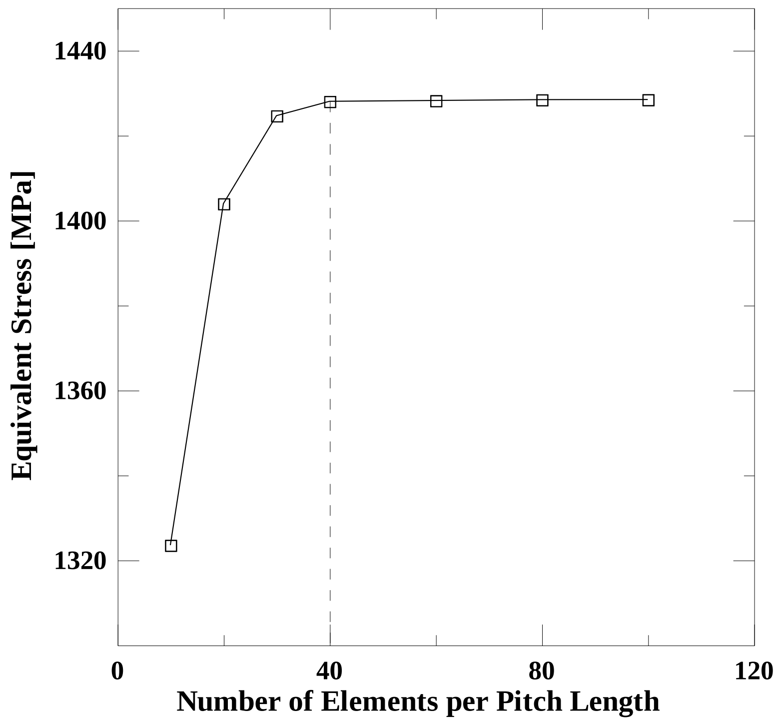

(c)

Fig. 3.5. Convergence of the equivalent stress calculated in the beam FE model. (a) Stress calculation points, (b) Model length, (c) The number of elements

The total numbers of beam elements, nodes, and DOFs were 1,099, 1,106, and 6,636, respectively. Only 1.93 % of the DOFs of the full solid FE model were used.

In this model, it is believed that the beam-to-beam contacts simulate the behavior of the core-wire contact and the wire-wire contact. Contact resolved between beams in the 3D space and is detected wherever contact occurs, not just between the beam nodes or beam node and a beam element. Contact algorithm creates an extra node at the contact point. Beam contact has to be activated in the contact detection form, the contact is detected using the following penetration function:

$$g = d - r_a - r_b + e \leq 0, \tag{64}$$

where d is the minimum distance between the beams, r_a and r_b are the radii of the beams (denoted by a and b, respectively), and e is the change of the beams that is due to the cross-sectional deformation, as shown in Fig. 3.6. During the contact-iteration procedure, the contact points between the beam elements can change if the elements slide with respect to each other; furthermore, the points in contact can move from one element to another. During such sliding, the corresponding friction should be taken into account.

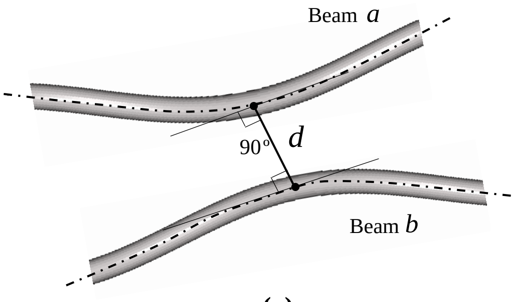

(a)

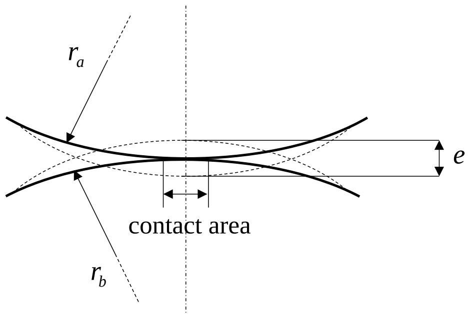

(b)

Fig. 3.6. Contact condition of circular beams (a) Closest points on two beams, (b) Contraction of radii of contacting bodies. r_a and r_b are the cross-section radii of the beams, respectively.

3.3 Mixed finite element model

Compared with a full solid FE model, a beam FE model is very effective in reducing computational cost; however, the advantage of the former is the attainment of detailed values such as local stress and the starting point of the yield in the individual wires. Since yield generally starts from the core, a mixed FE model wherein the solid elements were used to model the core and the beam elements were used to model the surrounding wires was considered for this paper, as shown in Fig. 3.2 (c); then, the advantages of both the solid FE and beam FE models can be obtained. Of course, in this model, the contact between the solid elements and the beam elements should be considered. In this model, the numbers of the solid and beam elements were 11,932 and 942, respectively, and the number of DOFs was 48,825.

4. Results and discussion

Considering the two loading cases for the 7-wire helically stranded cable, axial loading and transverse loading, the entire analysis procedure is static. In the axial loading analysis (Fig. 3.1 (a)), axial stretch and twisting occur, and the numerical results were compared to the analytical and experimental results [1, 5]. The transverse loading analysis (Fig. 3.1 (b)) was performed to predict the transverse behavior under different pre-tension levels.

4.1 Axial loading analysis

Fig. 4.1 presents the axial load-axial strain curves that were obtained from the use of the three different FE models, and they were compared to the experimental and analytical results [1, 5]. The predicted results of all of the models are in sound agreement with the experimental results, while the numerical results are compatible with the analytical results in the linear-elastic range.

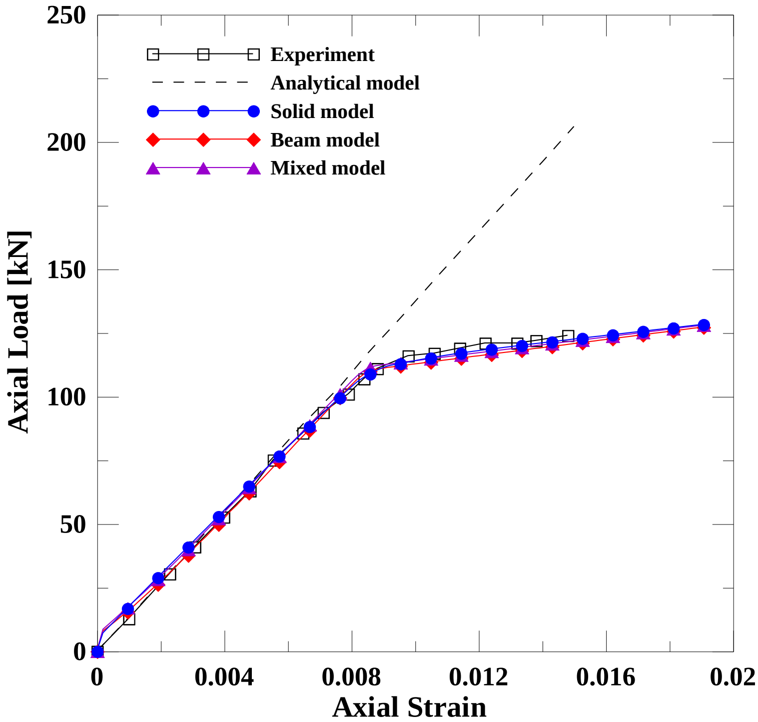

Fig. 4.1. Axial load-axial strain curves for the 7-wire helically stranded cable in the axial-load case.

Because the twist is constrained at both ends of the cable, reaction torques occur at the ends during the axial loading. Fig. 4.2 shows the axial load-torque curves up to an axial load of 90 kN. The results of the beam FE model closely agree with the experimental results. Notably, unlike the beam FE model, it is not easy to calculate the torque of the solid FE and mixed FE models, as the post-processing that is required is quite complicated.

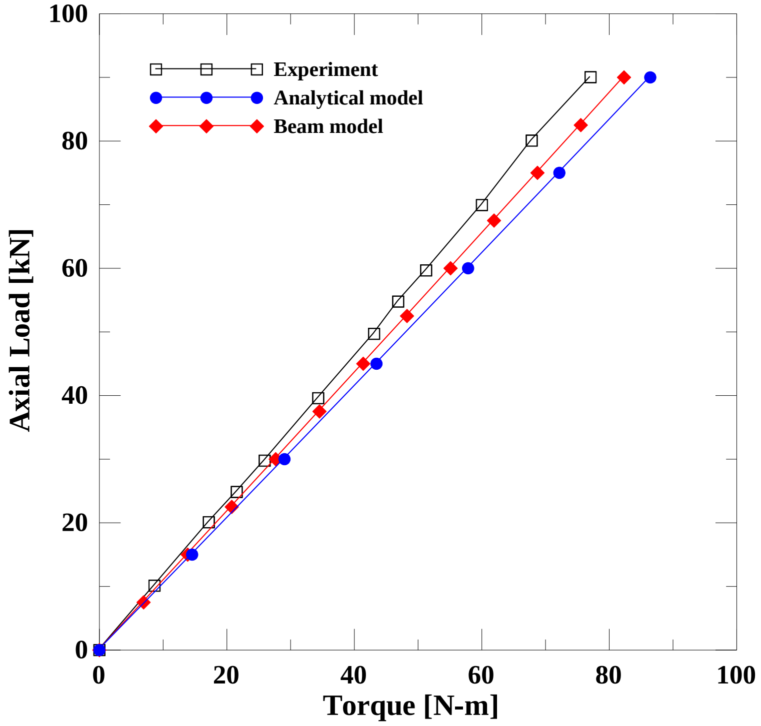

Fig. 4.2. Axial load-torque curves for the 7-wire helically stranded cable in the axial-load case.

Fig. 4.3 shows the displacement contours of the each FE model at ε =0.019, the beam model and mixed model have a good agreement with 3D solid model. Figs. 4.4 and 4.5 show the equivalent stress (Von-Mises stress) and longitudinal axial stress contours that were obtained with the use of the three FE models when ε =0.019. All of the wires already yielded (σ_Y =1540MPa) and are in the strain-hardening stage.

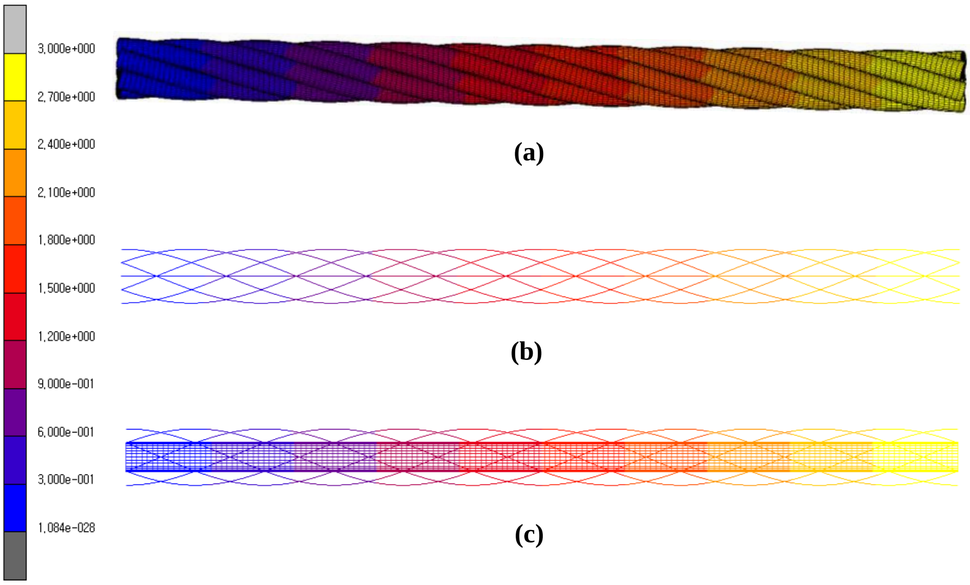

Fig. 4.3. Axial displacement contours obtained from the three FE models when axial strain ε =0.019. (a) Full solid FE model, (b) Beam FE model, (c) Mixed FE model

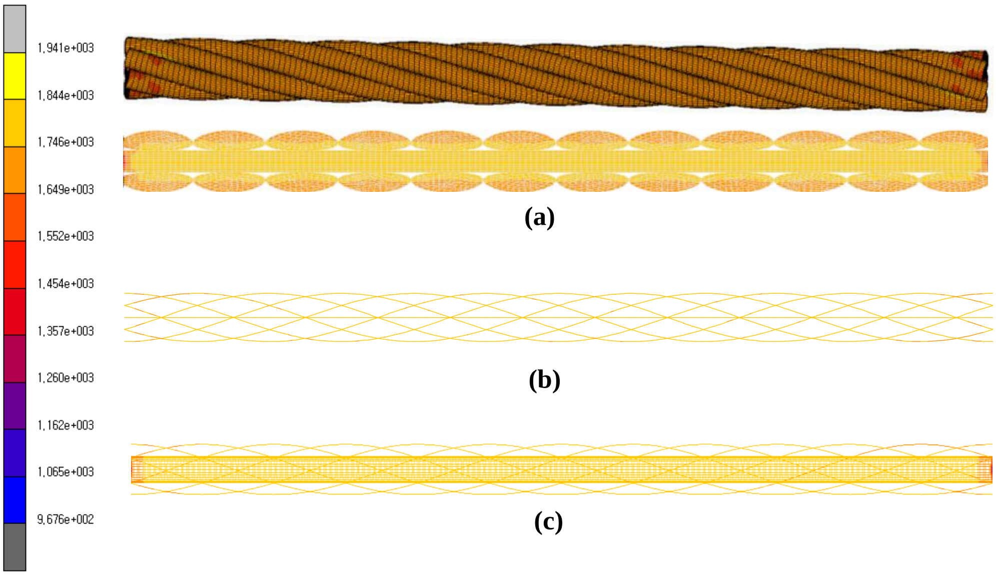

Fig. 4.4. Von-Mises stress contours obtained from the three FE models when axial strain ε =0.019. (a) Full solid FE model, (b) Beam FE model, (c) Mixed FE model

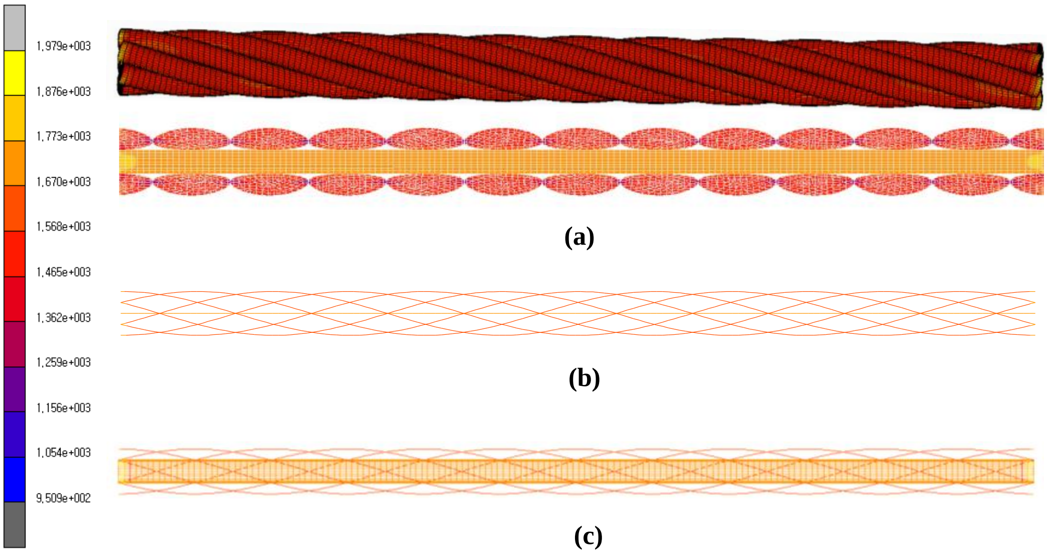

Fig. 4.5. Axial stress contours obtained from the three FE models when axial strain ε =0.019. (a) Full solid FE model, (b) Beam FE model, (c) Mixed FE model

The core is subjected to both axial stress and transverse contact stress that are induced by the continuous pressing of the helical wires onto the core under the diametrical contraction of the helically stranded wires; therefore, the maximum stress occurs in the core under axial loading and, compared to other wires, the core is reached first at the yield stress and the ultimate stress. The outer wires bear less stress than the core because of an unwinding, and this causes an early yielding in the core. The stress plots show the trend of the stress distributions under axial loading, helping the cable designer find the stress-intensity locations.

4.2 Transverse loading analysis

One end is clamped and the other is subjected to a transverse load with pre-tension. The following three different pre-tensions are considered: 10kN, 20kN, and 30kN. The transverse loading is applied up to 7kN.

Fig. 4.6 shows the transverse load-transverse displacement curves, whereby similar results are obtained with all three of the FE models. Fig. 4.7 illustrates the displacement contours of each FE model at 20kN pre-tension. All of the FE models show the same lateral deformation contours.

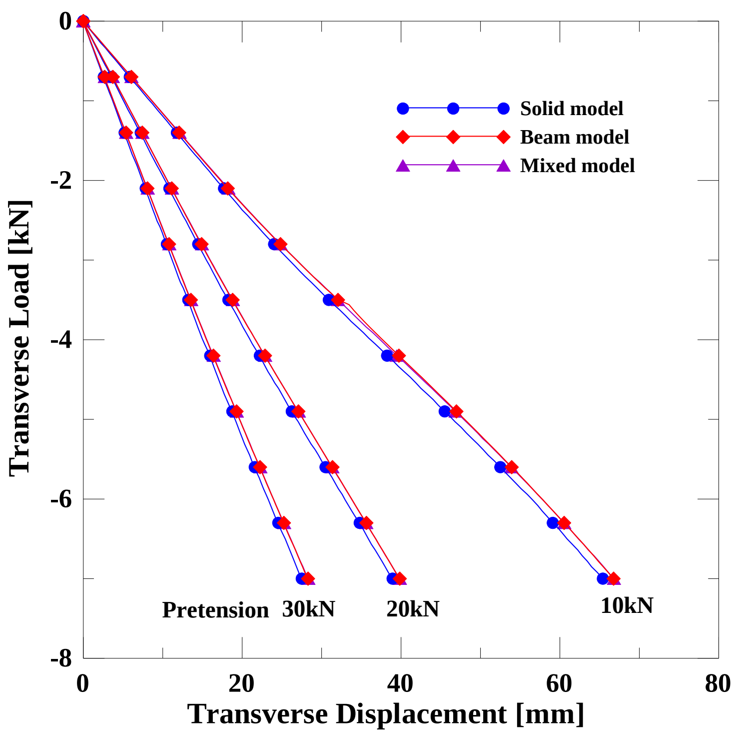

Fig. 4.6. Transverse load-transverse displacement curves for the 7-wire helically stranded cable in the transverse load case (Pre-tension = 10kN, 20kN, 30kN).

Figs. 4.8 and 4.9 illustrate the Von-Mises stress and axial stress contours of each FE model at a 20kN pre-tension. The stress concentration is located at the end areas, and all three FE models show similar levels of stress. Solid model and mixed model show the same stress contours, but it's not easy to compare them with beam model directly. However, the global stress level of beam model except for the area close to the fixed-end and loading-end is nearly the same with the other FE models.

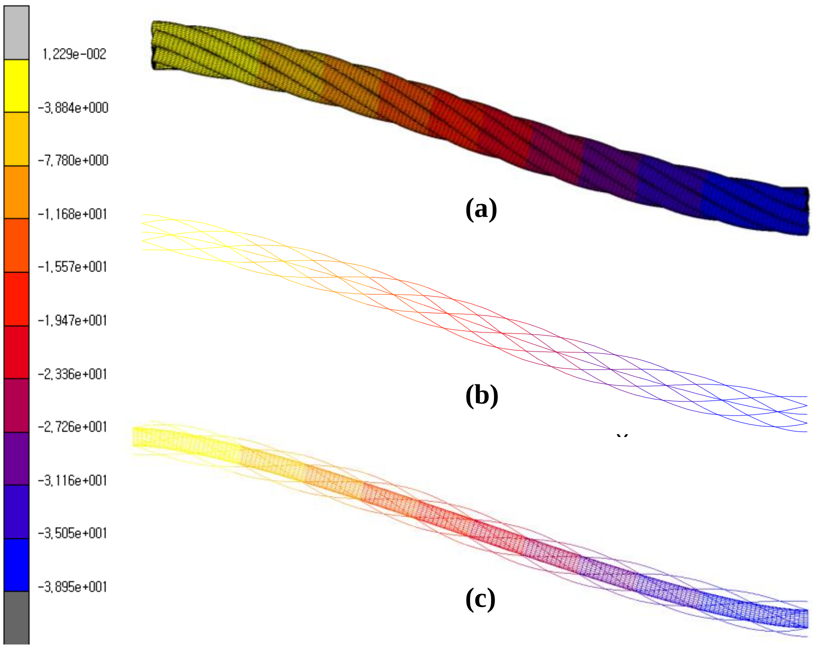

Fig. 4.7. Lateral displacement contours obtained from three FE models when pre-tension = 20kN and transverse load = 7kN. (a) Full solid FE model, (b) Beam FE model, (c) Mixed FE model

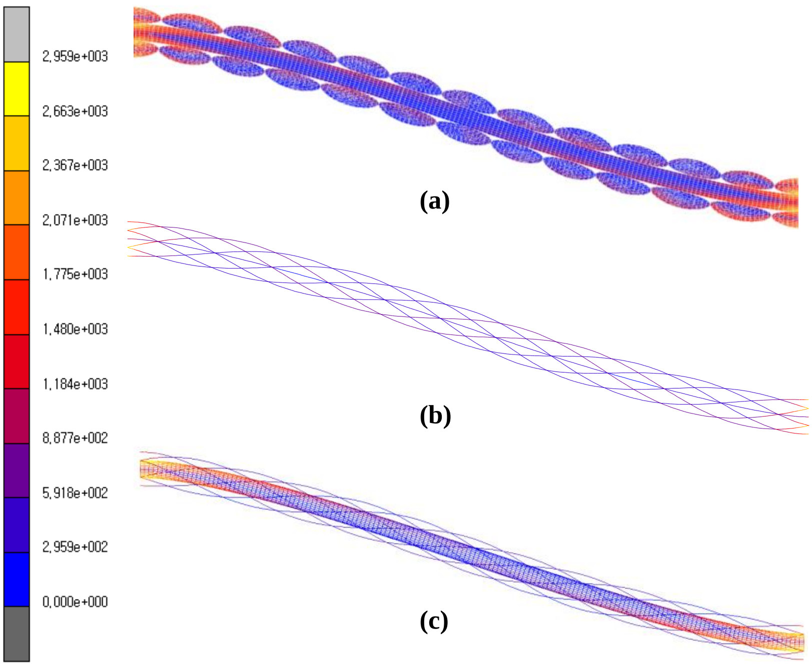

Fig. 4.8. Von-Mises stress contours obtained from three FE models when pre-tension = 20kN and transverse load = 7kN. (a) Full solid FE model, (b) Beam FE model, (c) Mixed FE model

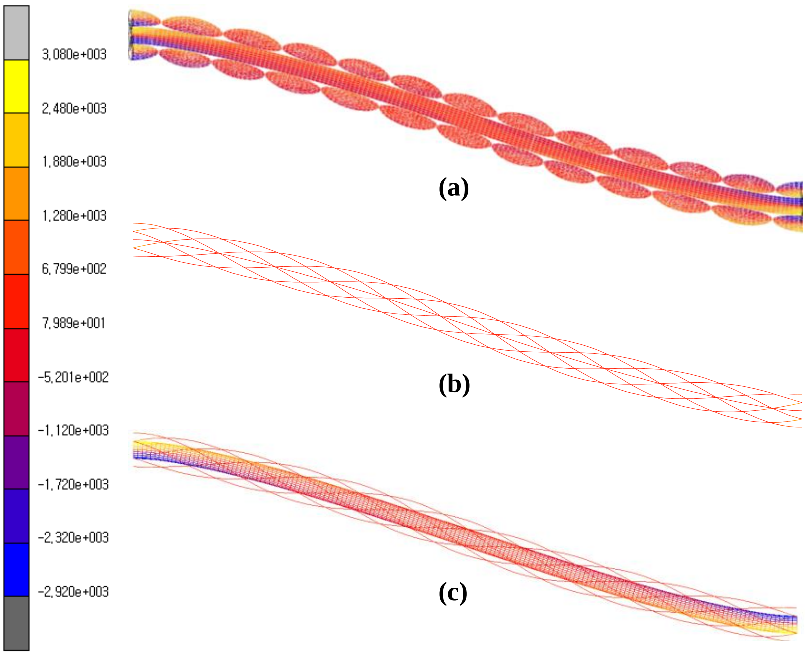

Fig. 4.9. Axial stress contours obtained from three FE models when pre-tension = 20kN and transverse load = 7kN. (a) Full solid FE model, (b) Beam FE model, (c) Mixed FE model

4.3 Influence of friction

4.3.1 Influence of friction model

Friction is a complex physical phenomenon and the most popular friction model is the Coulomb friction model which is used in this study. The coulomb model can be characterized by

$$\|f_t\| < \mu f_n \quad \text{(stick)}, \tag{65}$$

$$f_t = -\mu f_n \mathbf{t} \quad \text{(slip)}, \tag{66}$$

where f_t is the tangential (friction) force, f_n is the normal force, μ is the friction coefficient and $\mathbf{t}$ is the tangential vector in the direction of the relative velocity, $\mathbf{t} = v_r / \|v_r\|$, v_r is the relative sliding velocity.

For a given normal force, the friction force has a step function behavior based on the value of the relative sliding velocity v_r or the tangential relative displacement $\Delta\mathbf{u_t}$ as shown in Fig. 4. 10.

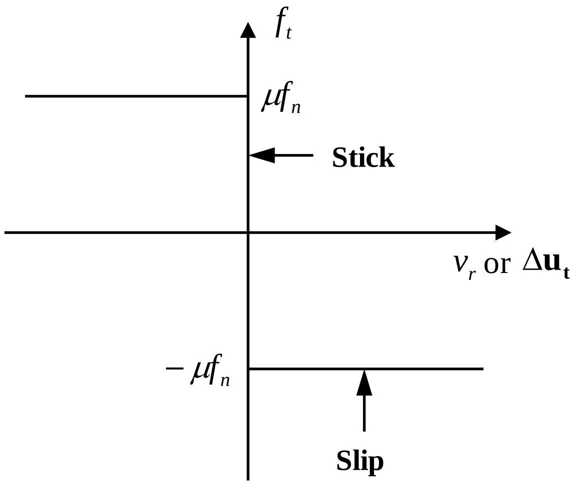

Fig. 4. 10. Coulomb friction model

Since this discontinuity in the friction value may easily cause numerical difficulties, different approximations of the step function have been implemented by user subroutine. They are graphically represented in Fig. 4. 11.

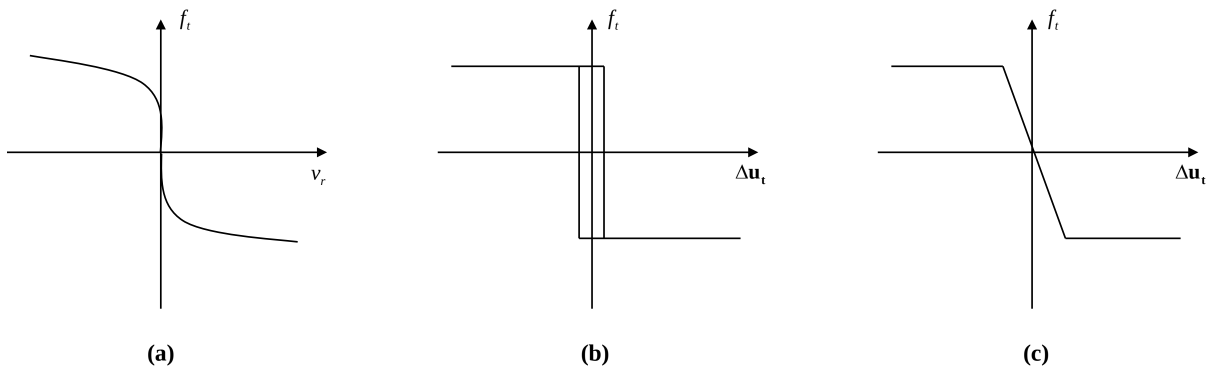

Fig. 4. 11. Different approximations of the Coulomb friction model for numerical analysis. , (a) Arctangent model, (b) Stick-slip (modified step function) model, (c) Bilinear model.

The arctangent model is based on a continuously differentiable function in terms of the relative sliding velocity, for the friction force

$$\mathbf{f_t} = -\mu f_n \frac{2}{\pi} \arctan\left(\frac{\|v_r\|}{R_v}\right)\mathbf{t}, \tag{67}$$

where the value of R_v is the value of the relative velocity below which sticking occurs. The value of R_v is important in determining how closely the mathematical model represents the step function as shown in Fig. 4. 12.

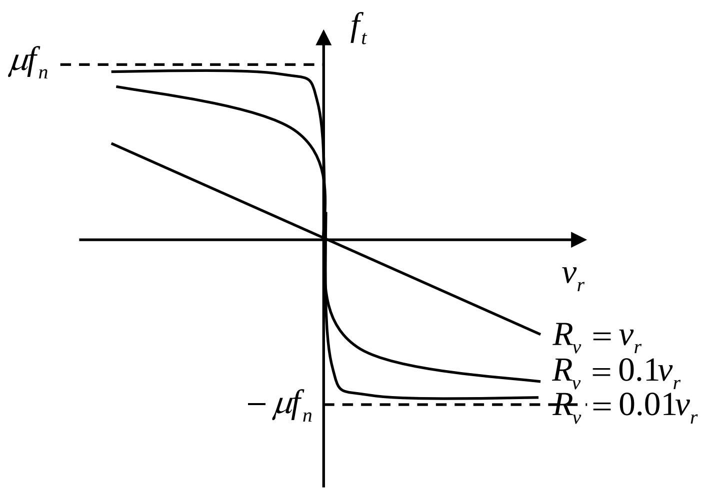

Fig. 4.12. Arctangent model for different value of R_v.

A very large value of R_v results in a reduced value of the effective friction, and a very small value may result in poor convergence. It is recommended that the value of R_v be 1% to 10% of a typical relative sliding velocity, $\|v_r\|$. The analysis result for 7-wire helically stranded cable was almost same regardless of the range of R_v from 1% to 10% of relative sliding velocity. Thus, the value of R_v is selected as 10% of relative sliding velocity considering computational cost in this paper.

During iteration of the Newton-Rapson process, the change of the friction force $\delta \mathbf{f}_\mathbf{t}^i$ is related to the change of the relative sliding velocity, δv_r^i, is defined as follows :

$$\delta v_r^i = \frac{\Delta \mathbf{u}_\mathbf{t}^\mathbf{i} - \Delta \mathbf{u}_\mathbf{t}^{\mathbf{i}-1}}{\Delta t} = \frac{\delta \mathbf{u}_\mathbf{t}^\mathbf{i}}{\Delta t} . \tag{68}$$

Stick-slip model is based on a slightly modified step function and can be used to simulate true stick-slip behavior. In this procedure, each node in contact gets a friction status, being either stick or slip. The slip to stick transition region β is introduced as a tolerance on the friction solution as shown in Fig. 4.13.

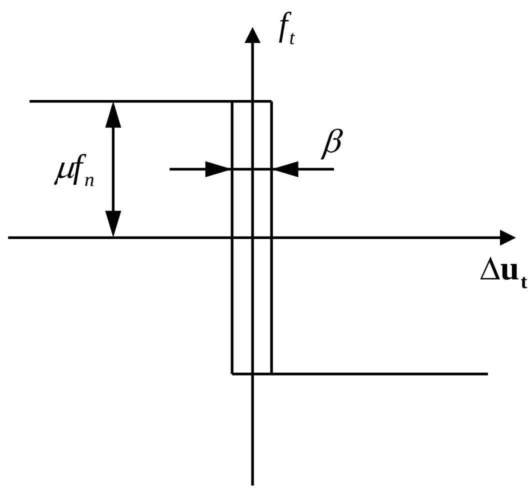

Fig. 4.13. Stick-slip (modified step function) model with friction parameter β.

If a node is in slipping mode and moves in the direction of the friction force, but the corresponding relative displacement magnitude is within the slip to stick transition, then this will not cause the increment to be started with modified friction conditions. A large value of β gives a poor numerical result with friction, and a very small value may result in poor convergence. Thus, the value of β is selected as 1×10^{-6} in this paper.

The bilinear model is similar to the modified step function model, it is based on relative tangential displacements. The bilinear model assumes that the stick and slip conditions correspond to reversible (elastic) and permanent (plastic) relative displacement, respectively. The friction is expressed by a slip surface Φ:

$$\Phi = \|\mathbf{f_t}\| - \mu f_n . \tag{69}$$

The stick domain is given by $\Phi < 0$. The rate of the relative tangential displacement vector is split into an elastic (stick) and plastic (slip) contribution according to:

$$\dot{\mathbf{u}}_t = \dot{\mathbf{u}}_t^e + \dot{\mathbf{u}}_t^p , \tag{70}$$

and the rate of change of friction force vector is related to the elastic tangential displacement by

$$\dot{\mathbf{f}}_t = \mathbf{D}\dot{\mathbf{u}}_t^e , \tag{71}$$

where matrix $\mathbf{D}$ is given by

$$\mathbf{D} = \begin{bmatrix} \frac{\mu f_n}{\delta} & 0 \\ 0 & \frac{\mu f_n}{\delta} \end{bmatrix}, \tag{72}$$

with δ the slip threshold or relative sliding displacement below which sticking is simulated as shown in Fig. 4.14. The value of δ is selected as 0.0025 considering the average edge length of the finite elements defining the deformable contact bodies in this paper.

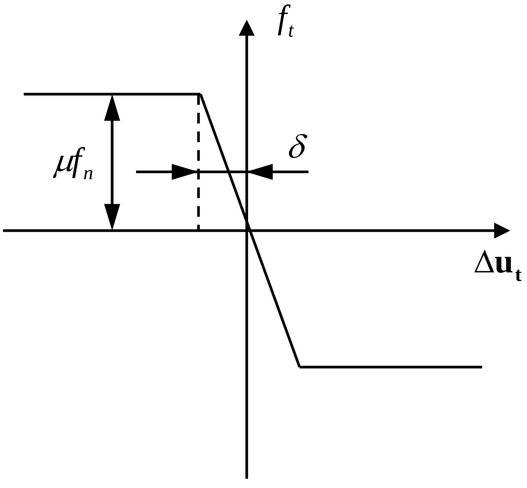

Fig. 4.14. Bilinear model with slip threshold δ.

The influence of the friction model was verified using above three models in the solid FE model. The axial loading conditions were considered in the parametric study. Fig. 4. 15 shows that the global response under axial load is almost the same regardless of the type of friction models. This observation indicates that the influence of friction models on the global behavior of the cable is small.

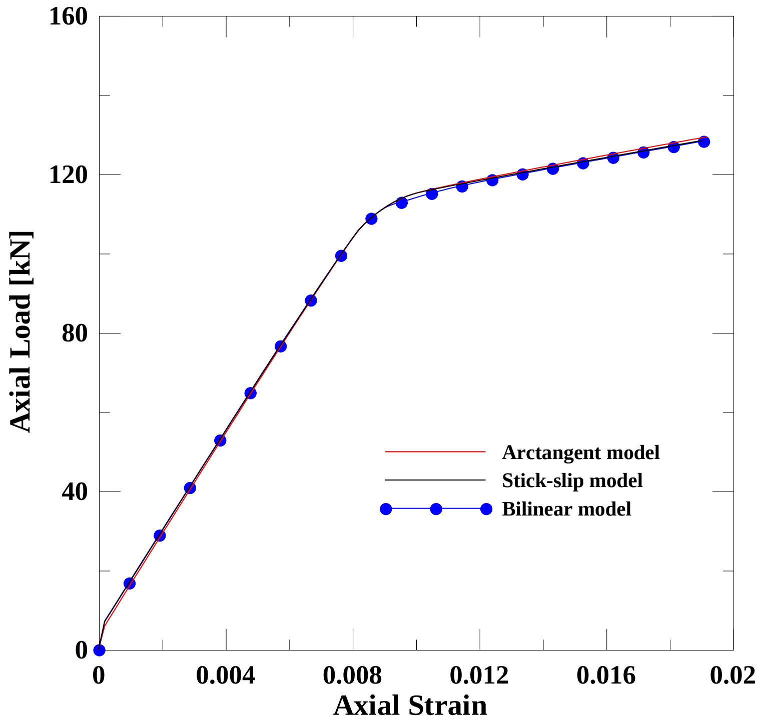

Fig. 4.15. Influence of three different friction models under axial load.

Table 4.1 presents computational time required for each model. The arctangent model requires approximately 123% and the stick-slip model requires 112% of computational time compared to the bilinear model. Therefore, the bilinear friction model is an effective for the FE analysis of helically-stranded cable in terms of computational efficiency.

Table 4.1. Computational time required for analyses of the 7-wire helically stranded cable where three different friction models are used.

Friction model	Arctangent model	Stick-slip model	Bilinear model
Computational time [sec]	26,308 [123%]	23,916 [112%]	21,450 [100%]

4.3.2 Influence of friction coefficient

The friction coefficient in this study was used 0.115, which was experimentally obtained [25]. This value was also used in the numerical models proposed in Refs. [14, 17]. It is well known that the range of the coefficient is from 0.1 to 0.4 [17, 25]. We here verify the influence of the friction coefficient considering five different values, 0.0, 0.05, 0.115, 0.2, and 0.4 in the solid FE model. The axial and transverse loading conditions were considered in the parametric study.

Figs. 4. 16 (a) and (c) show that the global responses under both axial and transverse loads are almost the same regardless of friction coefficients. This observation indicates that the influence of friction coefficients on the global behavior of the cable is small. Figs. 4. 16 (b) and (d) show that, as the friction coefficient increases, the equivalent stresses at core center and the maximum stress decrease. However, the decrease is not large within the range of friction coefficients from 0.1 to 0.4. Nevertheless, it should be mentioned that while the friction effect plays a small role in global behavior of such cables, the effect of friction on the long-term performance and durability of a structure under cyclic loading can be significant.

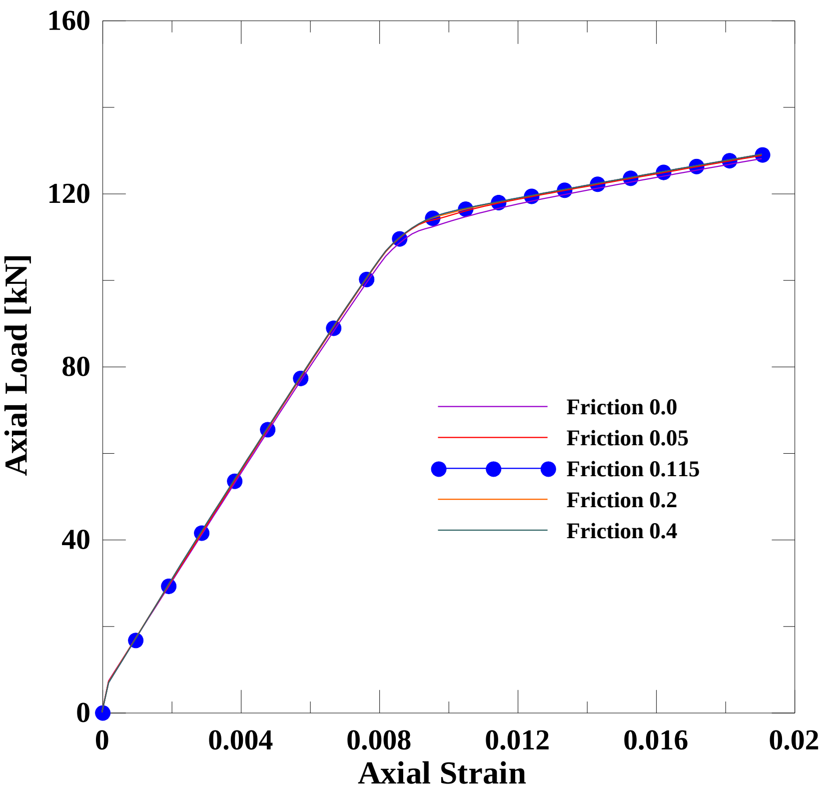

(a)

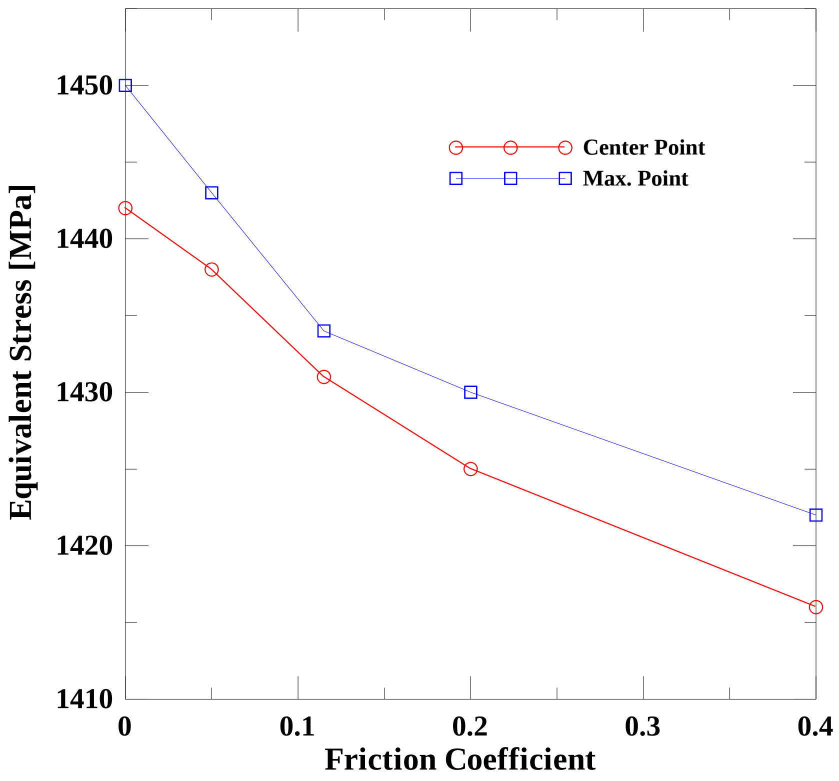
1450
1440
1430
1420
1410
Equivalent Stress [MPa]
Center Point
Max. Point
0
0.1
0.2
0.3
0.4
Friction Coefficient

(b)

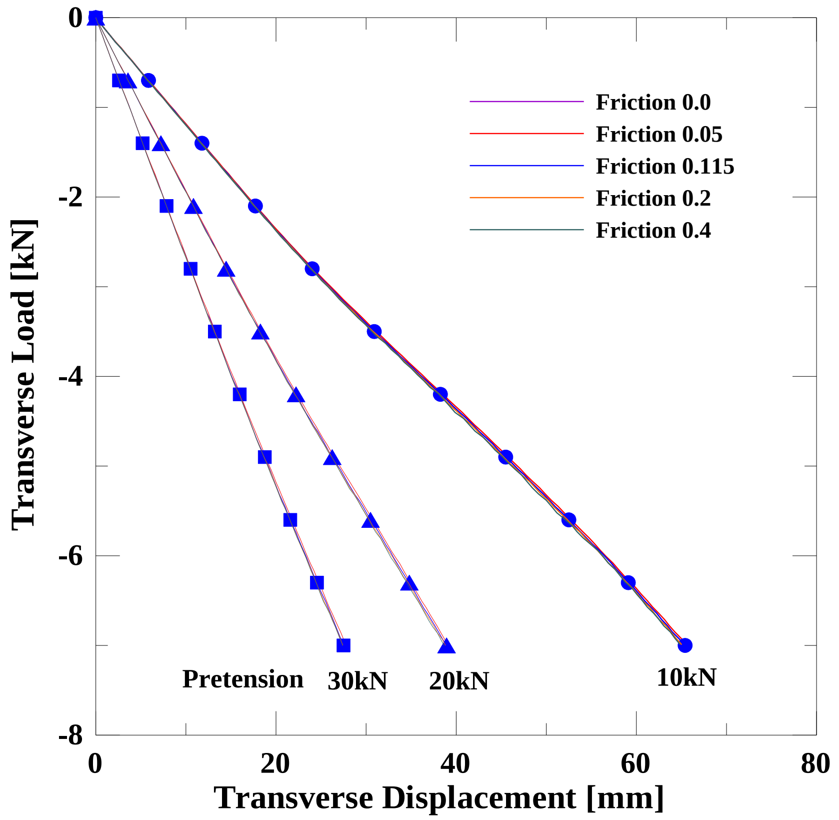
0
-2
-4
-6
-8
Transverse Load [kN]
Friction 0.0
Friction 0.05
Friction 0.115
Friction 0.2
Friction 0.4
Pretension
30kN
20kN
10kN
0
20
40
60
80
Transverse Displacement [mm]

(c)

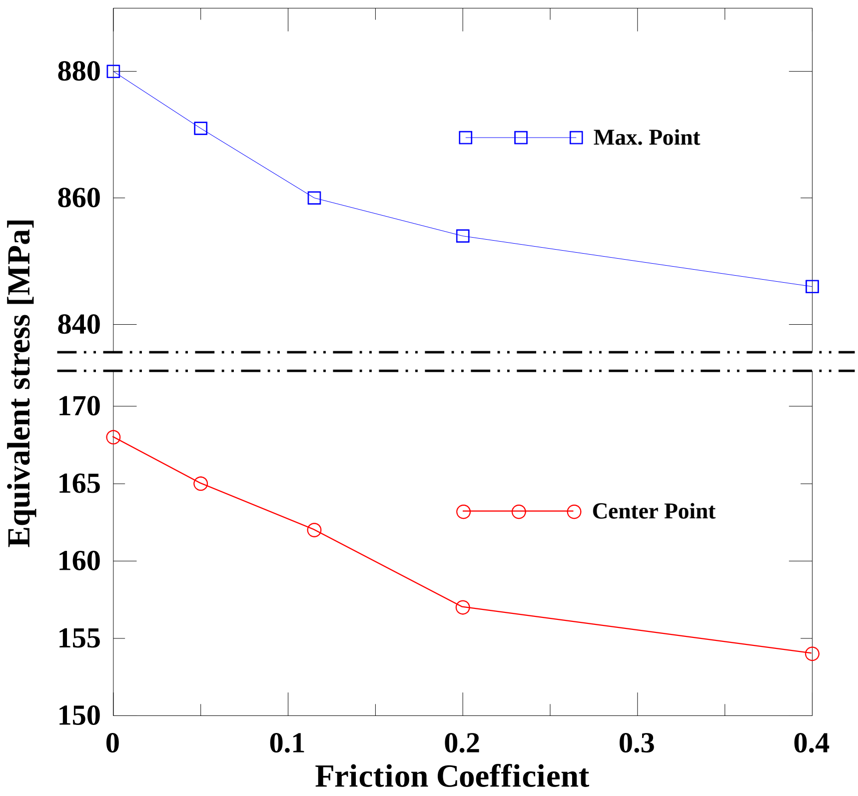

(d)

Fig. 4.16. Influence of friction coefficients under axial load and transverse load (a) Load-strain curve under axial load, (b) Equivalent stress under axial load, (c) Load-displacement curve under transverse load, (d) Equivalent stress under transverse load

4.4 Remarks on computational cost and accuracy

The required computational time for the analysis of the 7-wire helically stranded cable in both loading cases was measured. A personal computer (Intel Xeon® CPU E5-1620 V3 @3.5 GHz Dual Core Processor, RAM 32GB) was used to perform all of the computations.

The full solid FE model requires approximately six hours and four hours for the axial loading and transverse loading cases, respectively, while the beam FE model only requires approximately 17 minutes and 19 minutes, respectively. Table 4 shows the computational time required for each model.

Considering the geometry modeling and the mesh generation, the cost of the solid FE model is significantly greater than that of the beam FE model. Computational efficiency is a very important factor for designers in the cable industry; therefore, the beam FE model is a very effective for the prediction of the mechanical behavior of helically-stranded cables in terms of computational efficiency.

Table 4. 2. Computational time required for analyses of the 7-wire helically stranded cable where three different FE models are used.

FE model	Number of Elements	Number of DOFs	Computational time [sec]	
			Axial load	Transverse load
Solid model	96,556 [100%]	343,104 [100%]	21,450 [100%]	13,445 [100%]
Beam model	1,099 [1.1%]	6,636 [1.9%]	999 [4.7%]	1,121 [8.3%]
Mixed model	12,874 [13.3 %]	48,825 [14.2 %]	3,193 [14.9 %]	1,745 [13.0 %]

We then compared equivalent stresses calculated using three FE models for a 7-wire helically stranded cable. The equivalent stress at core center and the maximum equivalent stress at core were investigated in the half length of the model as shown in Fig. 5(a). The stresses were obtained at 100kN axial load and 7kN transverse load with pre-tension of 10kN.

Table 4.3 shows the stresses calculated using three FE models. Basically, the levels of stress are similar but, as expected, the stresses calculated using the solid model are larger than those obtained using other models. The results indicate that the beam FE model is useful for predicting the global behaviors of cables, but the solid and mixed FE models are appropriate for investigating the local behaviors of cables such as stress concentrations, local yielding stress, and detailed contact stress.

While the solid FE model shows detailed local-stress distributions, the advantage of the beam FE model is a high cost-efficiency, and the mixed FE model shows detailed stress distributions in the core with reasonable cost-efficiency. Therefore, cable designers need to choose an FE model appropriate for the purpose of the design.

Table 4.3. Equivalent stresses calculated using three FE models.

FE model	Center point [MPa]		Maximum point [MPa]	
	Axial load [100kN]	Transverse load [7kN]	Axial load [100kN]	Transverse load [7kN]
Solid model	1431	162	1434	860
Beam model	1428	159	1428	851
Mixed model	1431	161	1433	858

4.5 Validity of analytical solutions

In order to find the validity of the analytical solutions, we performed general comparisons for helix angle varying between 55° and 87.5°, the stiffness matrix component values obtained both using the analytical models and beam FE model have been compared.

The stiffness coefficients in beam FE model are computed in four successive steps corresponding to different loading condition in tension and torsion. Considering Eq. (1),

$K_{\varepsilon\varepsilon}$: Axial load F_T is applied and the change of twist angle $\delta\theta$ is set to zero.

$K_{\theta\theta}$: Torsion M_T is applied and the change of axial stretch δh is fixed to zero.

$K_{\varepsilon\theta}$: Axial load F_T is applied with a free twist angle.

$K_{\theta\varepsilon}$: Torsion M_T is applied with a free axial stretch.

Fig. 4.17 shows the axial stiffness value, $K_{\varepsilon\varepsilon}$, obtained by different analytical models as well as beam FE model, versus helix angle. The axial stiffness values of analytical models are almost same each other, but a little higher than those of beam FE model. For the large helix angle ($\alpha \geq 75°$), the results of all analytical models have a good agreement with the beam FE model (within 2.2% of each other).

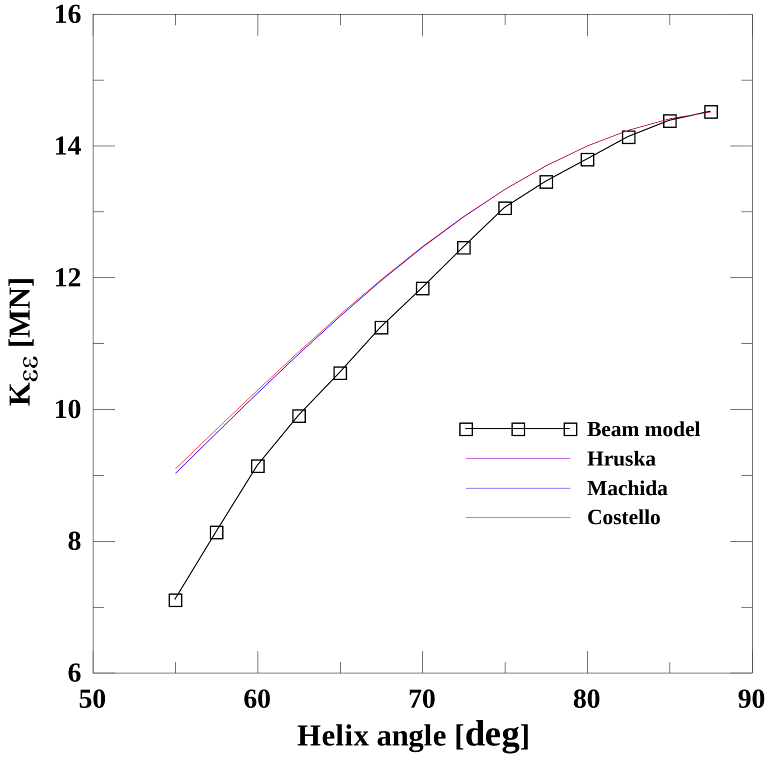

Fig. 4.17. Axial stiffness $K_{\varepsilon\varepsilon}$ versus Helix angle α curves for the 7-wire helically stranded cable.

Fig. 4.18 shows the torsion stiffness value, $K_{\theta\theta}$, versus helix angle. As shown in Fig. 4.18 the model of Hruska gives results appreciably lower than the others, because the torsional stiffness of the wires is neglected as presented in eq. (25c). All the other analytical models provide very similar results, the difference increases slightly with decreasing helix angle. For $\alpha \geq 62.5°$, the agreement between the analytical models (except Hruska's model) and beam FE model are very close.

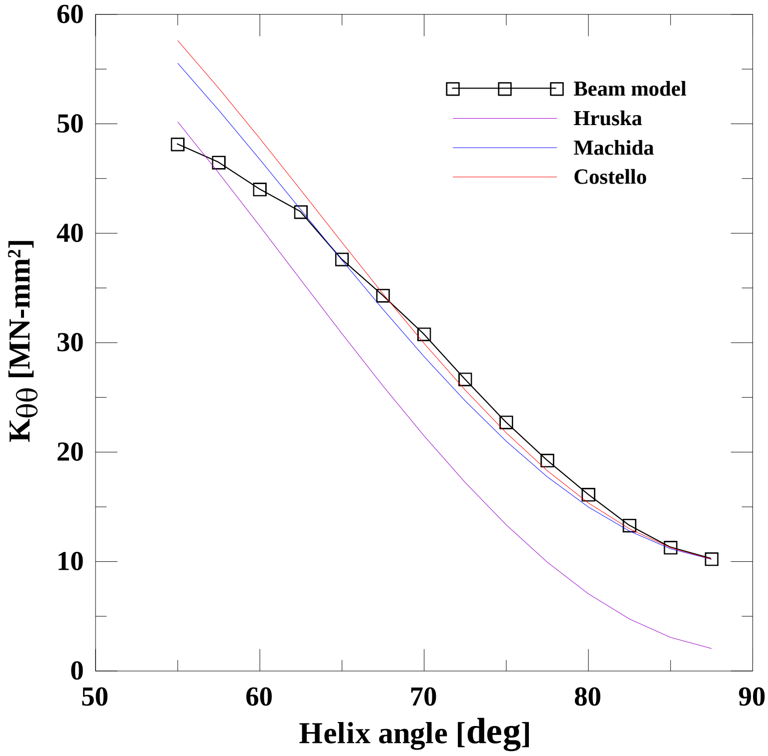

Fig. 4.18. Torsional stiffness $K_{\theta\theta}$ versus Helix angle α curves for the 7-wire helically stranded cable.

The stiffness value of the coupling terms, $K_{\varepsilon\theta}$ and $K_{\theta\varepsilon}$, versus helix angle are shown in Figs. 4.19 (a) and (b). For $K_{\varepsilon\theta}$, the difference increases with decreasing the helix angle. For a large helix angle ($\alpha \geq 75°$), the agreement with the FE model is good and the difference is within 5%. Below this α value, a significant difference appears.

For $K_{\theta\varepsilon}$, the Hruska model has same stiffness value with $K_{\varepsilon\theta}$ because it has symmetrical matrix terms ($K_{\varepsilon\theta}$ = $K_{\theta\varepsilon}$) while the Machida and Costello models have different value with $K_{\varepsilon\theta}$. As shown in Fig. 4.19 (b), the Machida and Costello models have a good agreement with beam FE model at $\alpha \geq 70°$.

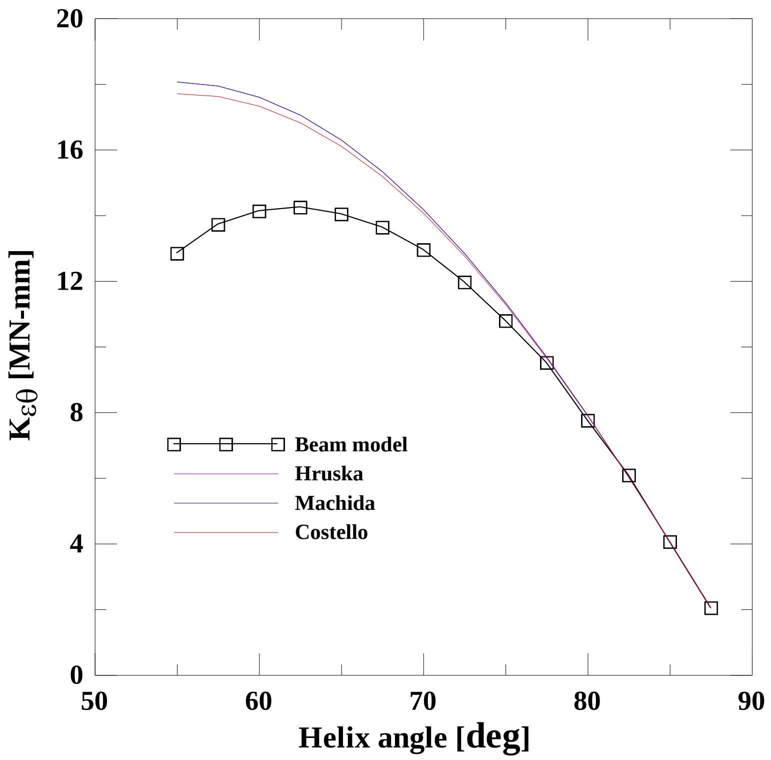

(a)

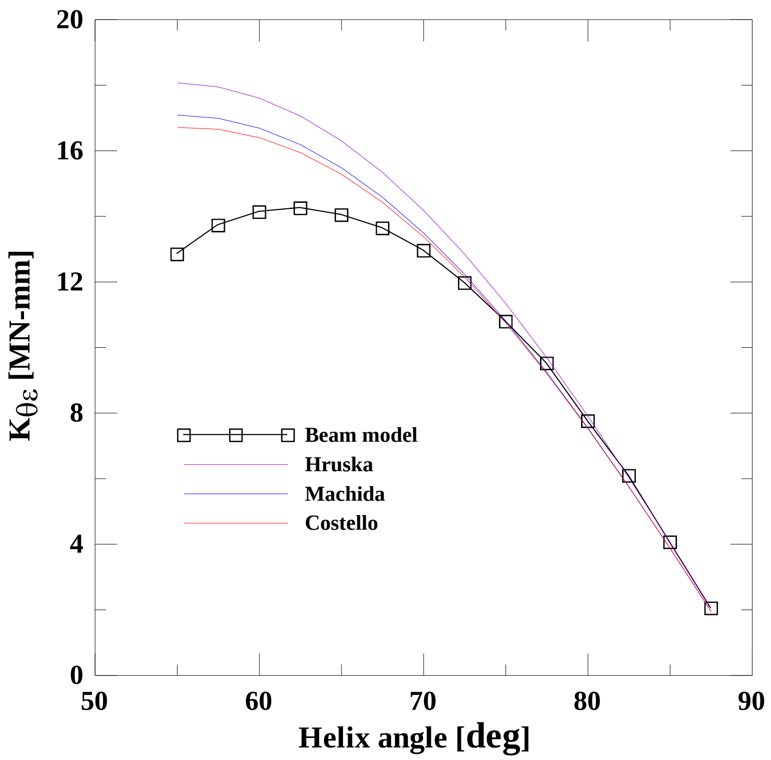

(b)

Fig. 4.19. Coupling stiffness $K_{\varepsilon\theta}$ and $K_{\theta\varepsilon}$ versus helix angle α curves for the 7-wire helically stranded cable.

In conclusion, the relative differences of stiffness values between analytical models and beam FE model are less than 5% for the helix angle beyond 75°. But, the differences grow significantly for α value below 75°, the analytical models are too approximate for the analysis of 7-wire helically stranded cable. This can be a good information for the cable designers when they select a design tool for cable design.

5. Torque balance design of helically stranded cables

During axial loading, the helical wires, which render the cable flexible, induce a twisting of the stranded cable that can be undesirable in several ways. Cable twisting may loosen some wires and tighten others depending on the helix directions, so that some of the layers will be stressed at higher levels and the breaking strength of the cable could be considerably reduced. Long cables that are restrained from twisting may develop a large induced torque, whereby slight relaxations of the cable tension (momentary slack cable) can result in hockling (looping) due to the corresponding instability.

To prevent undesirable cable twisting, external torque needs to be applied; however, a more favorable solution is the prevention or minimization of such twisting behavior by properly designing the cable layer composition. It is possible to find the “torque balance design” that is a suitable geometry between the adjoining layers of a multilayered stranded cable that yields no twisting and no torque. For torque balance design, $\delta\theta / h = 0$ and $M_T = 0$ in Eq. (1) and thus $K_{\theta\varepsilon}$ in Eq. (1) and Eqs. (25b), (26c) and (27c) are equal to zero. Our goal is to find a layer composition and geometry that result in $K_{\theta\varepsilon} = 0$.

For torque balance design, there are available several analytical models [26–30], in which dimensionless parameters are adopted. However, such analytical models are only useful for designing cables with relatively simple geometry. In this study, the use of the beam FE model is proposed for the torque balance design. The beam FE model can be used for a design of cable with a complicated geometry, while the desirable accuracy and a computational efficiency are also achieved. Of course, full solid FE model can be used for torque balance design, but their practical use is limited due to the excessive computational cost. In the following sections, a design procedure for which the beam FE model is used is explained through demonstrations of the torque balance designs of two layer and three layer cables.

5.1 Two layer cable

To create the torque balance condition in a two layer cable, as shown in Fig. 5.1, the torque of layer 1 should be equal and in the opposite direction to that of layer 2 . Here, the helix angles of both layers are defined as the design parameters; that is, the helix angles need to be determined for the torque balance, while the other properties (the geometric and material properties of the cable, and the boundary conditions including the contacts) are fixed. This methodology has been widely and effectively used in common cable design practices.

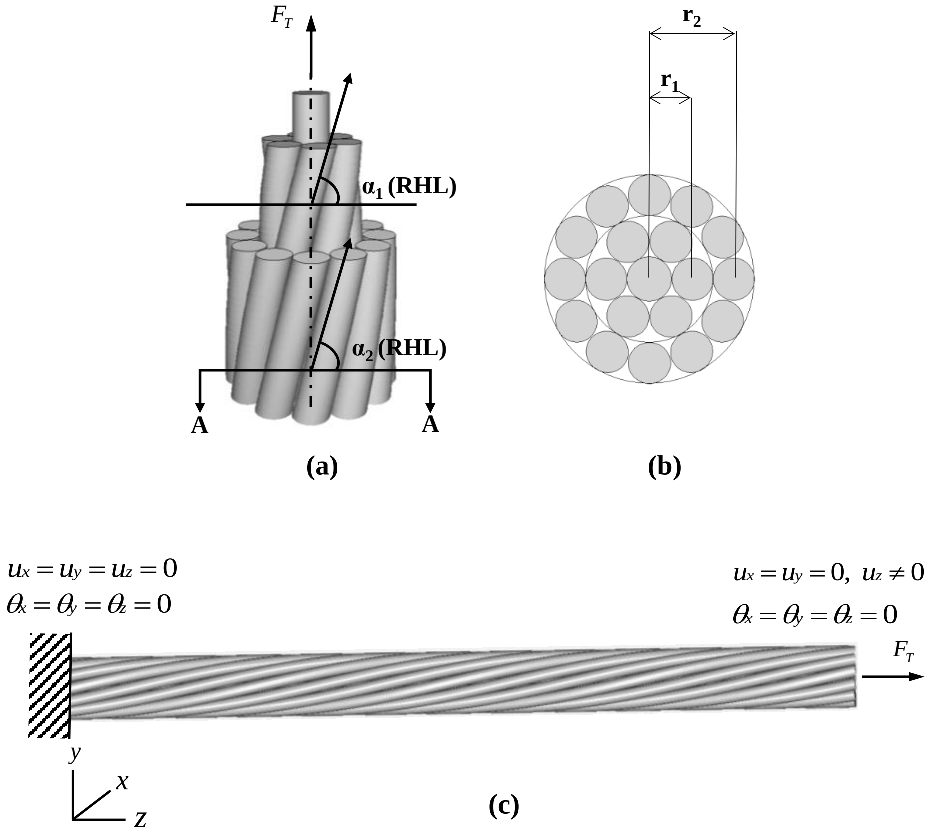

Fig. 5.1. Geometry of the two-layer cable (1 + 6 + 12 structure). α_1: helix angle of layer 1; α_2: helix angle of layer 2.

A two-layer cable consists of 19 helically stranded wires (1 + 6 + 12). Fig. 5.1 shows the geometric and boundary conditions, Fig. 5.2 shows the beam FE model for the prediction of the torque, and Table 5.1 presents the geometric and material properties of the cable. Coulomb friction model with a friction coefficient of 0.115 was used in this model.

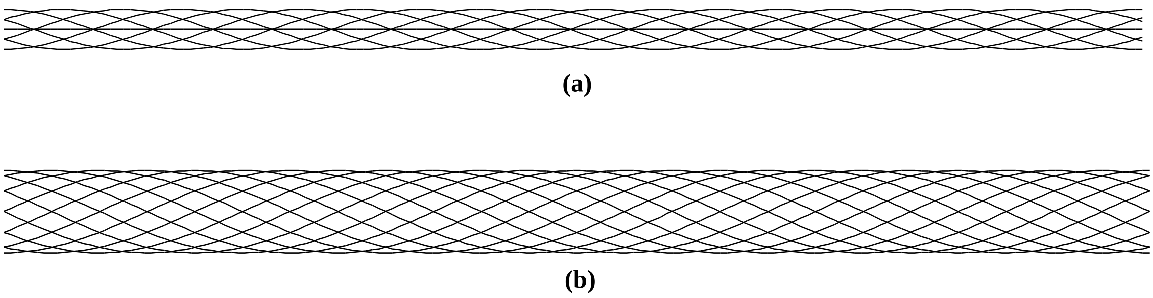

Fig. 5.2. Beam FE model of the two layer cable (a) Core and layer 1, (b) Layer 2

Table 5.1. Geometric and material properties of the two layer cable

Layer No.	No. of wires	Helical direction & angle [α]	Wire diameter [mm]	Pitch length [mm]	Model Length [mm]	Young's Modulus [GPa]	Poisson's ratio
Core	1	-	3.66	-	334.56	198	0.3
1	6	RHL, 75.37°	3.33	84.11	334.56	198	0.3
2	12	RHL, 75.9°	3.33	167.28	334.56	198	0.3

Fig. 5.3 shows the axial load-axial strain curves that were obtained through the use of the beam FE model, the experiments [3], and the analytical model [10]. During the investigation of the loads that correspond to the axial strain of 0.003, the observed response of the beam FE model is much closer than that of the analytical model to the experimental results. The differences from the experimental results are 20% and 5.7% for the analytical model and the beam FE model, respectively. Fig. 5.4 shows that the axial load-torque curves of the cable are also well predicted through the use of the beam FE model, whereby the cable produces a net torque of 140N-m at a working load of 120kN; that is, the torque in this cable is not balanced.

Regarding torque balance design, a consideration of the stress limit and the flexural rigidity, in addition to the torque balance, is also very important; that is, the design stress limit should always be satisfied. A lower flexural rigidity allows for a more effective cable handling capability; therefore, the torque balance condition and design stress limit should be satisfied together, and the flexural rigidity needs to be minimized.

In a two-layer cable, the helix angles α_1 and α_2 for layer 1 and layer 2, respectively, are the design parameters.

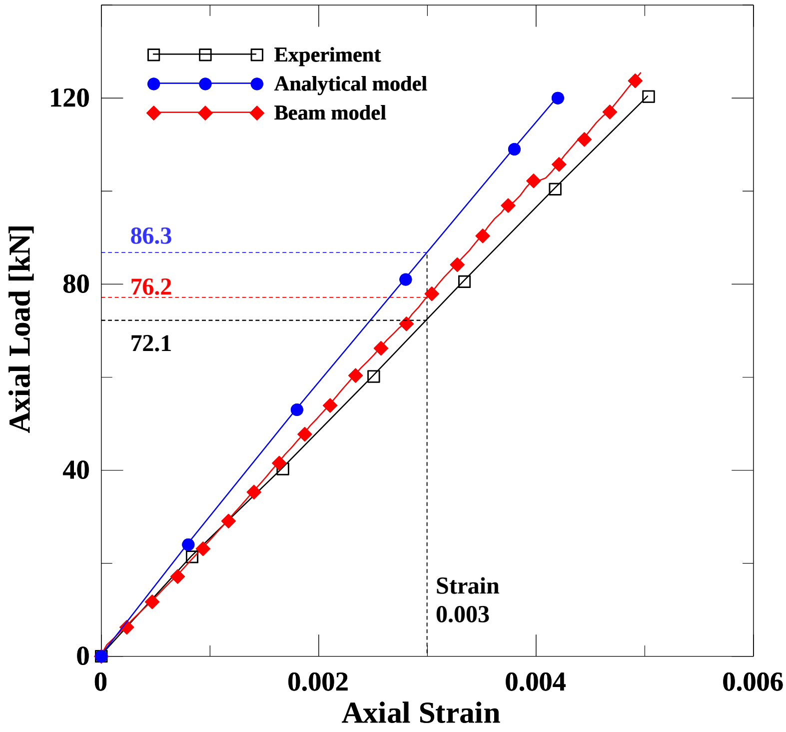

Fig. 5.3. Axial load-axial strain curves of the two layer cable

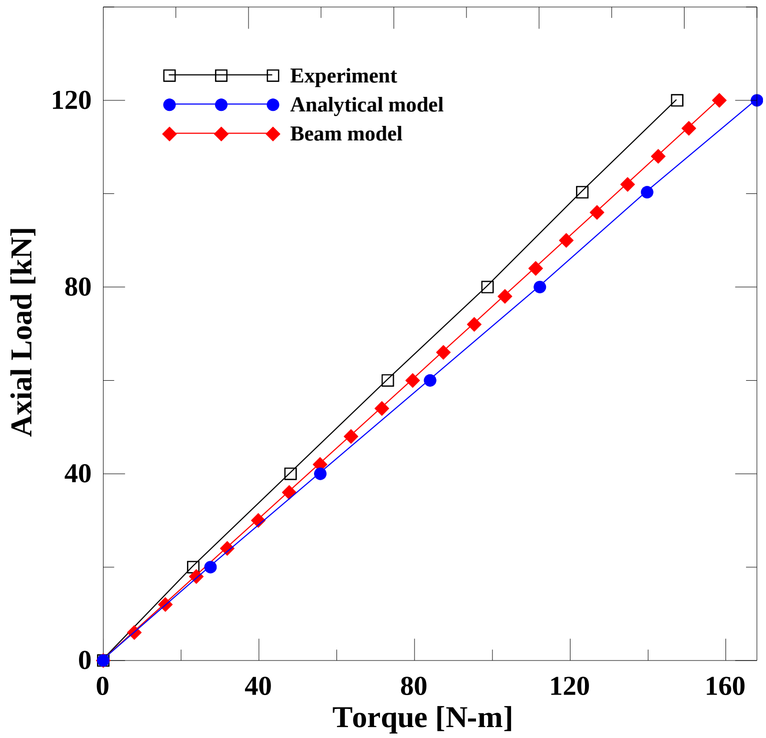

Fig. 5.4. Axial load-torque curves of the two layer cable

The torque balance design can be accomplished by using the following design procedure:

(Step 1) First, the helix angles are selected. Practically, a limit of the helical angle α_1 needs to be considered, because the wire has the maximum permissible value of the helical-wire area in the layer. The cross sections of the helical wires are perpendicular and are of an elliptical shape. The total surface area of these cross sections depends on the helical angle and the wire diameter of the layer. For a given wire diameter, the minimum helical angles are limited by the equations in Appendix C to make the closest fit between the helical wires and to maximize the surface area of the cross sections; therefore, the range of α_1 is approximately from 70° to 90°. Within this range, six α_1 values (72.5°, 75°, 77.5°, 80°, 82.5°, and 85° right-hand lay (RHL)) are selected for the torque balance design; similarly, in the range from 70° to 90°, five α_2 values (72.5°, 75°, 80°, 85°, and 90° left-hand lay (LHL)) are selected. Note that the angles α_1 and α_2 are in opposite directions.

(Step 2) For the selected α_2 and α_1 values, torque analyses are performed using the beam FE model. The α_2-torque relation curve for every α_1 value is then plotted to find the zero-torque points, as shown in Fig. 5.5. Using the six points, the torque balance curve (the relation between α_1 and α_2) is plotted, as shown in Fig. 5.9.

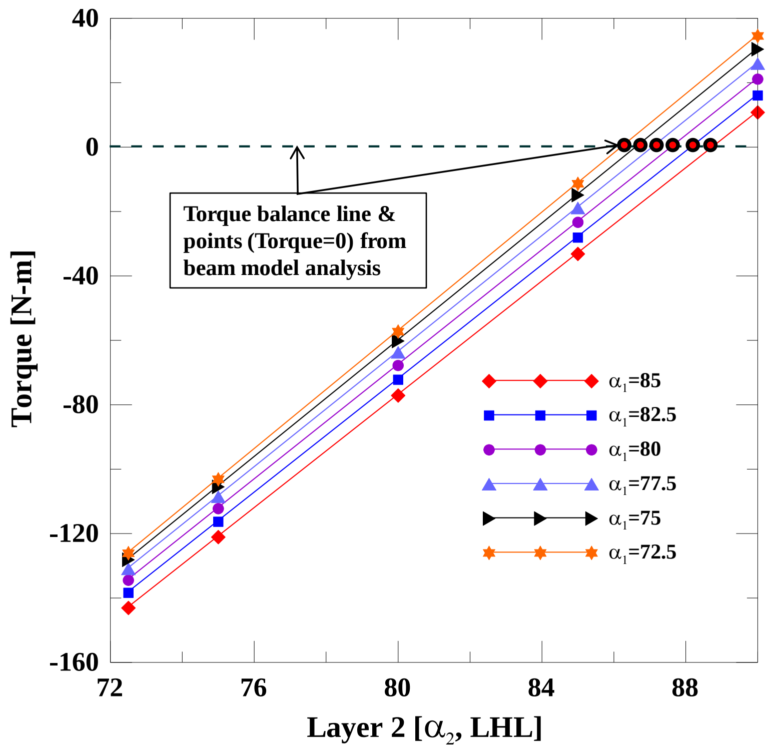

Fig. 5.5. Torque balance points (torque = 0); red dots: torque balance points

(Step 3) The maximum equivalent stress (Von-Mises stress) at the zero torque points is computed using the beam FE model and the equivalent-stress curve is also plotted, as shown in Fig. 5.9. Note that the maximum equivalent stress is generally found in the core because the core is subjected to both axial stress and transverse contact stress induced by the helical wires continuously pressing on the core.

(Step 4) Flexural rigidity is a very important factor when handling cable in cable industries, especially in the installation stage. To compute the flexural rigidity, bending analyses are performed using the beam model shown in Fig. 5. 6. Several tip moments with no pre-tension are applied at the right end of the cable; then, we can fit the centerline of the deformed cable with a circle fitting. The curvature of the bend radius ρ can be calculated through this analysis. The curves of the bending moment-curvature and flexural rigidity-curvature of the cable with different helical angle pairs (at zero torque points) are shown in Fig. 5.7 and 5.8. It is well known that, although the flexural rigidity and curvature relation is nonlinear, a smaller helical angle pair generally produces less flexural rigidity in the entire range of curvature [5, 55-56].

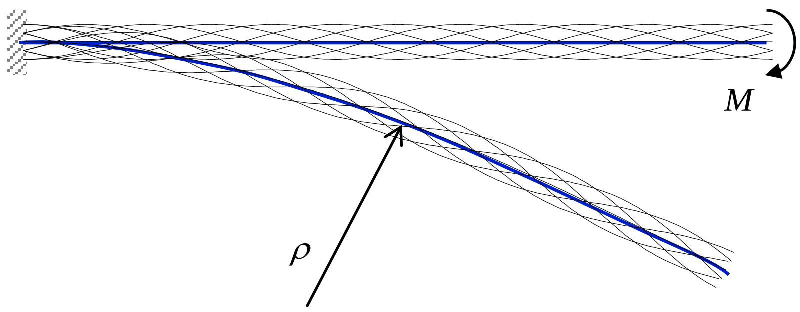

Fig. 5.6. Boundary conditions and deformation using beam model to compute flexural rigidity of the cable. M is tip bending moment and ρ is bend radius.

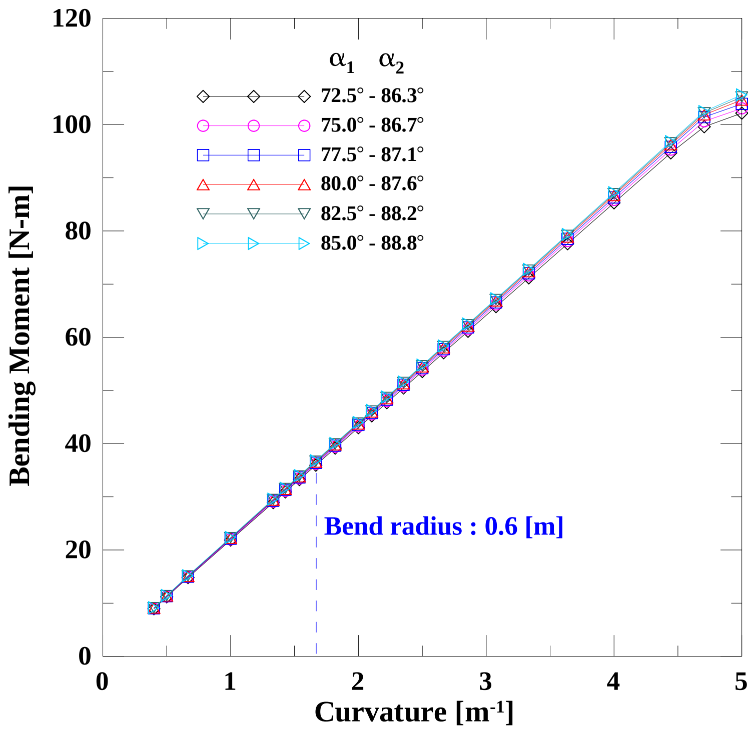

Fig. 5.7. Curves of the bending moment-curvature of the two layer cable with different helical angle pairs (at zero torque points).

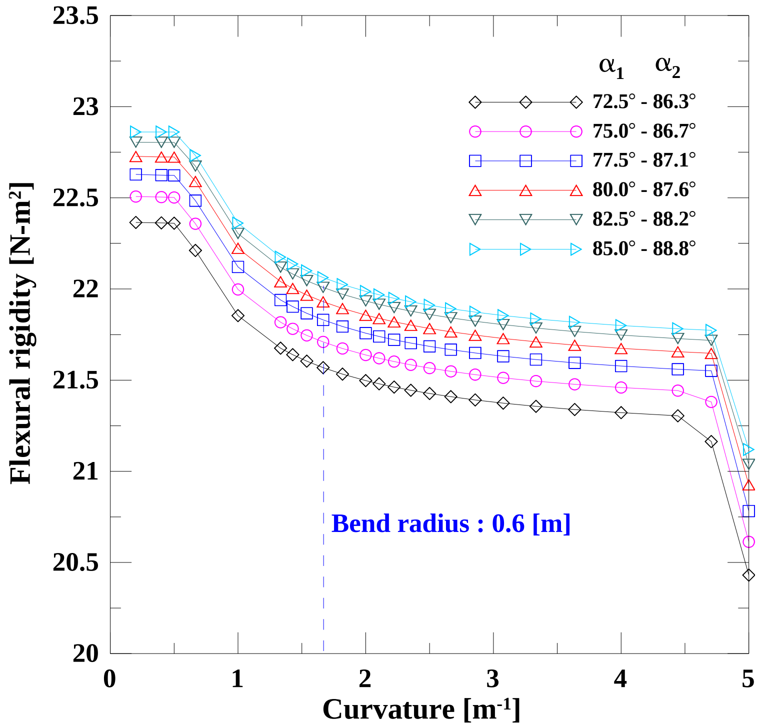

Fig. 5.8. Curves of the flexural rigidity-curvature of the two layer cable with different helical angle pairs (at zero torque points).

Based on these results, the flexural rigidity curve for the bend radius of 0.6m (cable drum size) is plotted at zero torque points, as shown in Fig. 5.9.

(Step 5) On the equivalent-stress curve, Point ① that corresponds to the design stress limit (924MPa), which is defined as 60 % of the yield strength (1540MPa) of the wire, is found. To satisfy the design stress limit, the value of α_1 should be larger than 78.85°, as shown in Fig. 5.9. In the range of α_1, the minimum flexural rigidity is obtained at α_1 = 78.85°, as shown in Point ② of Fig. 5.6. The torque balance point is finally determined at Point ③, whereby α_1 = 78.85° and α_2 = 87.41°, satisfying the design stress limit and minimizing the flexural rigidity.

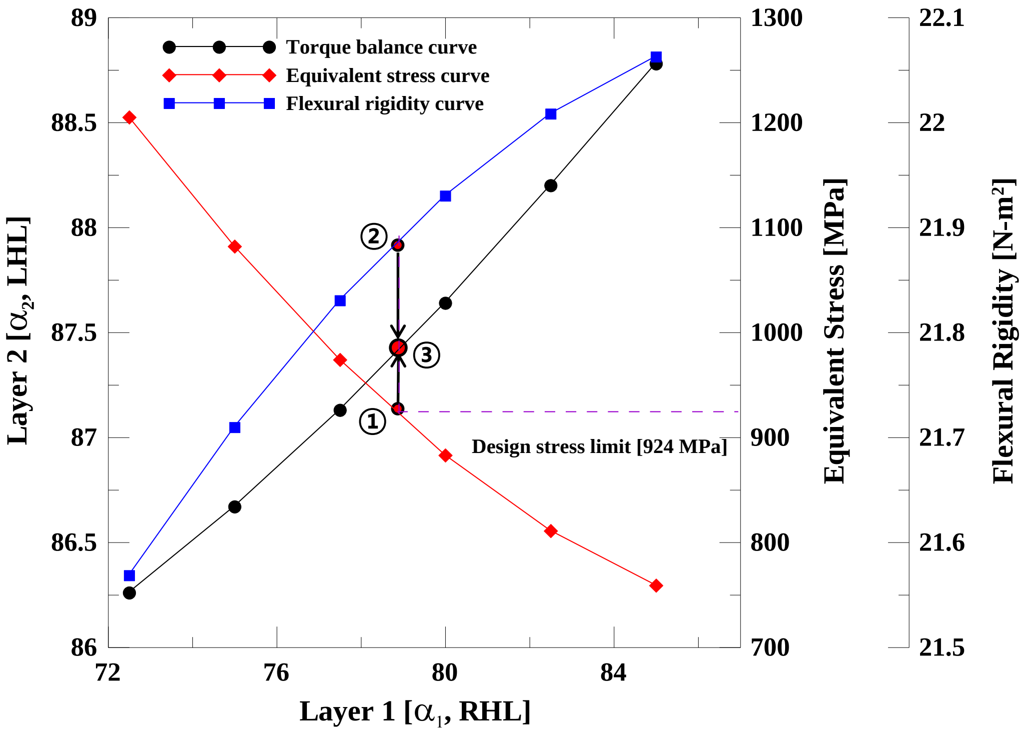

Fig. 5.9. Determination of the torque balance point ①: Design stress limit point, ②: Minimum flexural rigidity point that satisfies the design stress limit, ③: Torque balance point that satisfies the design-stress limit and minimizes the flexural rigidity.

This proposed design procedure for which the beam FE model is used is practically very useful for the torque balance design of helically-stranded cables. Fig. 5.10 summarizes the flowchart of the design procedure.

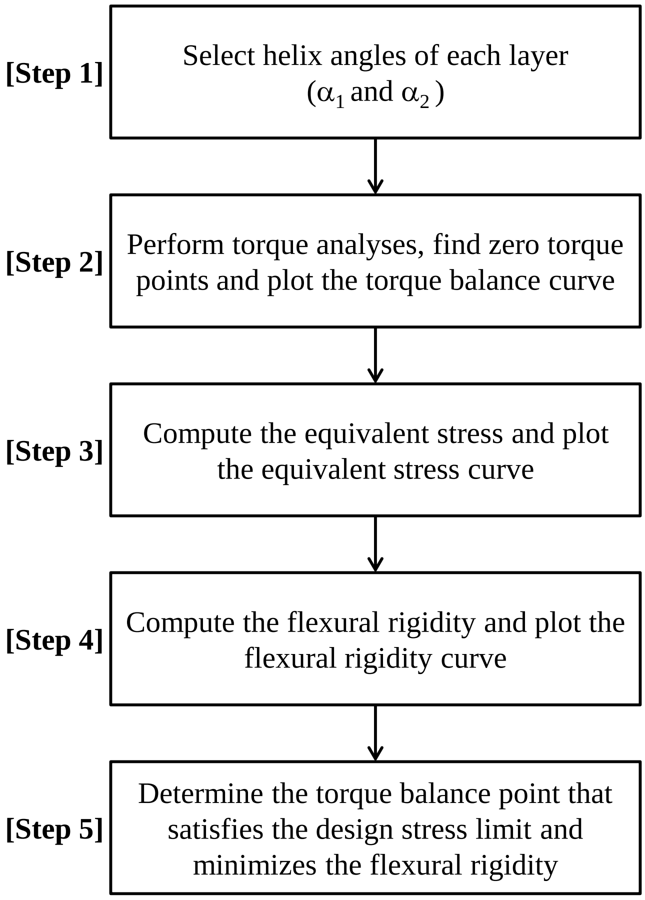

Fig. 5.10. Torque balance design procedure.

5.1.1 Comparison with analytical models

In this section, we compared FE beam model with analytical model for the torque balance. In the analytical model, the equation $\delta\theta / h = 0$ and $M_T = 0$ in Eq. (1) and thus $K_{\theta\varepsilon} = 0$. This means

$$(K_{\theta\varepsilon})_{layer1} + (K_{\theta\varepsilon})_{layer2} = 0 \tag{73}$$

Using Eq. (73) and Eqs. (25b), (26c) and (27c) for various analytical models, the torque balance points were calculated and compared with the results of beam FE model. A two layer contra helically armored KEVLAR EM cable used as a segment link between a surface support ship and a deep sea unmanned work system has been used. For the two layered cable given in Table 5.2, suitable helix angle for the outer layer α_2 is computed for different helix angles of inner layer α_1. MATLAB program was used for calculation and the convergence condition for satisfying Eq. (73) is as follows

$$\left| \frac{(K_{\theta\varepsilon})_{layer1} - (K_{\theta\varepsilon})_{layer2}}{(K_{\theta\varepsilon})_{layer1}} \right| \le 10^{-5} \tag{74}$$

Table 5.2. Geometric and material properties of KEVLER EM cable

Parameter	Inner Layer	Outer Layer
Wire radius, r_w [mm]	1.285	0.9715
Centerline radius, r [mm]	12.59	14.85
Helix angle, α [deg]	RHL	LHL
Young's Modulus, E [GPa]	75.36	83.74
Yield Strength, S_y [MPa]	1309	1509
Number of wires, n	28	44
Core radius, r_c [mm]	11.31	

The relationship between α_1 and α_2 obtained and compared with FE beam model is shown in Fig. 5.11. The results among analytical models are similar, but they are different from beam FE model. Especially, in the smaller helical angle, the difference is larger.

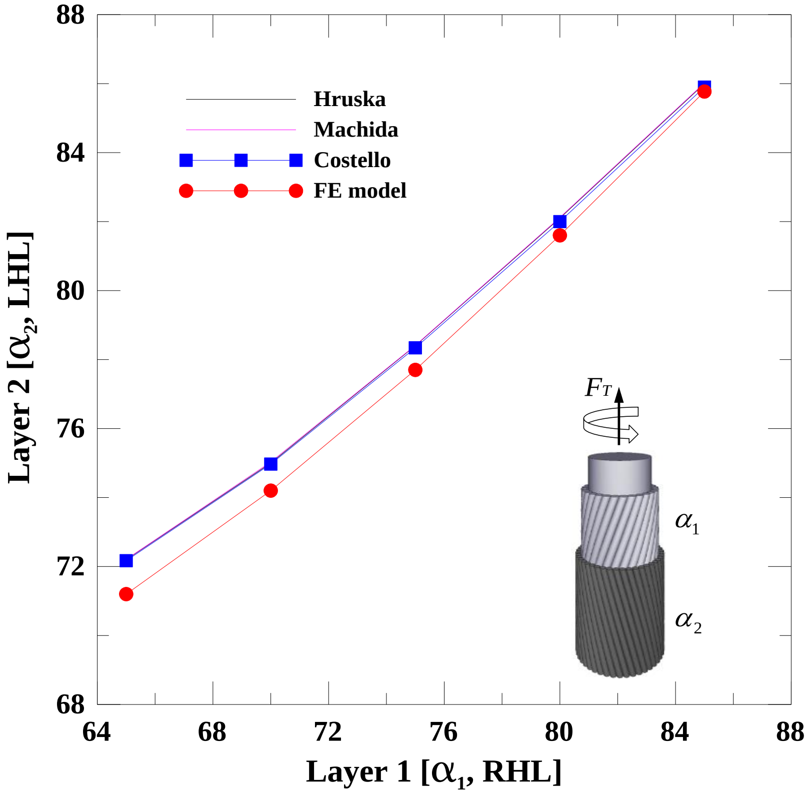

Fig. 5.11. Comparison of helix angles satisfied with torque balance of KEVLER EM cable

5.2 Three layer cable

We performed the torque balance design of a three layer cable with 37 wires (1 + 6 + 12 + 18), and its geometry and boundary conditions are shown in Fig. 5.12. Coulomb friction model with a friction coefficient of 0.115 was used in this model. Fig. 5.13 shows the beam FE model that is used, and the geometric and material properties are given in Table 5.3. To achieve the torque balance for the three-layer cable, the sum of the torques that are induced in the three layers should be equal to zero, as follows:

$$(K_{\theta\varepsilon})_{layer\ 1} + (K_{\theta\varepsilon})_{layer\ 2} + (K_{\theta\varepsilon})_{layer\ 3} = 0 \tag{75}$$

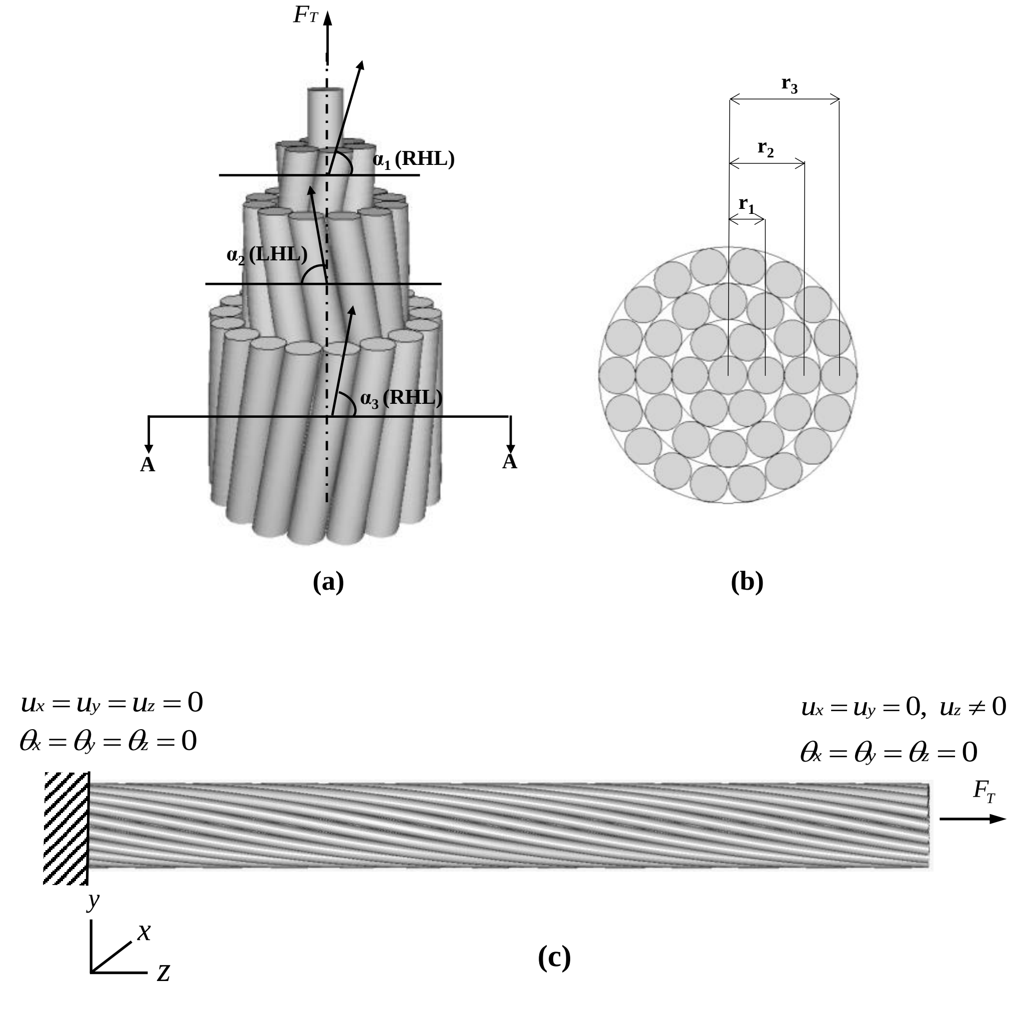

Fig. 5.12. Geometry of the three layer cable (1 + 6 + 12 + 18 structure). α_1: helix angle of layer 1; α_2: helix angle of layer 2; α_3: helix angle of layer 3.

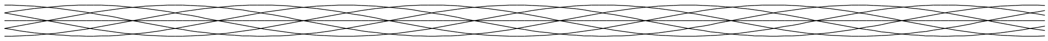

(a)

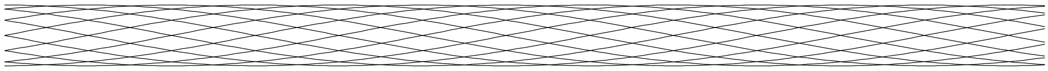

(b)

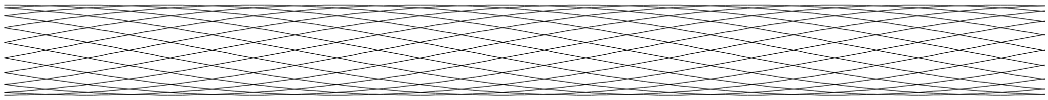

(c)

Fig. 5.13. Beam FE model of the three layer cable (a) Core and layer 1, (b) Layer 2, (c) Layer 3

Table 5.3. Geometric and material properties of the three-layer cable where RHL and LHL denote “right hand lay” and “left-hand lay,” respectively.

Layer No.	No. of wires	Helical direction and angle [α]	Wire diameter [mm]	Pitch length [mm]	Young’s Modulus [GPa]	Poisson’s ratio
Core	1	-	1.09	-	190	0.3
1	6	RHL, 79.23°	1.00	34.52	190	0.3
2	12	LHL, 79.23°	1.00	67.55	190	0.3
3	18	RHL, 79.23°	1.00	100.58	190	0.3

Fig. 5.14 shows the axial load-axial strain curves that were obtained with the use of the beam FE model, the experiments, and the analytical model. The beam FE model is capable of a sound prediction of the experimental results [31].

By using a design procedure that is similar to that which has been presented for the two layer cable, the torque balance points that satisfy the design stress limit and minimize the flexural rigidity can be determined for the three layer cable model.

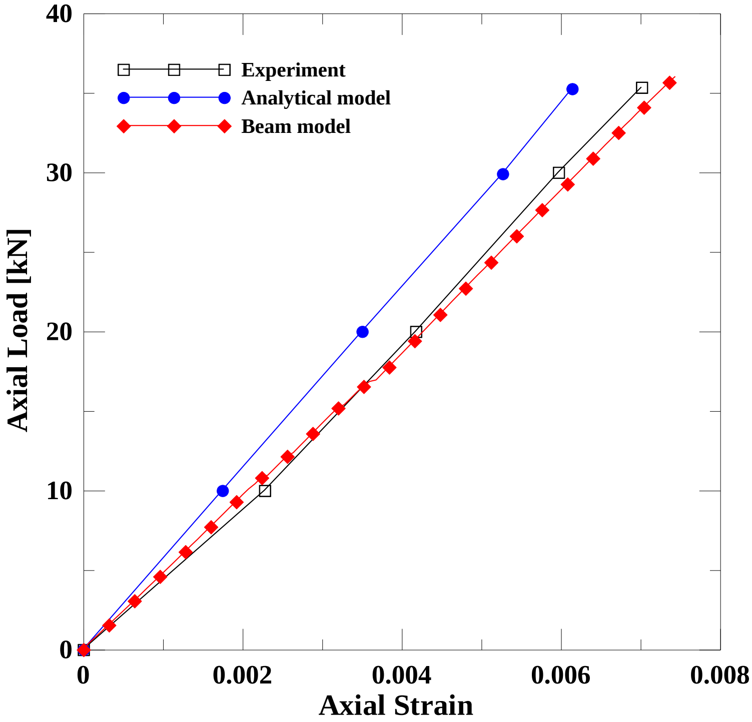

Fig. 5.14. Axial load-axial strain curves of the three layer cable

First, six α_1 values (72.5°, 75°, 77.5°, 80°, 82.5°, and 85° RHL), six α_2 values (72.5°, 75°, 77.5°, 80°, 82.5°, and 85° LHL), and five α_3 values (72.5°, 75°, 80°, 85°, and 90° RHL) are selected for the torque balance design. The directions of the three helix angles are defined in Fig. 5.12 (a).

For the selected α_1, α_2 and α_3 values, 180 cases (six $\alpha_1 \times$ six $\alpha_2 \times$ five α_3) of the torque analyses were performed using the beam FE model. The α_3 torque-relation curves are plotted for all of the α_1 and α_2 values and the zero-torque points were found. Fig. 5.15 shows the α_3 - torque relation curves for the α_2 values when α_1 = 85°; similarly, for the other α_1 values (72.5°, 75°, 77.5°, 80°, and 82.5°), the curves are plotted and the torque balance points were found. . Fig. 5.16 and 5.17 show the curves of the bending moment-curvature and the flexural rigidity-curvature for the three layer cable with different helix angle pairs (at zero torque points) when α_1 =85°. It also shows that a smaller helix angle pair produces less flexural rigidity over the entire range of curvature.

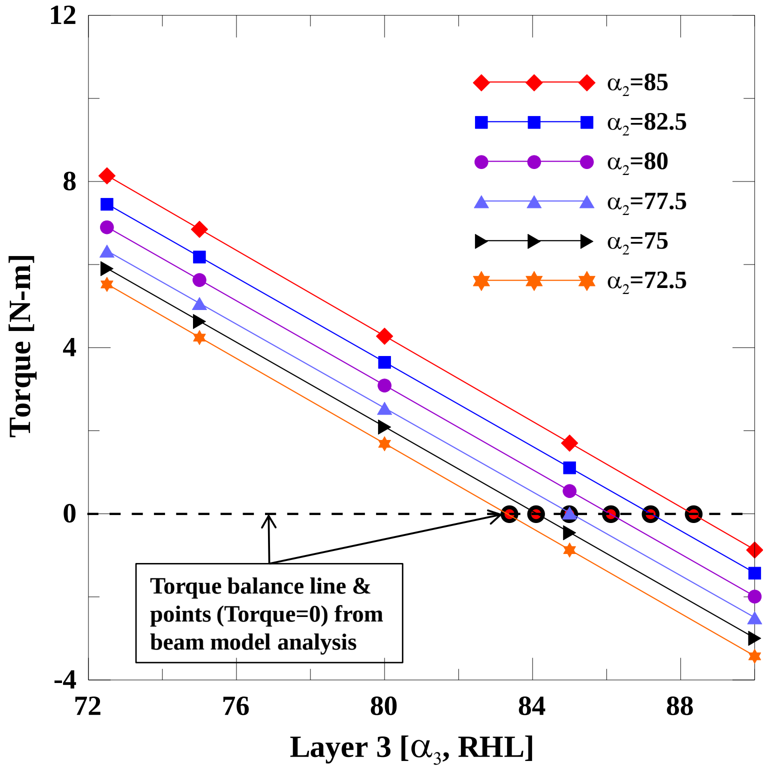

Fig. 5.15. Torque balance line and points (torque = 0) when $\alpha_1 = 85°$; red dots: torque balance points.

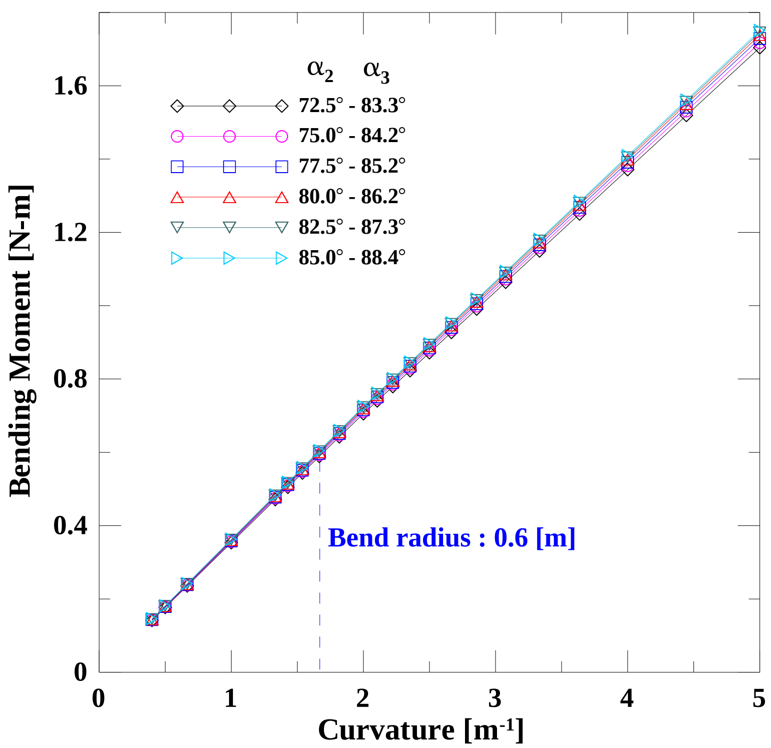

Fig. 5.16. Curves of the bending moment - curvature of the three layer cable with different helical angle pairs (at zero torque points) when $\alpha_1 = 85°$.

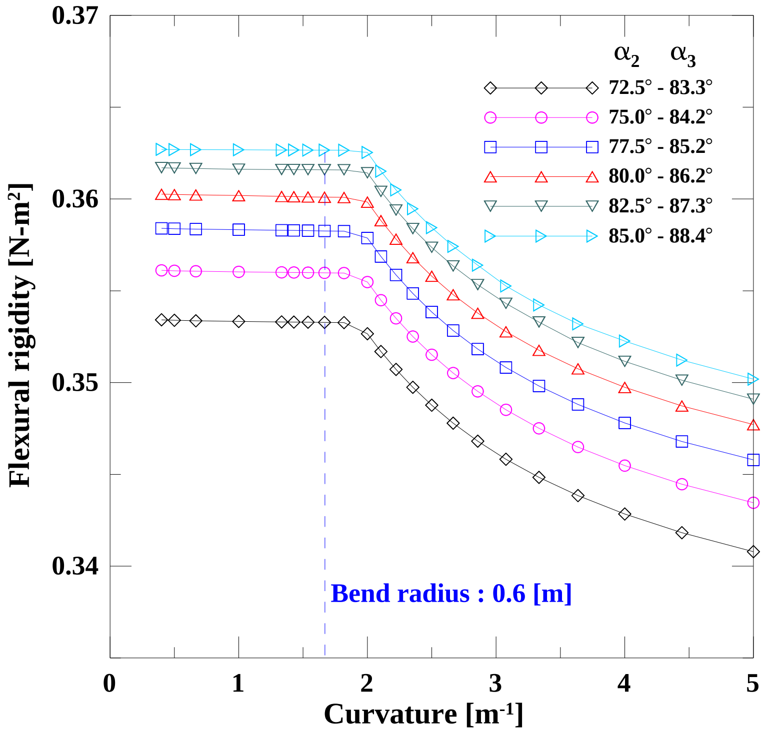

Fig. 5.17. Curves of the flexural rigidity - curvature of the three layer cable with different helical angle pairs (at zero torque points) when α_1 = 85°.

Using the obtained torque balance points, the torque balance curves (the relations among α_1, α_2 and α_3) are plotted, as shown in Fig. 5.18. On the equivalent stress curves that are also plotted, the design-stress limit (924MPa) can be reached for three α_1 values (80°, 82.5° and 85°), and the corresponding points in the torque balance curves are point ①, point ②, and point ③. The flexural rigidity obtained at the three points, ①, ②, and ③, are 0.3602 N-m^2, 0.3607 N-m^2, and 0.3612 N-m^2, respectively, and point ① provides the minimum flexural rigidity among the three points. The torque balance design is finalized at α_1 = 85°, α_2 = 80.1° and α_3 = 86.28°.

Based on the design procedure proposed in this study, multilayered helically-stranded cables that comprise four or more layers can be practically designed for torque balance.

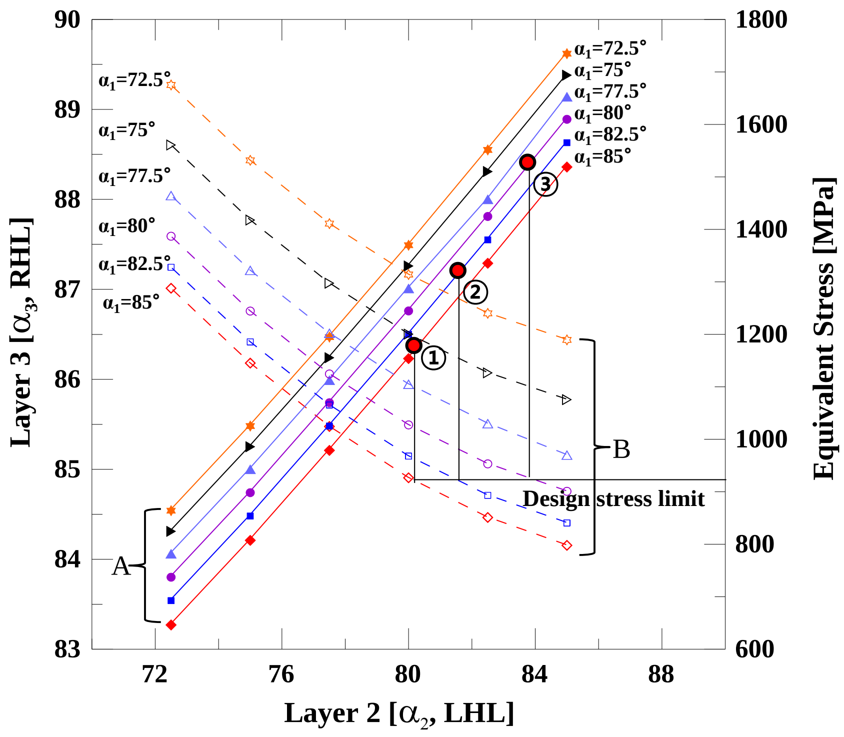

Fig. 5.18. Determination of the torque balance point; A: torque balance curves; B: equivalent stress curves; red dots: torque balance points that satisfy the design stress limit.

Finally, we note that in engineering practice, two and three layer cables have been most widely used and the proposed design procedure is demonstrated for such cases. However, as the number of cable layers increases, the design procedure could become very complicated. Refs. [57-58] suggest a torque balanced arrangement of high axial stiffness for the cable design, using an analytical model derived from parametric study and the structural optimization method, for up to five layers. This may be a good solution for the design of multilayer cables, and the beam FE model proposed in this paper could be used as an analysis tool for it.

Here, for more practical approach to perform the torque balance design of multilayer cables, it may be a better method to determine only two helical angles, α_{n-1} and α_n, for n layer cables using the beam FE model. For an example, in a five layer cable, the helical angles of the first, second and third layers (with alternating opposite directions) could be determined within a practically reasonable range, and then α_4 and α_5 could be determined using the torque balance design procedure suggested (as presented in Fig. 5.10). It is not a perfect solution for the design of multilayer cables, but it may be a good practical solution useful in cable industries.

6. Case study

To verify the accuracy of the design procedure for torque balance, two test cables, typical of aluminum-conductor steel reinforced (ACSR) and submarine power cable, were constructed and subjected to tests.

6.1 Case study 1: Torque balance design of ACSR cable

The ACSR test cable is depicted in Fig. 6.1. Its outside diameter is 22.75mm and the external 2 layers are made of aluminum alloy wires whose function is mainly to flow electrical current. Core and the internal 1 layer are made of aluminum-clad steel wires that act as the main structural part. Geometric and material properties for all cable components are summarized in Table 6.1.

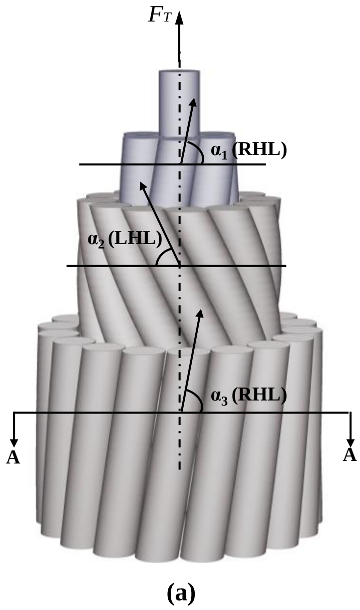

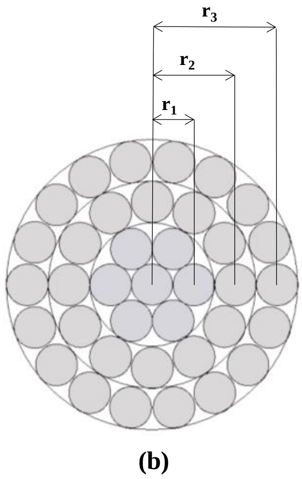

Fig. 6.1. Geometry of ACSR cable. Core and 1 layer : aluminum-clad steel, 2 and 3 layers : aluminum alloy.

Table 6.1. Geometric and material properties of ACSR cable

Layer No.	No. of wires	Helical direction and angle [α]	Wire diameter [mm]	Pitch length [mm]	Young's Modulus [GPa]	Poisson's ratio
Core	1	-	3.25	-	162	0.3
1	6	RHL, 85°	3.25	233.4	162	0.3
2	12	LHL, 75.5°	3.25	157.9	69	0.33
3	18	RHL, 85.4°	3.25	761.4	69	0.33

6.1.1 Cable design

By using the proposed design procedure in this paper, six α_2 values (72.5°, 75°, 77.5°, 80°, 82.5°, and 85° left-hand lay (LHL)) and five α_3 values (72.5°, 75°, 80°, 85°, and 90° RHL) are selected for the torque balance design, and α_1 is fixed as 85°(RHL).

For the selected α_2 and α_3 values, 30 cases (one $\alpha_1 \times$ six $\alpha_2 \times$ five α_3) of the torque analyses were performed using the beam FE model. The α_3 torque-relation curves are plotted for all of α_2 values and the zero-torque points were found. Fig. 6.2 shows the α_3 - torque relation curves for all of α_2 values, the curves are plotted and the torque balance points were found. Coulomb friction model was used with a friction coefficient of 0.2 in FE analysis.

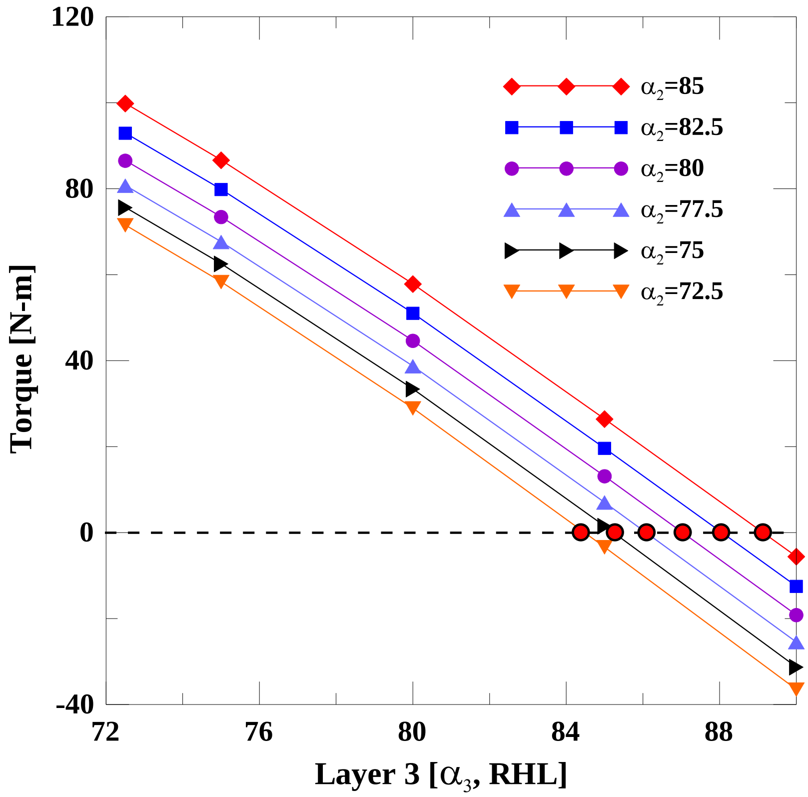

Fig. 6.2. Torque balance points of ACSR cable

Using the obtained torque balance points, the torque balance curves are plotted, as shown in Fig. 6.3. The equivalent stress curves and flexural rigidity curves are also plotted. On the equivalent-stress curve, Point ① that corresponds to the design stress limit (720MPa), to satisfy the design stress limit, the value of α_2 should be larger than 75.5°, as shown in Fig. 6.3. In the range of α_2, the minimum flexural rigidity is obtained at $\alpha_2 =$

75.5°, as shown in Point ② of Fig. 6.3. The torque balance point is finally determined at Point ③, whereby α_2 = 75.5° (LHL) and α_3 = 85.4°(RHL), satisfying the design stress limit and minimizing the flexural rigidity.

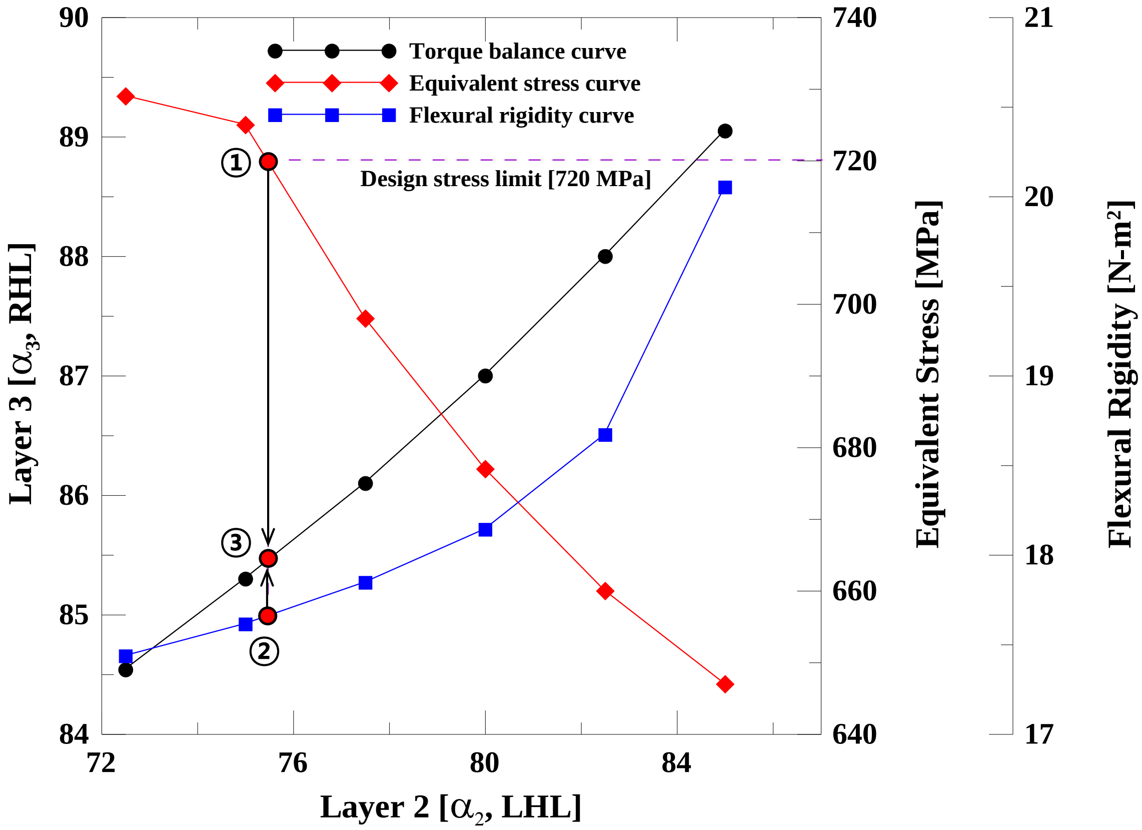

Fig. 6.3. Determination of the torque balance point of ACSR cable

6.1.2 Experimental test

First, the mechanical tests of core and the internal 1 layer, which are made of aluminum-clad steel wires, were performed as shown in Fig. 6.4. Both ends were firmly socketed and fixed against rotation. One end was attached to a torque meter.

Fig. 6.4. Tensile test of the core and internal 1 layer structure (aluminum-clad steel wires) of ACSR cable

Comparison of the beam model and test results is given in Figs. 6.5 and 6.6, which are axial load-axial strain curves and axial load-torque curves respectively. The beam model is successful in predicting the reaction torque as well as the load-strain relation with applied tension. It is obvious that the beam model predicts the behavior of the core and internal 1 layer structure.

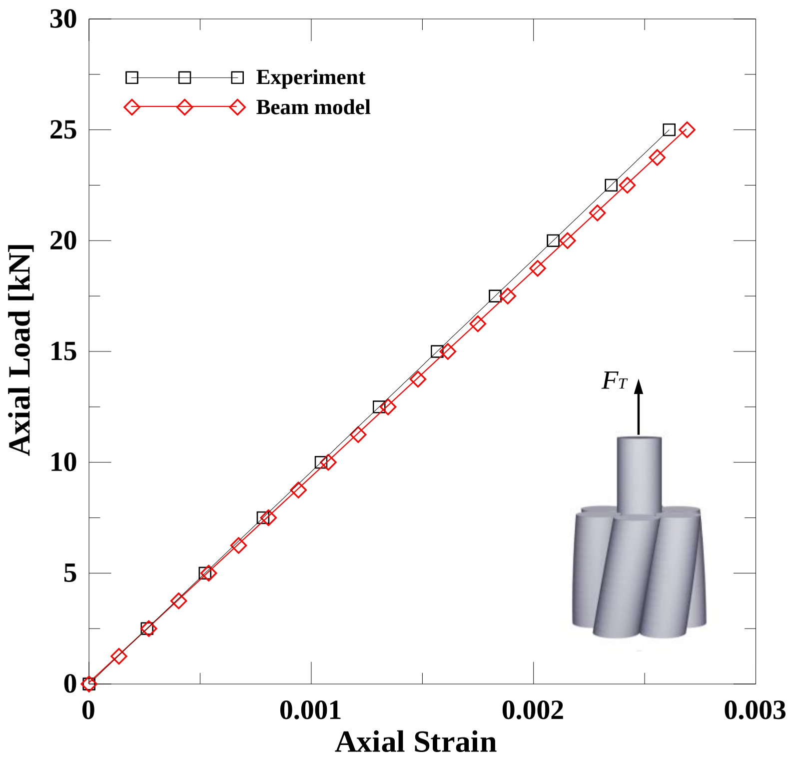

Fig. 6.5. Axial load-axial strain curves of the core and 1 layer structure of ACSR cable

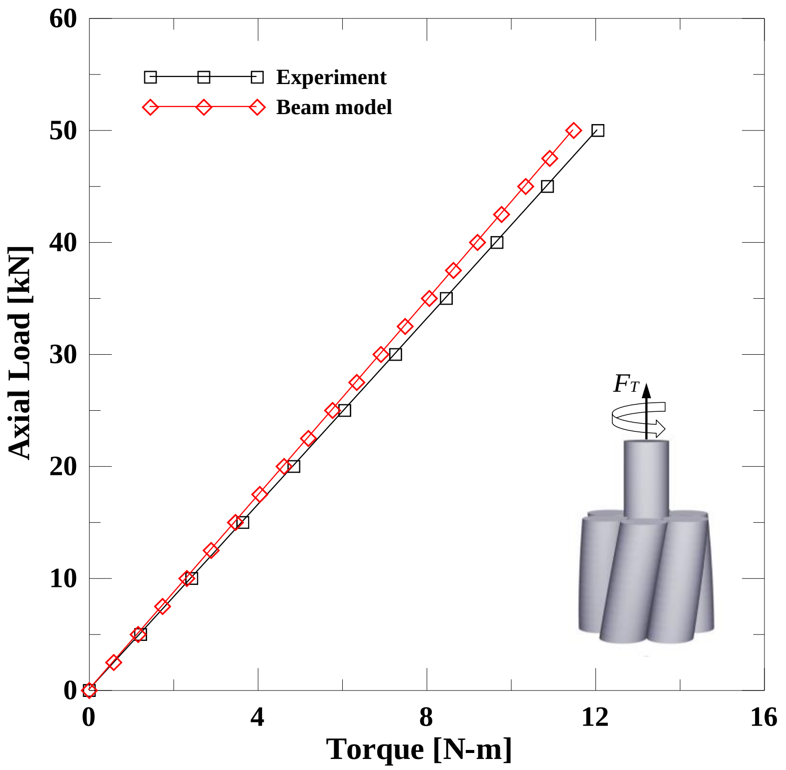

Fig. 6.6. Axial load-torque curves of the core and 1 layer structure of ACSR cable

Second, the mechanical tests were performed on the ACSR cable which is manufactured by torque balance design in section 6.1.1. The specimen was socketed and restrained against rotation at each end. The load was applied up to 100kN. During the test, cable axial strain and reaction torque resulting from an applied tension were measured.

6.1.3 Results and discussion

Figs. 6.7 and 6.8 compare beam model and experimental results respectively. Fig. 6.7 shows close agreement in the axial load-axial strain plots, while Fig. 6.8 shows a small difference. The torque from beam FE model is 0.56 N-m with applied tension 100kN. The torque value from beam model is nearly “zero” and this means the cable is well designed for torque balance. The experimental result indicates that the torque is 2.53N-m with applied tension, the difference of the value between beam model and experiment is 1.97N-m. It can be considered that the difference is due to unequal load sharing among the wires. Looseness of the wires while handling them in preparation for socketing makes it possible for wire layers to have unequal lengths between sockets and generate torque. Nevertheless, the torque value from experiment is below 3N-m and it’s so small value. It’s obvious that this small torque value doesn’t make the cable to have any harmful mechanical behavior.

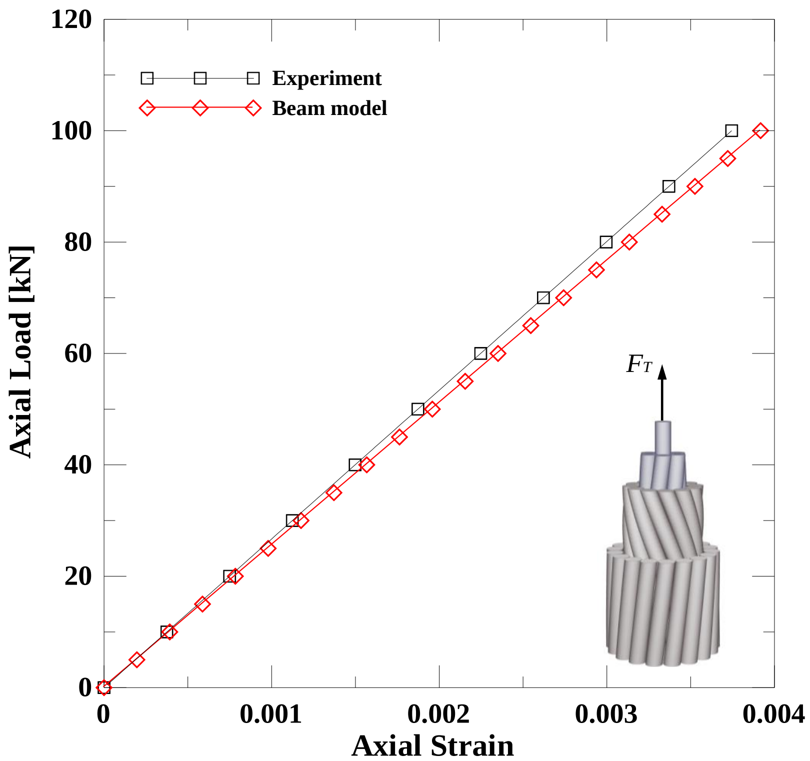

Fig. 6.7. Axial load-axial strain curves of ACSR cable

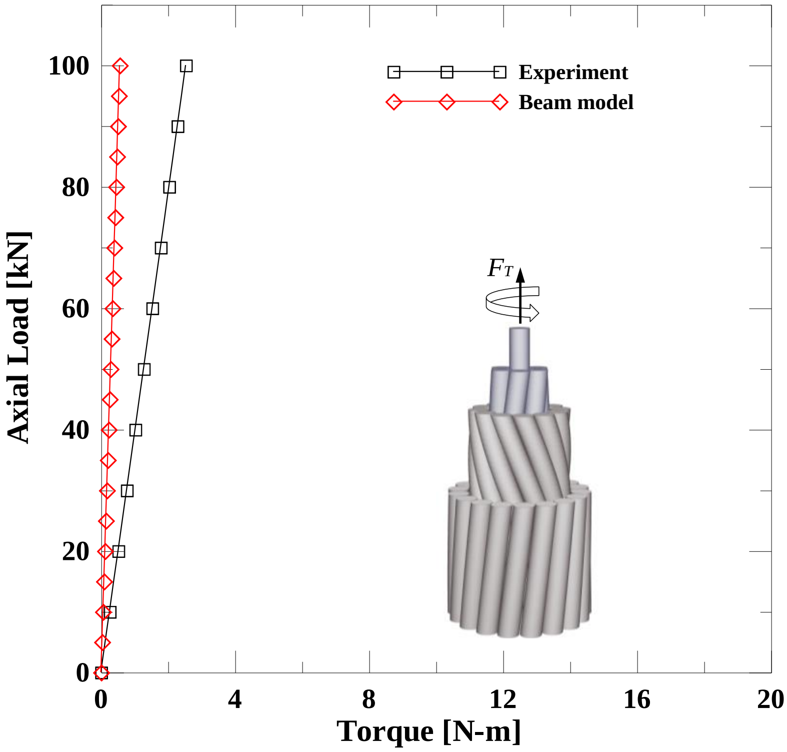

Fig. 6.8. Axial load-torque curves of ACSR cable

As a result, good agreement between test and analysis results indicates that satisfactory estimates of cable behavior can be obtained with the proposed beam FE model and torque balance design procedure. This can provide preliminary designs and guidance in planning appropriate cable manufacturing.

6.2 Case study 2: Torque balance design of submarine power cable

The submarine power cable is depicted in Fig. 6.9. The cable mainly consists of copper keystone conductors, XLPE insulation, a lead sheath and double layers of copper armor wires. Conductors consist of helically stranded flat wires. Geometric and material properties for all cable components are summarized in Table 6.2.

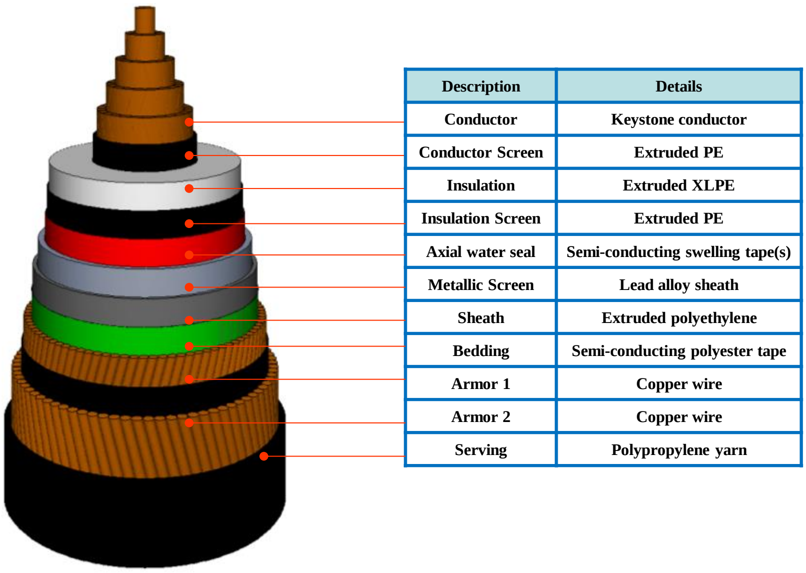

Fig. 6.9. Geometry of submarine power cable.

Table 6.2. Main geometric and material properties of submarine cable

Layer	No. of wires	Helical direction and angle [α]	Outer Diameter [mm]	Pitch length [mm]	Young's Modulus [GPa]	Poisson's ratio
Conductor	-	-	58.8	-	117	0.36
Insulation	-	-	117.2	-	0.30	0.46
Metallic screen	-	-	130.6	-	9.78	0.45
Sheath	-	-	137.0	-	0.88	0.46
Armor 1	85	RHL, 74.7°	148.52 (5mm : wire)	1650	117	0.36
Armor 2	78	LHL, 75.5°	162.72 (6mm : wire)	1900	117	0.36

6.2.1 Cable core test and modified cable model

The real model consists of many components as shown in Fig. 6.9. This model needs to be simplified for the torque balance design using beam model. We assumed the equivalent core that has only one component from conductor to bedding layer. Fig. 6.10 shows the modified model using equivalent core. The modified model consists of equivalent core and wires. Fig. 6.11 shows the beam FE model that is used in this modeling.

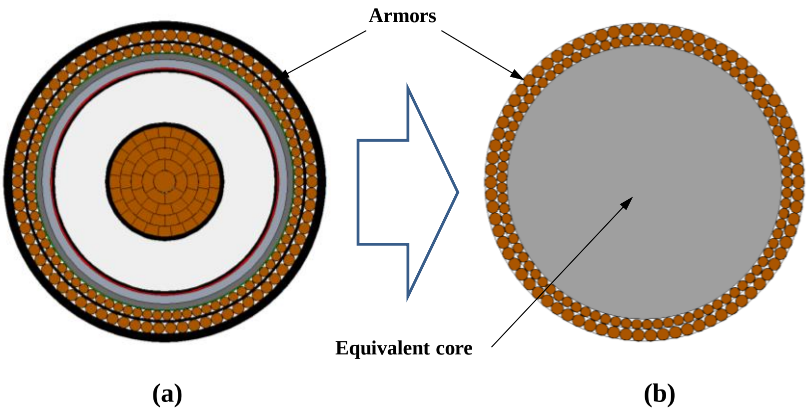

Fig. 6.10. Modified model using the equivalent core. (a) original model, (b) modified model.

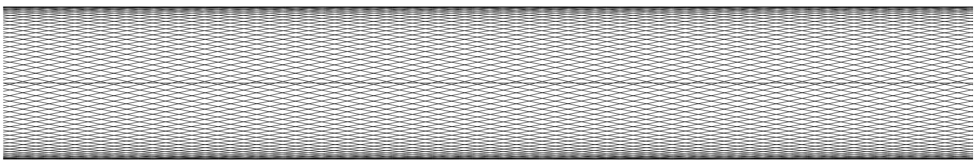

(a)

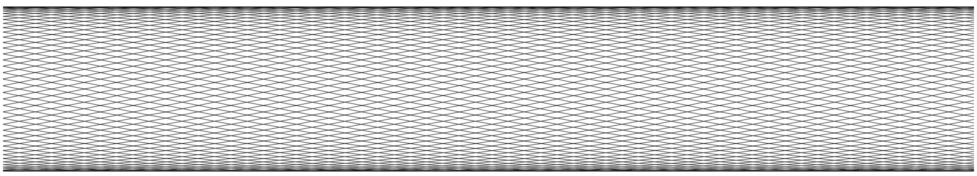

(b)

.

Fig. 6.12. Beam FE model of submarine cable (a) Equivalent core and layer 1, (b) Layer 2

The cable core test was performed to get the equivalent material properties for the equivalent core. The test equipment is shown in Fig. 6.12. The core was socketed and restrained against rotation at each end. The load was applied up to 200kN. During the test, cable axial strain and reaction torque resulting from an applied tension were measured.

The test result is given in Figs. 6.13 and 6.14, which are axial load-axial strain curves and axial load-torque curves respectively. The equivalent Young’s modulus of the core can be determined as 19.84GPa from the axial load-axial strain curve. Because the conductor of the cable originally consists of helically stranded flat wires, the torque of the core is generated under axial load. The torque from the core test is 281N-m when the load applied 200kN as shown in Fig. 6.14. It is very important to consider the torque of the core from the test when we design the torque balance using the modified model. After the torque balance design using the modified model, the torque of the core from the test needs to be added or subtracted depending on its direction of the torque.

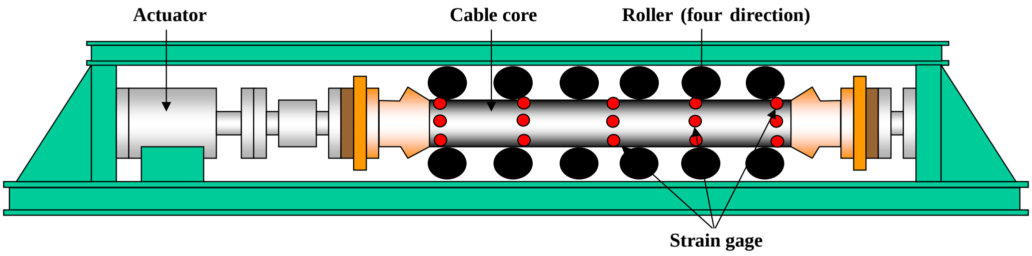

Fig. 6.12. Tensile test equipment of cable core

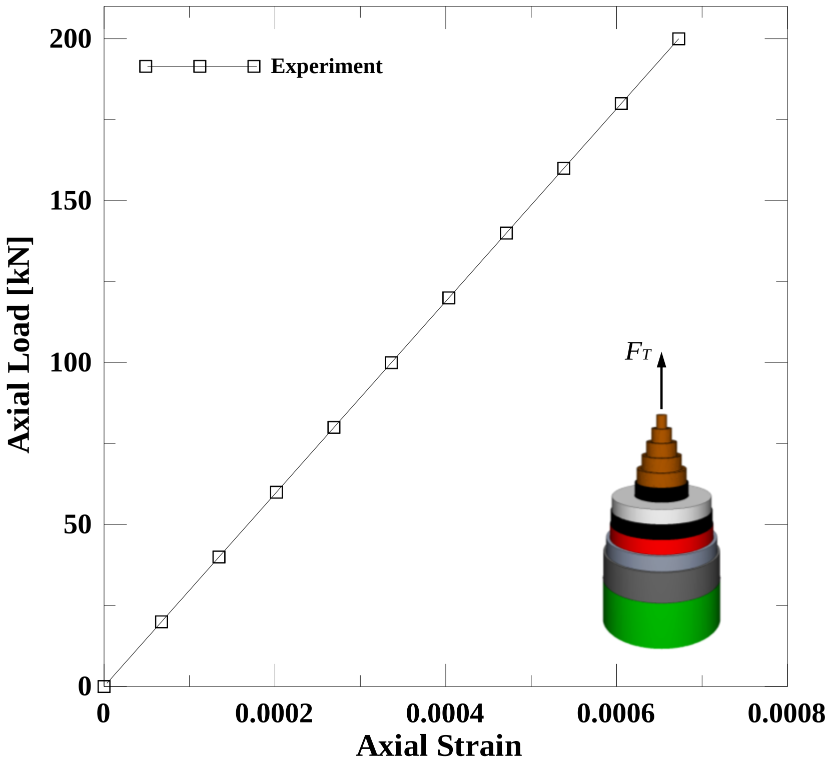

Fig. 6.13. Axial load-axial strain curves of cable core

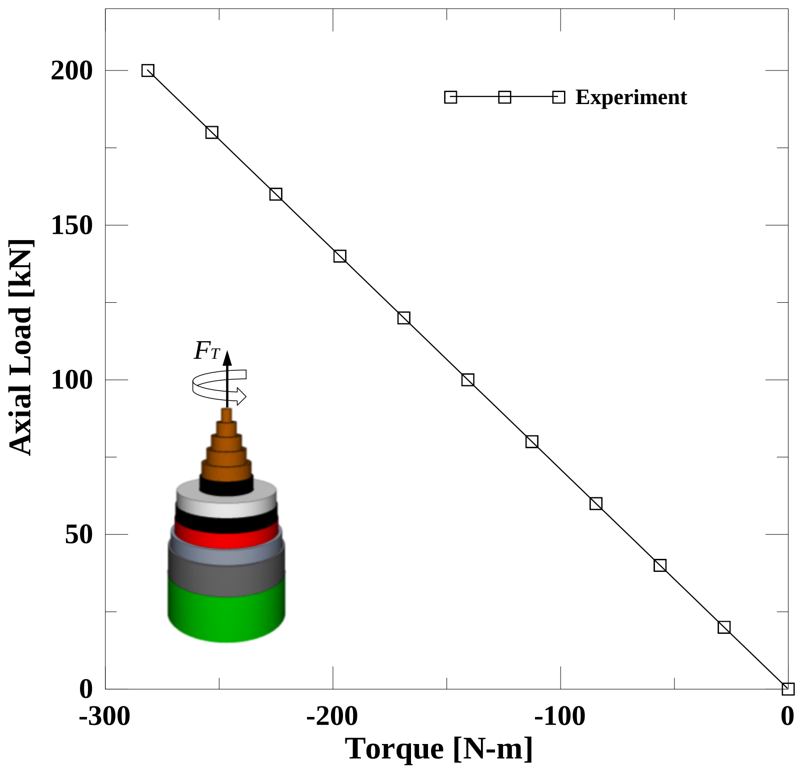

Fig. 6.14. Axial load-torque curves of cable core

Bending test was performed to find bending rigidity and Young' modulus for bending of the equivalent core was calculated. Fig. 6.15 shows the test equipment for 3 point bending. Bending rigidity can be calculated following equation.

$$EI = \frac{WL^3}{48\delta}, \tag{76}$$

where EI is bending rigidity, W is load, L is length between pivots and δ is deformation.

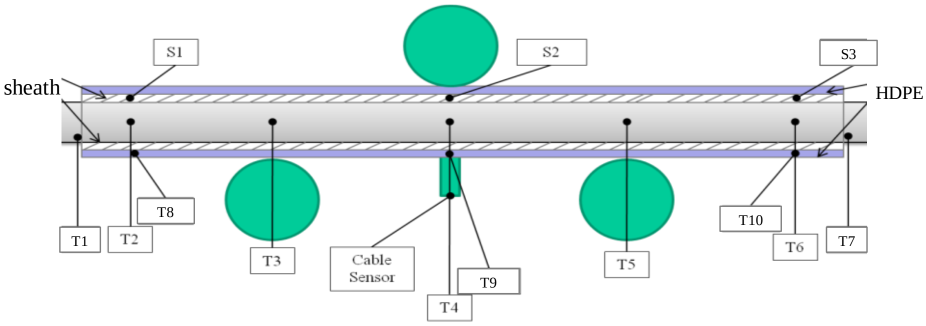

Fig. 6.15. Bending test equipment of the cable core

The equivalent Poisson's ratio needs to be determined but it's not easy to measure the lateral displacement of the core from the test. Therefore, the FE analysis for finding equivalent Poisson's ratio was performed using beam model. The difference of the values of Axial load-axial strain curves was just below 0.1% with the range of the Poisson's ratio 0.1~0.45 from FE analysis result as shown in Fig. 6.16. Thus, the Poisson's ratio was determined as 0.4 and Table 6.3 shows the geometric and material properties of the modified model for the submarine cable.

In the table 6.3, there are two types of Young' modulus, one is for axial rigidity and another is for bending rigidity, respectively.

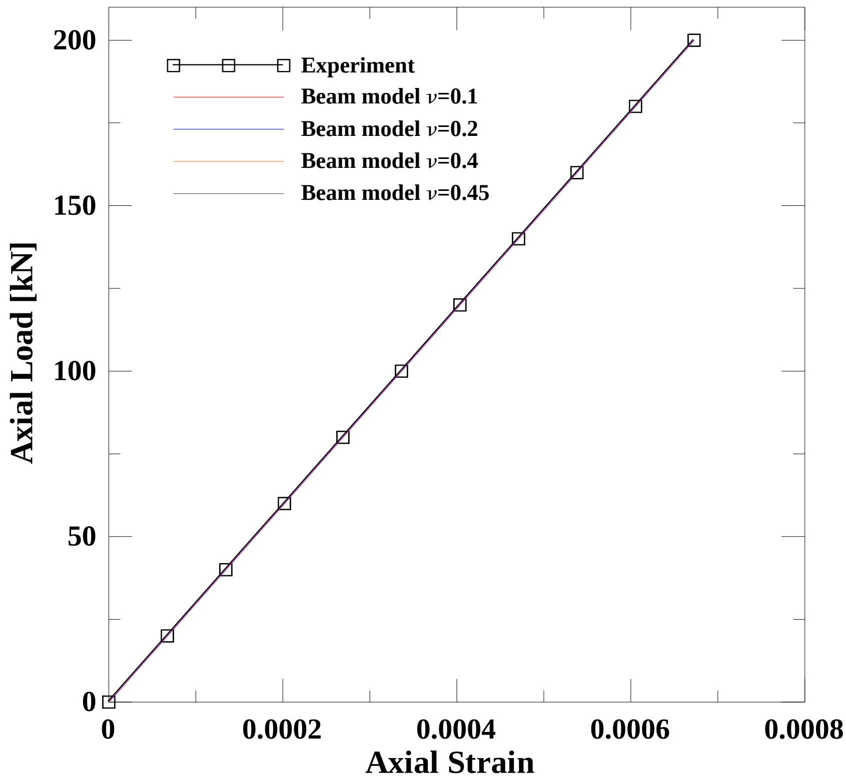

Fig. 6.16. Axial load-axial strain curves of cable core with Poisson's ratio

Table 6.3. Geometric and material properties of the modified model for the torque balance of the submarine cable

Layer	No. of wires	Helical direction and angle [α]	Wire diameter [mm]	Pitch length [mm]	Young's Modulus * [GPa]	Poisson's ratio
Equivalent core	-	-	138.12	-	19.84 (A) 2.36 (B)	0.4
Armor 1	85	RHL, 78.8°	5	2270	117	0.36
Armor 2	78	LHL, 82.4°	6	3629	117	0.36

* Two types of Young's modulus, A : for axial rigidity, B : for bending rigidity

6.2.2 Cable design

By using the proposed design procedure and modified cable model with equivalent core in this paper, six α_1 values (72.5°, 75°, 77.5°, 80°, 82.5°, and 85° right-hand lay (RHL)) and five α_2 values (72.5°, 75°, 80°, 85°, and 90° LHL) are selected for the torque balance design.

For the selected α_1 and α_2 values, 30 cases (six α_1 × five α_2) of the torque analyses were performed using the beam FE model. The α_2 torque-relation curves are plotted for all of α_1 values and the zero-torque points were found. Fig. 6.17 shows the α_2 - torque relation curves for all of α_1 values, the curves are plotted and the torque balance points were found. The friction coefficient was used as 0.2 in FE analysis.

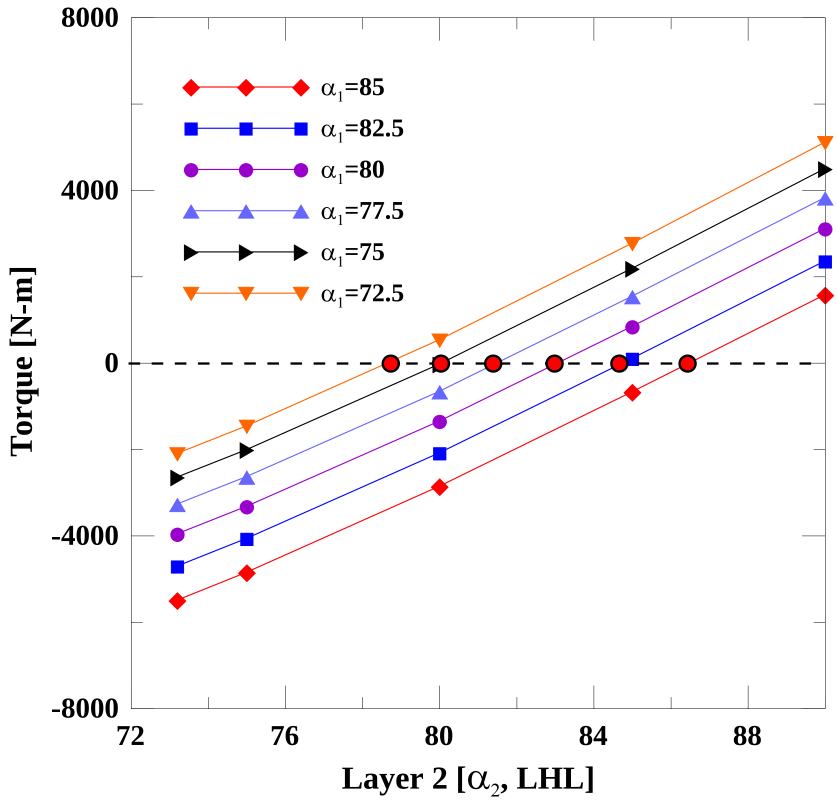

Fig. 6.17. Torque balance points of the submarine power cable

Using the obtained torque balance points, the torque balance curves are plotted, as shown in Fig. 6.18. The equivalent stress curves and flexural rigidity curves are also plotted. The maximum equivalent stress (Von-Mises stress) at the zero torque points is computed as shown in Fig. 6.18. The maximum equivalent stress is calculated in the wire. The flexural rigidity is also computed at the zero torque points and the flexural rigidity curve is plotted, as shown in Fig. 6.18. To compute the flexural rigidity, bending analyses are performed using a beam model for which a bending radius of 2000mm is considered.

On the equivalent-stress curve, Point ① that corresponds to the design stress limit (158MPa), to satisfy the design stress limit, the value of α_1 should be larger than 78.8°, as shown in Fig. 6.18. In the range of α_1, the minimum flexural rigidity is obtained at α_1 = 78.8°, as shown in Point ② of Fig. 6.19. The torque balance point is finally determined at Point ③, whereby α_1 = 78.8° (RHL) and α_2 = 82.4°(LHL), satisfying the design stress limit and minimizing the flexural rigidity.

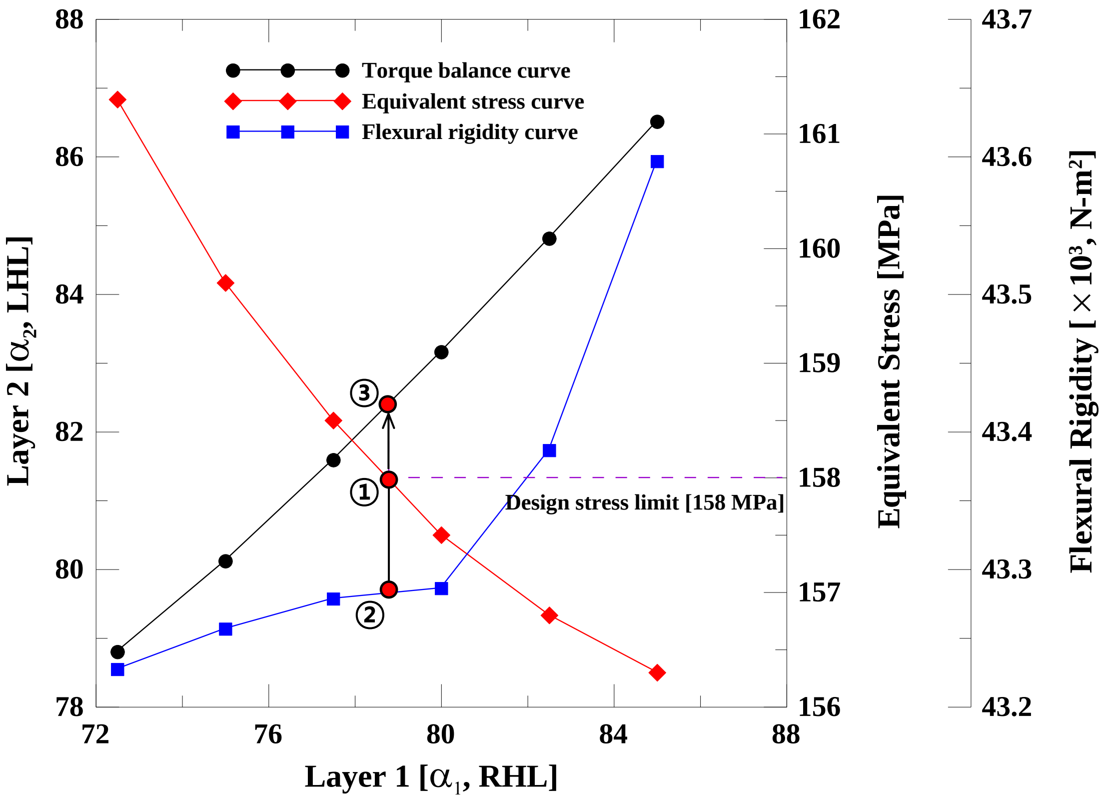

Fig. 6.18. Determination of the torque balance point of the submarine power cable

6.2.3 Experimental test

The tensile tests as shown in Fig. 6.19 were performed on the submarine cable which is manufactured by torque balanced design in section 6.2.2. All the conductor and armors were bonded together at both ends of the cable by means of an anchoring head which prevents them from longitudinal movement and relative rotation inside it. The cable heads were installed in a way that the resulting forces on the different cable components far from the ends are equivalent to the distribution of forces during test. To achieve this is to have separate anchoring devices for the armors and cable core where the relative load sharing can be controlled by a screw device. An anchoring head is shown in Fig. 6.20. Before the test a small tensile load was applied to the cable and the core anchoring position was adjusted, relative to the armor anchoring, to ensure that the core is also loaded. The load was applied up to 1,000kN. During the test, cable axial strain and reaction torque resulting from an applied tension were measured.

(a)

(b)

Fig. 6.19. Tensile test of the submarine power cable (a) Specimen test, (b) Real cable test.

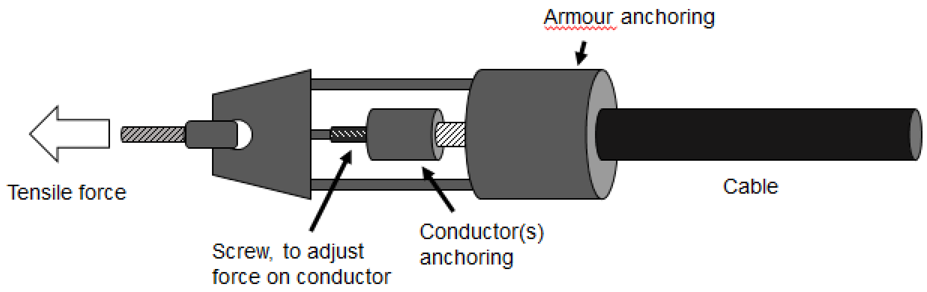

Fig. 6.20 Anchoring head to control relative load sharing between conductor and armor

6.2.4 Results and discussion

Figs. 6.21 and 6.22 compare beam model and experimental results respectively. Fig. 6.21 shows close agreement in the axial load-axial strain plots while Fig. 6.22 shows difference between beam model and experiment.

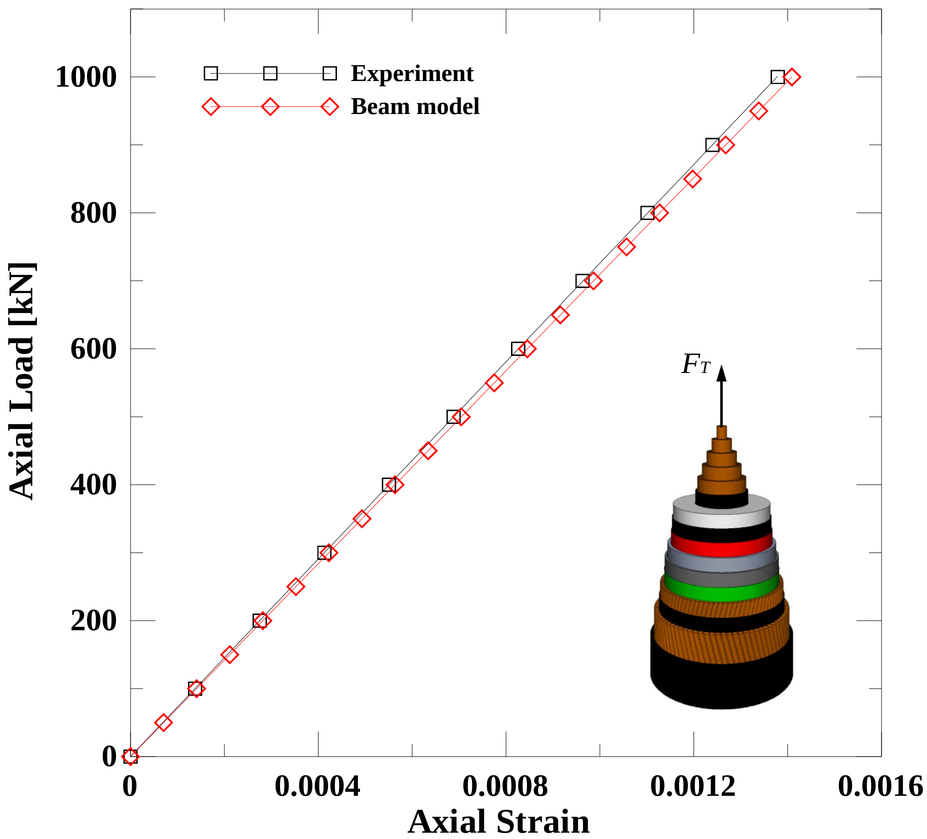

Fig. 6.21. Axial load-axial strain curves of submarine cable

The torque from beam model is nearly “zero”, but the torque from the experiment is 1381N-m when the load applied up to 1,000kN. The conductor of the core originally consists of helically stranded flat wires, the torque of the core is generated under axial load. Thus, the torque from core model should be considered as we mentioned in section 6.2.1. The torque from the core test is 281N-m when the load applied 200kN as shown in Fig. 6.14. If the load in Fig. 6.14 applied up to 1,000kN, the torque from the core is linearly increased up to 1405N-m as shown in Fig. 6.22. This torque value of the core is nearly same with the experiment result of the cable. Considering above result, the proposed beam FE model with torque balance procedure has good agreement with the experiment results.

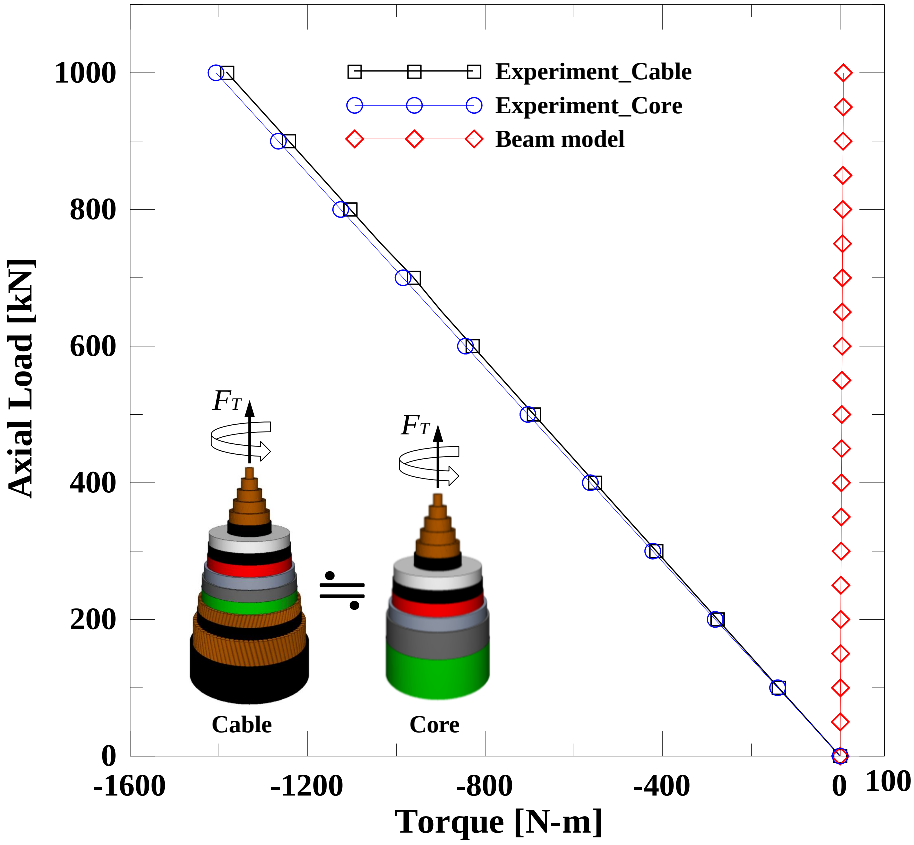

Fig. 6.22. Axial load-torque curves of submarine cable

6.3 Generalized torque balance curves using dimensionless parameter

Two layer contra-helically armored cables have been most widely used in the submarine cable system. Thus, it is very important to achieve torque balance for two layer cable. If the generalized torque balance curves could be introduced for a two layer cable without using any analytical solution or FE analyses, it's very useful and practical to perform preliminary design in cable industry. Therefore, generalized torque balance curves in two layer contra-helically cables were proposed in this section.

Based on eq. (73), generalized torque balance curves can be proposed by properly introducing dimensionless parameter with the geometric and material properties. As discussed in section 5, the three analytical stiffness constants, Eqs. (25b), (26c) and (27c) have to be zero to achieve torque balance. The difference of the values among those three equations is very small because the values are dominated by the wire stretch and they have same stretch term in each equation [see section 2.4]. Therefore, by properly adjusting the geometric and material values in stretch term of those equations, new dimensionless parameter, R_t, for torque balance can be introduced as follows :

$$R_t = \frac{n_1 E_1 A_1 r_1}{n_2 E_2 A_2 r_2}, \tag{77}$$

where n_1, n_2, E_1, E_2, A_1, A_2, r_1 and r_2 are the number of wires, Young's modulus, area of wires and wire center line radius of the each layer, respectively.

The helix angles of each layer for torque balance can be calculated in accordance with the dimensionless parameter, R_t, using the beam FE analysis. The range of the helix angles is selected from 70° to 90°, which are most frequently used in two layer cables.

First, to verify the definition of dimensionless parameter, the model in section 6.2 is used. Several types of model can be made with same R_t (=0.703). For example, if the wire radius of armor 2 is changed from 6mm to 7mm, the number of wires of armor 2 can be changed from 85 to 57 to have same value of R_t as presented in type 1 of table 6.4. Four types of changed models with same R_t are presented in Table 6.4. The values with bold type on the underlines are changed from original model. The material properties of the core are used with the same values.

Table 6.4. Geometric and material properties of the original model and changed model with same dimensionless parameter R_t.

Model	Layer	No. of wires	Wire diameter [mm]	Center line radius [mm]	Young's Modulus [GPa]	Dimensionless parameter R_t
Original	Core	-	138.12	69.06	19.84	0.703
	Armor 1	85	5	71.56	117	
	Armor 2	78	6	77.06	117	
Type 1	Core	-	138.12	69.06	19.84	0.703
	Armor 1	85	5	71.56	117	
	Armor 2	**<u>57</u>**	**<u>7</u>**	**<u>77.56</u>**	117	
Type 2	Core	-	138.12	69.06	19.84	0.703
	Armor 1	**<u>59</u>**	**<u>6.02</u>**	**<u>72.07</u>**	117	
	Armor 2	78	6	**<u>78.08</u>**	117	
Type 3	Core	-	138.12	69.06	19.84	0.703
	Armor 1	85	5	71.56	**<u>100</u>**	
	Armor 2	**<u>66</u>**	**<u>6.03</u>**	**<u>77.08</u>**	117	
Type 4	Core	-	**<u>69.06</u>**	**<u>34.53</u>**	19.84	0.703
	Armor 1	**<u>45</u>**	**<u>5.09</u>**	**<u>37.08</u>**	117	
	Armor 2	**40**	6	**<u>42.62</u>**	117	

The torque balance curves for the original model and changed models were plotted by using proposed design procedure. Fig. 6.23 shows the comparison of torque balance curves among original model and changed models with same R_t (=0.703). The differences among each type can be negligible as shown in Fig. 6.23. Therefore, it's obvious that the definition of dimensionless parameter is appropriate for torque balance, and using this dimensionless parameter, the generalized torque balance curves can be plotted.

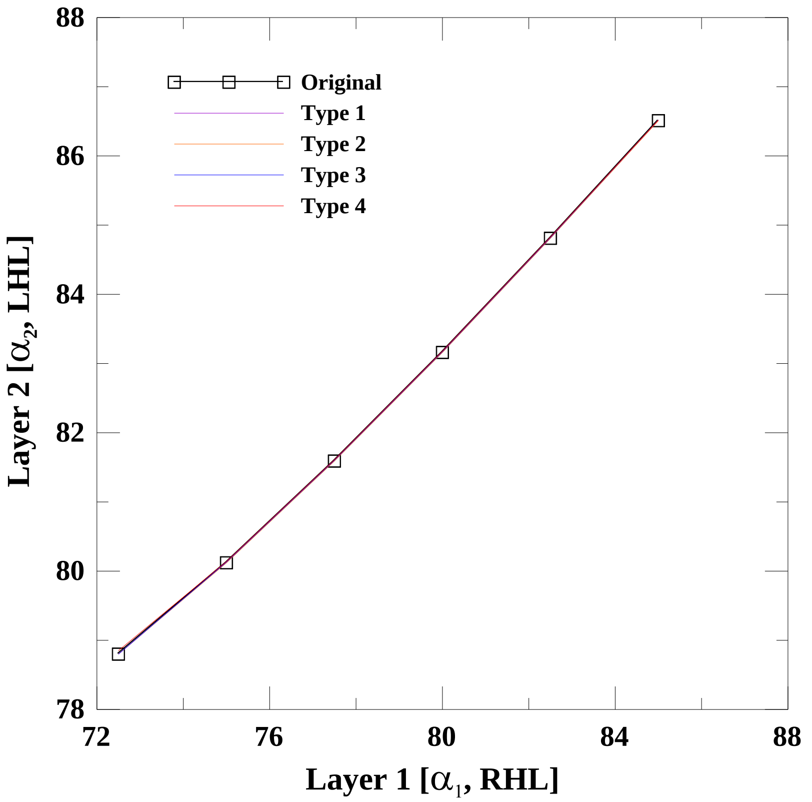

Fig. 6.23. Comparison of torque balance curves among the original model and the changed models with same dimensionless parameter R_t (=0.703).

Fig. 6.24 shows the torque balance curves obtained from the torque analysis of the beam FE model in accordance with a variety of dimensionless parameters for two layer cables. As shown in Fig. 6.24, the torque balance point is determined at Point ① R_t=1.1, α_1 = 70° (RHL) and α_2 = 65.8°(LHL), at Point ② R_t=0.8, α_1 = 75° (RHL) and α_2 = 78.6°(LHL), and at Point ③ R_t=0.5, α_1 = 80° (RHL) and α_2 = 85.2°(LHL), respectively.

This generalized torque balance curves can be a good guidance for preliminary torque balance design instead of relying on experimental data or other analysis tools.

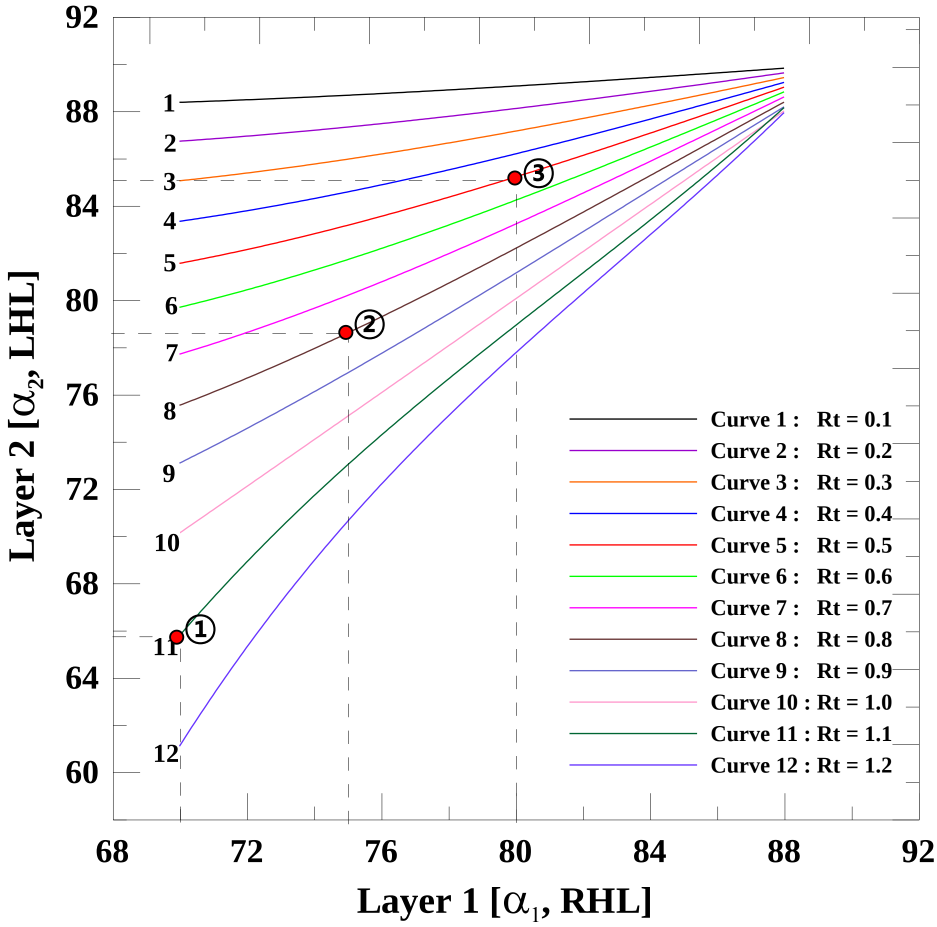

Fig. 6.24. Generalized torque balance curves for a two layer cable with dimensionless parameter, R_t.

7. Conclusion

The stiffness coefficients of the various analytical models for the helically stranded cable were evaluated. The difference in the stiffness coefficients among analytical models was relatively so small. This is mainly because of the predominance of the effect of wire stretch compared to that of wire twist and bending.

To predict the mechanical behavior of helically stranded cables, FE model was proposed in this paper. Regarding the FE modeling, the wire-to-wire contacts and the elastoplastic material behavior are considered. For the contact model, the influence of friction was analyzed and the bilinear coulomb friction model is an effective for the helically-stranded cable in terms of computational efficiency. And, the influence of friction coefficients on the global behavior of the cable was small.

The results that were obtained with the use of three different FE models (solid FE model, beam FE model and mixed FE model) were compared with those of an analytical model and experiments, where the accuracy and computational cost were also investigated. The solutions produced by the FE models were closer to the experimental results than those produced by the analytical model; in particular, the beam FE model accurately predicted global behavior of the cable as the solid FE model did. The computational cost of the beam FE model, however, was significantly less than that of the solid FE model. For this reason, the beam FE model can be a cost-effective solution for the design of helically stranded cables. Since many FE analyses must be performed during the preliminary design stage, the importance of the effectiveness of the beam FE model is heightened.

To verify the validity of the analytical solutions, analytical models and FE model have been compared with stiffness coefficients. As the result, the relative differences of stiffness values between analytical models and beam FE model are less than 5% for the helix angle beyond 75°.

A procedure for the torque balance design whereby the beam FE model is used to design a non-rotating helically stranded cable was proposed. In the proposed torque balance design, the helix angles are first changed using the beam FE model for the performance of a number of torque analyses; simultaneously, the stress and flexural rigidity are calculated, followed by the plotting of the torque balance, equivalent stress, and flexural rigidity curves. Lastly, the helix angles of each of the layers that satisfy the design stress limit and the torque balance are determined, and the flexural rigidity is minimized.

The proposed design procedure is verified by experimental test and the generalized torque balance curve is proposed using new dimensionless parameter. The design procedure and torque balance curves provide an appropriate and rational choice regarding the initial structural parameters for the preliminary design stage of helically stranded cables. It is likely that the impact of the findings of this paper will be significant for cable industries.

Appendix

Appendix A. Stress determination of a stranded cable under axial load

It is assumed that the wires are initially stress free. From the Eqs. (23) and (24), the total axial loads the total axial twisting moment acting on the n outer wires are

$$\frac{F_w}{Er_w^2} = n\left[\frac{F_z}{Er_w^2}\sin\alpha + \frac{F_y}{Er_w^2}\cos\alpha\right], \tag{A.1}$$

$$\frac{M_w}{Er_w^3} = n\left[\frac{M_z}{Er_w^3}\sin\alpha + \frac{M_y}{Er_w^3}\cos\alpha + \frac{F_z}{Er_w^2}\frac{r}{r_w}\cos\alpha - \frac{F_y}{Er_w^2}\frac{r}{r_w}\sin\alpha\right], \tag{A.2}$$

where F_w is total axial load and M_w is the total twisting moment acting on the wires.

The axial load F_c and the axial twisting moment M_c acting on the core (center wire) are given by

$$\frac{F_c}{Er_c^2} = \pi\varepsilon_c, \tag{A.3}$$

$$\frac{M_c}{Er_c^3} = \frac{\pi}{4(1+\nu)} r_c \frac{\Delta\theta}{l}. \tag{A.4}$$

The total axial load F_T and the total axial twisting moment M_T acting on the stranded cable are as

$$F_T = F_c + F_w, \tag{A.5}$$

$$M_T = M_c + M_w. \tag{A.6}$$

In the case of the core, the axial stress is

$$\sigma_{cF} = \frac{F_c}{\pi r_c^2}, \tag{A.7}$$

the maximum shearing stress on the cross

$$\sigma_{cM} = \frac{2M_c}{\pi r_c^3}. \tag{A.8}$$

The outside wires are subjected to axial, bending, and torsional loading in addition to the shearing load F_y. The stresses caused by the shearing force F_y are in general very small and is neglected. The axial stress caused by the load F_w is

$$\sigma_{wF} = \frac{F_w}{\pi r_w^2}, \tag{A.9}$$

the normal stress due to the bending moment M_y is

$$\sigma_{wMy} = \frac{4M_y}{\pi r_w^3}. \tag{A.10}$$

The maximum shearing stress on an outside wire due to the twisting moment M_z is

$$\sigma_{wMz} = \frac{2M_z}{\pi r_w^3}. \tag{A.11}$$

Appendix B. Stress determination of a stranded cable under bending

Based on the equations in section 2.5, the stresses in an outer wire subjected to bending are

$$\sigma_{wMx} = \frac{4M_s}{\pi r_w^3} \cos ks, \tag{B.1}$$

$$\sigma_{wMy} = \frac{4M_s}{\pi r_w^3} \sin\alpha \sin ks, \tag{B.2}$$

$$\sigma_{wMz} = \frac{2M_s}{\pi r_w^3} \cos\alpha \sin ks, \tag{B.3}$$

where

$$k = \frac{\cos\alpha}{r_w}, \tag{B.4}$$

$$M_s = \frac{\pi r_w^4 E \sin\alpha}{2\rho(2+\nu\cos^2\alpha)}, \tag{B.5}$$

σ_{wMx} and σ_{wMy} are the maximum normal bending stresses on a given cross section due to the bending moments M_x and M_y, σ_{wMz} is the maximum shear stress on a given cross section due to the twisting moment M_z. The maximum normal stress on the cross section occurs at $s = 0$, $s = \pi(r_w / \cos\alpha)$, …, and, therefore,

$$\sigma_w = \frac{4M_s}{\pi r_w^3}. \tag{B.6}$$

The core (center wire) is also subjected to bending and, therefore, the maximum bending stress is

$$\sigma_c = \frac{Er_c}{\rho}. \tag{B.7}$$

The maximum bending stress always occurs in the center wire for two reasons, except for considering contact condition. First, the core usually has an equal or larger wire than the outside wire. Second, the helix angle α

tends to decrease the stiffness of an outside wire, compared with a straight wire. For example, a helical spring has a smaller bending stiffness, compared with a straight wire of the same wire diameter.

Appendix C : The minimum value of helical angle of the wire

An equation is derived to determine minimum helical angle of the wire to prevent the outer wires from touching each other.

.

Consider n helical wires, in a strand, that are just touching each other. Let the radius of helix, the wire radius, and the helix angle be denoted by r, r_w and α, respectively. Fig. C. 1(c) shows a wire cross section in a plane perpendicular to the cable. Since the wires are thin, the equation of the cross section, shown in Fig. C. 1(c), will be assumed elliptical and hence,

$$\left(\frac{x}{r_w / \sin\alpha}\right)^2 + \left(\frac{y}{r_w}\right)^2 = 1, \tag{C.1}$$

where (x , y) is any point on the ellipse. Now,

$$\frac{dy}{dx} = \pm\frac{x\sin^2\alpha}{r_w\sqrt{1-\left(\dfrac{x\sin\alpha}{r_w}\right)^2}}. \tag{C.2}$$

Also at the point (x_1, y_1), the slope is equal to $-\tan\left(\dfrac{\pi}{2}-\dfrac{\pi}{n}\right)$, as shown in Fig. C.1(c). Hence,

$$\tan\left(\frac{\pi}{2}-\frac{\pi}{n}\right) = \frac{x_1\sin^2\alpha}{r_w\sqrt{1-\left(x_1\dfrac{\sin\alpha}{r_w}\right)^2}}. \tag{C.3}$$

The solution for x_1 yields

$$x_1 = \frac{r_w}{\sin\alpha}\tan\left(\frac{\pi}{2}-\frac{\pi}{n}\right)\frac{1}{\sqrt{\sin^2\alpha+\tan^2\left(\dfrac{\pi}{2}-\dfrac{\pi}{n}\right)}}, \tag{C.4}$$

whereas Eq. (C.1) results in

$$y_1 = \frac{r_w\sin\alpha}{\sqrt{\sin^2\alpha+\tan^2\left(\dfrac{\pi}{2}-\dfrac{\pi}{n}\right)}}. \tag{C.5}$$

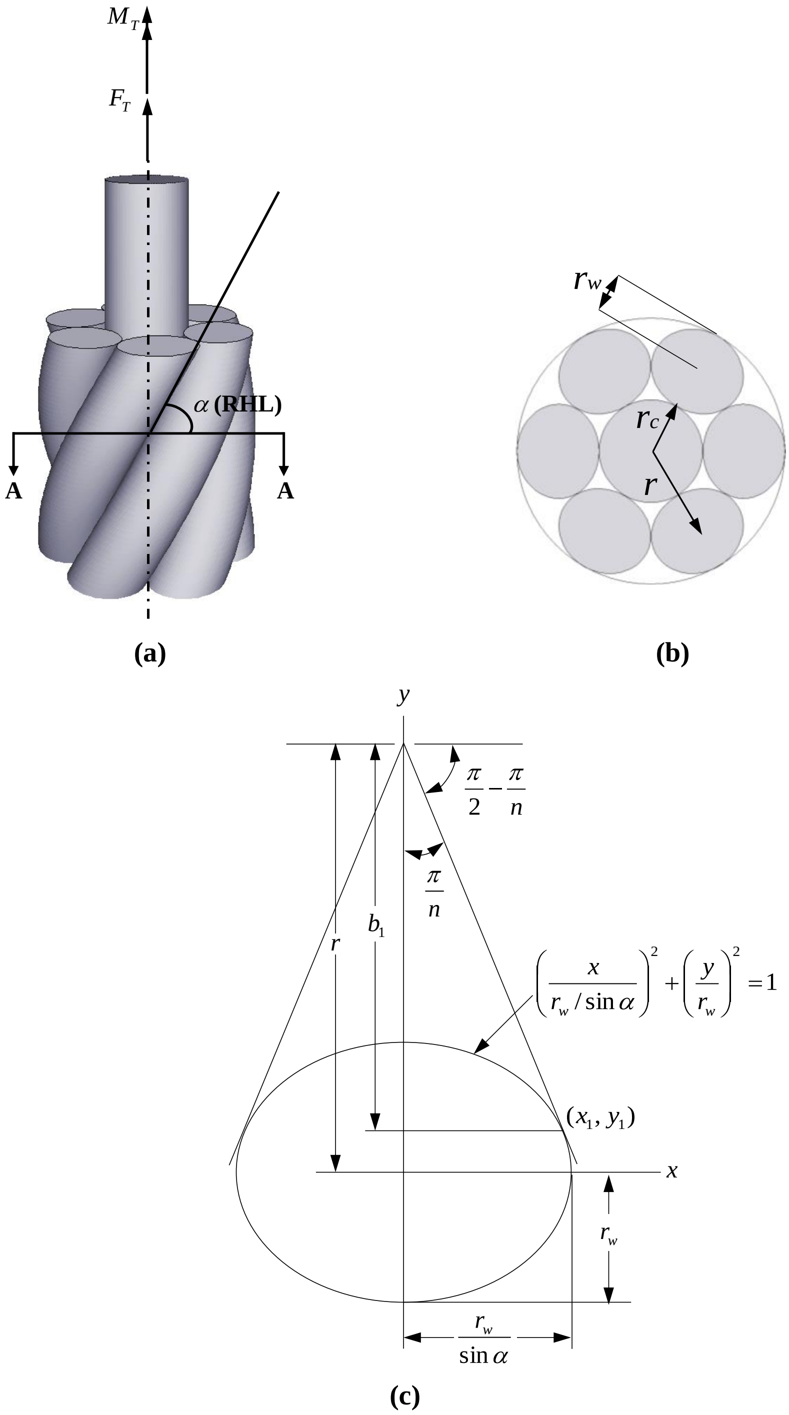

Fig. C.1. Geometry of a helically-stranded cable (1 layer, 1 + 6 structure). (a) Cable geometry, (b) Cross section A-A, (c) Wire cross section perpendicular to axis of cable

Fig. C. 1(c) indicates that

$$b_1 = x_1 \tan\left(\frac{\pi}{2} - \frac{\pi}{n}\right), \qquad \text{(C.6)}$$

and, hence, since $r = b_1 + y_1$,

$$r = r_w \sqrt{1 + \frac{\tan^2\left(\frac{\pi}{2} - \frac{\pi}{n}\right)}{\sin^2 \alpha}} \, . \qquad \text{(C.7)}$$

Finally, the equation of minimum value of helical angle is as below

$$\sin \alpha = \sqrt{\frac{r_w^2 \tan^2\left(\frac{\pi}{2} - \frac{\pi}{n}\right)}{r^2 - r_w^2}} \qquad \text{(C.8)}$$

Bibliography

[1] Utting WS, Jones N. The response of wire rope strands to axial tensile loads - part I: experimental results and theoretical predictions. International Journal of Mechanical Science 1987; 29(9):605–619.

[2] Utting WS, Jones N. The response of wire rope strands to axial tensile loads - part II: comparison of experimental and theoretical predictions. International Journal of Mechanical Science 1987; 29(9): 621–636.

[3] Utting WS, Jones N. Axial-torsional interactions and wire deformation in 19-wire spiral strand. Journal of Strain Analysis for engineering design 1988; 23(2): 79-86.

[4] Costello GA. Analytical investigation of wire rope. Applied Mechanics Reviews 1978; 31(7).

[5] Costello GA. Theory of wire rope. 2nd ed. New York: Springer; 1997.

[6] Machida S, Durelli AJ. Response of a strand to axial and torsional displacements. Journal of Mechanical Engineering science1973;15:241–251.

[7] Knapp RH. Derivation of a new stiffness matrix for helically armoured cables considering tension and torsion. International Journal for Numerical Methods in Engineering 1979; 14: 515–520.

[8] Lanteigne J. Theoretical estimation of the response of helically armored cables to tension, torsion, and bending. Journal of Applied Mechanics 1985; 52(2): 423–432.

[9] Ramsey H. Analysis of inter wire friction in multilayered cables under uniform extension and twisting. International Journal of Mechanical Sciences 1990; 32(8): 709–716.

[10] Sathikh S, Moorthy MBK, Krishnan M. A symmetric linear elastic model for helical wire strands under axisymmetric loads. Journal of Strain Analysis for engineering design 1996; 31(5): 389–399.

[11] Nawrocki A, Labrosse M. A finite element model for simple straight wire rope strands. Computers and Structures 2000; 77(4): 345–359.

[12] Jiang WG, Yao MS, Walton JM. A concise finite element model for simple straight wire rope strand. International Journal of Mechanical Science 1999; 41(2): 143–61.

[13] Ghoreishi SR, Messager T, Cartraud P, Davies P. Validity and limitations of linear analytical models for steel wire strands under axial loading, using a 3D FE model. International Journal of Mechanical Science 2007; 49(11): 1251–1261.

[14] Judge R, Yang Z, Jones SW, Beattie G. Full 3D finite element modelling of spiral strand cables. Construction and Building Materials 2012; 35: 452–459.

[15] Stanova E, Fedorko G, Fabian M, Kmet S. Computer modelling of wire strands and ropes part II: finite element-based applications. Advances in Engineering Software 2011; 42(6): 322–331.

[16] Kmet S, Stanova E, Fedorko G, Fabian M, Brodniansky J. Experimental investigation and finite element analysis of a four-layered spiral strand bent over a curved support. Engineering Structures 2013; 57: 475-483

[17] Yujie Yu, Zhihua Chen, Hongbo Liu, Xiaodun Wang. Finite element study of behavior and interface force conditions of seven-wire strand under axial and lateral loading. Construction and Building Materials 2014; 66: 10–18.

[18] CATIA Version 5. Release 18, English Documentation. Dassault System, 2007.

[19] MSC, Marc® Software Manual Volume A: Theory and User Information (Version2011), MSC Software Corporation, 2012.

[20] Timoshenko, SP, Goodier JN. Theory of elasticity. McGraw Hill, New York.1970.

[21] Bathe, KJ. Finite element procedures. Prentice Hall, New York. 1996.

[22] Yoon K, Lee Y, Lee PS. A continuum mechanics based 3-D beam finite element with warping displacements and its modeling capabilities. Structural Engineering and Mechanics2012; 43(4): 411-437.

[23] Yoon K, Lee PS. Nonlinear performance of continuum mechanics based beam elements focusing on large twisting behaviors. Computer Methods in Applied Mechanics and Engineering 2014; 281: 106-130.

[24] O. Kawa, P. Litewka. Contact between 3-D beams with deformable circular cross sections. CRC Press/Balkema. 2013.

[25] Chen C, Zheng G, Yan H, Du Y. Further determination of friction coefficients between high-strength zinc-coated steel wires in stay cables. J Chongqing Jiaotong Univ (Natural Sci) 2012; 31(2).

[26] Knapp RH, Das S, Shimabukuro TA. Computer-aided design of cables for optimal performance - geometric modelling and finite element software for structural design of cables. Sea Technology 2002; 43(7): 41–46.

[27] Knapp RH. Torque and stress balanced design of helically armored cables. Journal of engineering for industry 1981; 103: 61–66.

[28] Cable CAD® v2.4 User Manual, Knapp Engineering, Inc. 2010.

[29] Christian, B. P., Nerenstein, W. Analysis and Test of Torque Balanced Electro-Mechanical Mooring Cables. MTS Proceedings, 1976

[30] Liu, F.C., Design of Torque-Free Cables Using a Simulation Model. MTS Proceedings, 1976.

[31] Nakai M, Sato S, Aida T, Tomioka H. On the creep and the relaxation of spiral ropes. Bull JSME 1975; 18(125): 1308–1314.

[32] Utting WS, Jones N. Tensile testing of a wire rope strand. Journal of Strain Analysis for engineering design 1985; 20(3) : 151–164.

[33] Utting WS. Experimental and theoretical studies on stresses in and deformation of wire ropes under axial tensile loads. PhD thesis. University of Liverpool; 1984.

[34] Raoof M, Kraincanic I. Analysis of large-diameter steel ropes. Journal of Engineering Mechanics - ASCE 1995; 121(6): 667–675.

[35] BS EN 1993-1-11:2006. Eurocode 3 – design of steel structures: part 1-11: design of structures with tension components.

[36] Bridon structural systems catalogue 11/2007, 3 ed.

[37] Jolicoeur C, Cardou A. Semicontinuous mathematical model for bending of multilayered wire strands. Journal of Engineering Mechanics 1996; 122(7): 643–650.

[38] Feyrer K. Wire ropes, tension, endurance, reliability. Berlin: Springer-Verlag; 2007.

[39] Cardou A, Jolicoeur C. Mechanical models of helical strands. Applied Mechanics Review 1997; 50(1): 1–14.

[40] Kumar K, Botsis J. Contact stresses in multilayered strands under tension and torsion. Journal of Applied Mechanics 2001; 68(3): 432–440.

[41] Knapp RH, Chiu E. Tension fatigue model for helically armored cables. Journal of energy resources technology 1988; 110: 12-18

[42] McConnell KG, Zemeke WP. A model to predict the coupled axial torsion properties of ACSR electrical conductors. Journal of Experimental Mechanics 1982; 22: 237–244.

[43] Hruska FH. Calculation of stresses in wire ropes. Wire and wire products 1951; 26(9): 766–767.

[44] Hruska FH. Radial forces in wire ropes. Wire and wire products 1952; 27(5): 459–463.

[45] Hruska FH. Tangential forces in wire ropes. Wire and wire products 1953; 28(5): 455–460.

[46] Kumar K, Cochran Jr JE. Closed-form analysis for elastic deformations of multilayered strand. Journal of Applied Mechanics 1987; 54: 898–903.

[47] Labrosse M. Contribution to the study of the role of friction on the behavior and life of single layer cable. PhD thesis, Ecole Centrale de Nantes, France, 1998.

[48] Le TT, Knapp RH. A finite element model for cables with nonsymmetrical geometry and loads. Journal of offshore mechanics and arctic engineering 1994; 116: 14-20

[49] Knapp RH, Xin Liu. Cable vibration considering interlayer coulomb friction. International journal of offshore and polar engineering 2005; 15(3): 229-234

[50] Gnanavel BK, Gopinath D, Parthasarathy NS. Effect of friction on coupled contact in a twisted wire cable. Journal of applied mechanics 2010; 77: 024501-1-6

[51] Roark, RJ. Formulas for stress and strain. McGraw Hill, New York. 1965.

[52] P. Litewka. Finite Element Analysis of Beam to Beam Contact. Berlin Heidelberg, Springer. 2010.

[53] V. L. Popov. Contact Mechanics and Friction. Verlag Berlin Heidelberg, Springer. 2010.

[54] Papailiou KO. On the bending stiffness of transmission line conductors. IEEE Trans Power Deliv 1997; 12(4): 1576-1588.

[55] Enzhen X, Chunyan Z. Analysis of the bending behavior of a cable structure under microgravity. International Journal of Mechanical Sciences 2016; 114: 132–140.

[56] Hong KJ, Armen DK, Jerome LS. Bending Behavior of Helically Wrapped Cables. Journal of Engineering Mechanics 2005; 131(5): 500–511.

[57] Nikolaos K, Panagiotis A. Optimal structural arrangements of multilayer helical assemblies. International Journal of Solids and Structures 2016; 78: 1–8.

[58] Nikolaos K, Gerald K. Mechanical response of a helical body to axial, torsional and radial strain. International Journal of Mechanical Sciences 2015; 94-95: 260–265.

Summary in Korean

다중 보 유한요소를 이용한 케이블의 모델링 방법 및 이를 이용한 케이블 설계

스트랜드 케이블(Helically stranded cable) 기계적 거동 해석을 위한 이론 모델에 대해 각 강성계수(stiffness coefficient)를 계산하고 이에 따른 영향도를 분석하였다. 외부 축 하중이 작용하는 스트랜드 케이블 이론 모델의 강성계수는 각 와이어의 인장, 굽힘 및 비틀림에 의해 결정되지만, 분석 결과 와이어의 인장 요인이 지배적으로 작용하여, 각 이론 모델들은 유사한 강성 계수 값을 가지는 것을 알 수 있었다.

케이블의 기계적 거동 해석을 위한 유한요소 수치해석 모델을 제안하였다. 유한요소 해석 모델은 각 와이어간의 접촉 거동 및 탄소성 재료 거동을 잘 구현할 수 있도록 구성하였다. 특히, 접촉 거동을 구현하기 위해 쿨롱 마찰(Coulomb friction)을 사용하고, 이를 이용한 세가지 마찰 모델에 대해 서브루틴(Subroutine) 프로그램을 이용하여 유한요소해석 모델의 마찰 거동을 구현한 후 이에 대해 비교 분석하였다. 분석 결과, 각 마찰 모델간의 케이블의 거시 거동(global behavior)은 유사하였으며, 세가지 모델 중 변형된 계단 함수 모델(Bilinear model)이 가장 효율적인 해석 결과를 나타내었다. 또한, 마찰 계수(friction coefficient)에 따른 영향을 분석한 결과, 마찰 계수에 따른 케이블의 거시 거동(global behavior)에 대한 결과는 유사하였으며, 응력은 마찰 계수 증가에 따라 축방향 변형률(strain)의 감소로 인해 감소하는 결과를 보여주었으나, 그 수준의 차이는 크지 않았다. 이러한 마찰의 영향은 지속적 반복 하중 등과 같은 케이블의 장기 수명 특성에 영향을 줄 것으로 판단되므로, 해석 결과에 대한 정확한 적용이 필요하다.

유한요소 해석 모델로 3 차원 고체 유한요소(3D solid FE model), 보 유한요소(beam FE model) 및 혼합 유한요소(Mixed model, 고체+보 유한요소)의 세가지 모델을 제안하였다. 세가지 유한요소 모델에 대해 케이블의 축하중 및 굽힘 하중시의 거동을 해석하고 이론 및 실험 결과와 제안된 유한요소 모델들간의 정확성과 효율성을 비교하였다. 각 유한요소 해석 모델들은 이론 모델에 비해 모두 실험 결과와 더 잘 일치하는 결과를 나타내었다. 이 중 고체 유한요소는 케이블 각 와이어의 상세 접촉 응력(detail contact stress), 부분 항복 응력(local yielding stress) 등 미시 거동(local behavior)을 매우 잘 구현하지만, 타 모델에 비해 상대적으로 해석 효율성이 떨어진다. 보 유한요소는 케이블의 미시 거동의 정확한 표현에는 일부 제한적이지만, 케이블 전체 거동을 정확히 해석하면서도 효율성이 뛰어나므로, 케이블 설계 단계에서의 모델로서 가장 적합함을 알 수 있었다.

본 논문에서 제안된 다중 보 유한요소해석 모델을 이용하여 이론 모델에 대한 적용성(validity)을 평가하였다. 평가 결과, Hruska 모델을 제외한 Costello 모델과 Machida 모델은 케이블 꼬임각도(Helix angle)가 75° 이상의 경우 유한 요소 모델과 5% 이내의 일치하는 해석 결과를 나타냄을 알 수 있었다.

다중 보 유한요소해석을 이용한 스트랜드 케이블의 회전 균형 설계 방법(procedure of torque balance design)을 제안하였다. 먼저, 케이블 각 층별(layer) 꼬임각도(helical angle)에 따른 회전력(torque)을 계산하고, 회전력이 0 이 되는 회전 균형 곡선(torque balance curve)을 제시하였다. 동시에 설계 기준 응력(design stress limit)과 유연성(flexural rigidity)을 모두 만족하는 최적 회전 균형점을 찾고 이를 케이블의 최적 설계점(optimized torque balance point)으로 제안하였다.

상기 회전 균형 설계 방법에 대해 실제 다양한 케이블에 대해 적용하고 실험을 통해 그 결과를 검증한 결과, 설계 결과와 잘 일치함을 확인하였다. 또한, 회전 균형 무차원 계수의 도입을 통해 초기 케이블 설계 단계에서 해석 도구나 이론적 모델의 적용 없이 그래프를 이용하여 산업 현장에서 쉽게 적용 가능한 회전 균형 곡선을 제시하였다.

핵심낱말 : 스트랜드 케이블, 유한요소해석, 보요소, 보모델링, 쿨롱 마찰, 마찰 계수, 회전 균형 설계

Acknowledgments in Korean

뒤늦게 시작한 학위 과정을 과연 제대로 끝을 맺을 수 있을까, 어려운 과정들 속에 낙오되지 않을까, 과연 지금과 미래의 나에게 타당한 일인가, 많이 고민스럽고 어려웠지만, 작은 부분이지만 깊은 학문을 하고 있다는 자부심과 반드시 학위에 대한 꿈을 이루려는 의지로 앞만 보고 달려온 지난 시간들을 생각하면, 지금 저의 감정은 복잡하고 어려운 시험을 하나 치르고 나오는 수험생의 마음과 같이 만감이 교차합니다.

어려운 과정 속에서 무사히 학위를 마칠 수 있도록 학문적 지도와 여러 가지 배려를 해주신 이필승 교수님께 감사를 드립니다. 정말 교수님의 지도와 배려가 없었다면, 오늘의 이 자리가 오지 않았을 것이라는 생각에 더 큰 고마움을 느낍니다. 그리고, 바쁘신 와중에도 기꺼이 심사위원을 맡아주시고 더 나은 학위 논문이 될 수 있도록 많은 조언을 해주신 김진환 교수님, 정 현 교수님, 김병완 박사님, 그리고 이준근 박사님께 깊은 감사의 말씀을 드리고 싶습니다.

지난 몇 년간 제가 학위 과정을 진행하는 동안 늘 많은 도움을 주었던 CMSS 연구실 졸업생 및 재학생 모두에게도 진심으로 감사하다는 말을 전하고 싶습니다. 졸업생들은 사회에서 더 훌륭한 인재가 되어 승승장구하기를 바라고, 재학생들은 더욱 학문에 증진하여 좋은 연구 성과와 원하는 바를 모두 성취하기를 진심으로 바랍니다.

직장 생활과 학업을 병행하면서, 업무에 대한 배려와 학위 과정에 대한 깊은 이해로 제가 무사히 학위를 마칠 수 있도록 도와주신 회사 동료들과 여러 선후배 분들께도 진심으로 감사 드립니다. 지금 이 자리에서 저의 작은 성취가 앞으로 회사의 큰 발전이 될 수 있도록 더욱 노력하겠습니다.

늘 아낌없는 사랑과 믿음을 주신 부모님과 형제들, 그리고, 장인, 장모님을 비롯한 처갓집 식구들 모두에게도 그 동안 지원해주시고 격려해 주신데 대해 진심으로 감사를 드리고 싶습니다. 끝으로, 오늘 이 자리가 있기까지, 늘 옆에서 격려해주고 희생해주며 묵묵히 자리를 지켜준 사랑하는 아내 정희에게 정말 고맙고 사랑한다고 전하고 싶고, 우리의 소중한 아들 동현이에게도 사랑한다는 말과 함께 저의 이 작은 결실이 조금이나마 보답이 되기를 바랍니다.

2017 년 5 월

김 성 윤 올림